

A 5902 II

Dz.6

POLISH ACADEMY OF SCIENCES – WROCLAW BRANCH
WROCLAW UNIVERSITY OF TECHNOLOGY

Biblioteka Główna i OINT
Politechniki Wrocławskiej



100100354465

ISSN 1644-9665
INDEX 375667



ARCHIVES OF CIVIL AND MECHANICAL ENGINEERING

Quarterly
Vol. III, No. 1

WROCLAW 2003

ADVISORY COMMITTEE

Chairman – JAN KMITA¹

JAN BILISZCZUK (Poland)

CZESŁAW CEMPEL (Poland)

ROMAN CIESIELSKI (Poland)

JERZY GRONOSTAJSKI (Poland)

ANTONI GRONOWICZ (Poland)

M.S.J. HASHMI (Ireland)

HENRYK HAWRYLAK (Poland)

RYSZARD IZBICKI (Poland)

WACŁAW KASPRZAK (Poland)

MICHAEL KETTING (Germany)

MICHAŁ KLEIBER (Poland)

VADIM L. KOŁMOGOROV (Russia)

ADOLF MACIEJNY (Poland)

ZDZISŁAW MARCINIAK (Poland)

KAZIMIERZ RYKALUK (Poland)

ANDRZEJ RYŻYŃSKI (Poland)

ZDZISŁAW SAMSONOWICZ (Poland)

WOJCIECH SZCZEPIŃSKI (Poland)

PAWEŁ ŚNIADY (Poland)

TARRAS WANHEIM (Denmark)

WŁADYSŁAW WŁOSIŃSKI (Poland)

JERZY ZIÓŁKO (Poland)

JÓZEF ZASADZIŃSKI (Poland)

EDITORIAL BOARD

Editor-in-chief – JERZY GRONOSTAJSKI²

ROBERT ARRIEUX (France)

AUGUSTO BARATA DA ROCHA (Portugal)

GHEORGHE BRABIE (Romania)

L. DEMKOWICZ (USA)

KAZIMIERZ FLAGA (Poland)

YOSHINOBI FUJITANI (Japan)

FRANCISZEK GROSMAN (Poland)

MIECZYSLAW KAMIŃSKI (Poland)

Scientific secretary – SYLWESTER KOBIELAK
(Poland)

ANDRZEJ KOCAŃDA (Poland)

WACŁAW KOLLEK (Poland)

PIOTR KONDERLA (Poland)

ZBIGNIEW KOWAL (Poland)

TED KRAUTHAMMER (USA)

ERNEST KUBICA (Poland)

KRZYSZTOF KURZYDŁOWSKI (Poland)

TADEUSZ MIKULCZYŃSKI (Poland)

HARTMUT PASTERNAK (Germany)

MACIEJ PIETRZYK (Poland)

EUGENIUSZ RUSIŃSKI (Poland)

HANNA SUCHNICKA (Poland)

¹ The Faculty of Civil Engineering, Wrocław University of Technology
Wybrzeże Wyspiańskiego 27, 50-370 Wrocław, Poland

Tel. +48 71 320 22 46, Fax. +48 71 320 35 45, Email: mosty@pwr.wroc.pl

² The Faculty of Mechanical Engineering, Wrocław University of Technology
ul. Łukasiewicza 3/5, 50-371 Wrocław, Poland

Tel. +48 71 320 21 73, Fax. +48 71 320 34 22, Email: gronosta@itma.pwr.wroc.pl

POLISH ACADEMY OF SCIENCES – WROCLAW BRANCH
WROCLAW UNIVERSITY OF TECHNOLOGY



ARCHIVES OF CIVIL AND MECHANICAL ENGINEERING

Quarterly
Vol. III, No. 1

WROCLAW 2003

EDITOR IN CHIEF

JERZY GRONOSTAJSKI

EDITORIAL LAYOUT AND PROOF-READING

EWA SOBESTO, SEBASTIAN ŁAWRUSEWICZ

SECRETARY

TERESA RYGLOWSKA

Publisher: Committee of Civil and Mechanical Engineering
of Polish Academy of Sciences – Wrocław Branch,
Faculty of Civil Engineering and Faculty of Mechanical Engineering
of Wrocław University of Technology

© Copyright by Oficyna Wydawnicza Politechniki Wrocławskiej, Wrocław 2003

OFICyna WYDAWNICZA POLITECHNIKI WROCLAWSKIEJ
Wybrzeże Wyspiańskiego 27, 50-370 Wrocław

Drukarnia Oficyny Wydawniczej Politechniki Wrocławskiej. Zam. nr 499/2003.

Contents

B. CHIRITA, Experimental study of the influence of blankholder force on spring-back of sheet metal	5
P. ŚNIADY, R. SIENIAWSKA, S. ŻUKOWSKI, Reliability of bridge beams with hybrid cross-sections	13
I. SCHINDLER, E. HADASIK, Influence of structure on strain-rate sensitivity index at hot forming of steel	25
K. WIDANKA, The improvement in fatigue characteristic of sintered steel by vacuum carburizing	33
J. FALCÃO CARNEIRO, A. PESSOA DE MAGALHÃES, F. GOMES DE ALMEIDA, A. BARATA DE ROCHA, A contribution to optimal loading/unloading performance in automatic press feeding: the MANPRESS robot	39
W. GLABISZ, State analysis of time-varying linear systems via Walsh-wavelet packets	59
CZ.MACHELSKI, Probability of cracking of composite prestressed concrete bridges	77

Spis treści

B. CHIRITA, Badania wpływu siły dociskacza na powrotne odkształcenia sprężyste blach	5
P. ŚNIADY, R. SIENIAWSKA, S. ŻUKOWSKI, Niezawodność belek mostowych o przekroju hybrydowym	13
I. SCHINDLER, E. HADASIK, Wpływ struktury na wskaźnik czułości naprężenia na prędkość odkształcenia podczas przeróbki plastycznej na gorąco	25
K. WIDANKA, Poprawa charakterystyki zmęczeniowej stali spiekanej przez nawęglanie próżniowe	33
J. FALCÃO CARNEIRO, A. PESSOA DE MAGALHÃES, F. GOMES DE ALMEIDA, A. BARATA DE ROCHA, Wkład do optymalnego automatycznego podawania i odbierania wyrobów z pras: robot MANPRESS	39
W. GLABISZ, Falkowe pakiety Walsha w analizie układów liniowych o zmiennych w czasie współczynnikach	59
CZ.MACHELSKI, Prawdopodobieństwo zarysowania zespolonych mostów z betonu sprężonego	77

Experimental study of the influence of blankholder force on spring-back of sheet metal

BOGDAN CHIRITA

University of Bacau, Romania

Spring-back is the main defect of the U-shaped parts. After removal of tools, the U-shaped part undergoes significant modification of the angles between the bottom, the sidewall and the flange, and also a curvature of the sidewall appears. The blankholder force is an important factor in controlling the size of spring-back parameters. The present paper is an experimental study of how blankholder force influences spring-back phenomenon.

Keywords: *sheet metal forming, U-bending, spring-back, blankholder force*

1. Introduction

In sheet metal forming processes, at the end of the operation the blank being formed conforms closely to the shape of tools. After the load is released and the tools are removed the U-shaped part undergoes significant changes of its geometrical and shape parameters. This phenomenon is called a *spring-back*.

Spring-back parameters are mainly influenced by the following factors: punch and die radii, initial clearance, friction conditions, blankholder force and blankholder geometry, geometry of draw beads, sheet thickness, elastic modulus, Poisson's coefficient, blank material, and constitutive behaviour of the material in plastic field [1], [3], [4].

According to professional literature during the forming process of the U-shaped part, the sidewall suffers complicated bending and stretching phenomena. The stress distribution through the thickness of the sidewall is the following: the side near the die is subjected to tensile stress and the side near the punch – to compressing stress, which would promote a residual bending moment a result in sidewall curl. Introducing a considerable blankholder force into the forming process is useful in removing sidewall curl. When the blankholder force is increased, namely increasing the flow resistance of the material, the stress distribution through the thickness of the sidewall may be turned to tensile stress over the whole section. Accordingly, spring-back directions of both sides become consistent, which is conducive to decreasing shape distortion [2].

However, the increase of the blankholder force over a certain limit leads to a greater possibility of crack and fracture appearance.

A method used to diminish the spring-back intensity is described by Liu et al. [2] and consists in applying a variable blankholder force starting with a low optimum value followed by a sudden increase of its value which is beneficial to retain the part shape.

2. Experimental set-up

The present paper is an experimental research in the influence of the blankholder force upon spring-back parameters. Two methods were investigated: one that uses a constant blankholder force and the other that uses variable blankholder forces. The experiments were conducted using the set-up shown in Figure 1.

The material tested is an aluminium alloy.

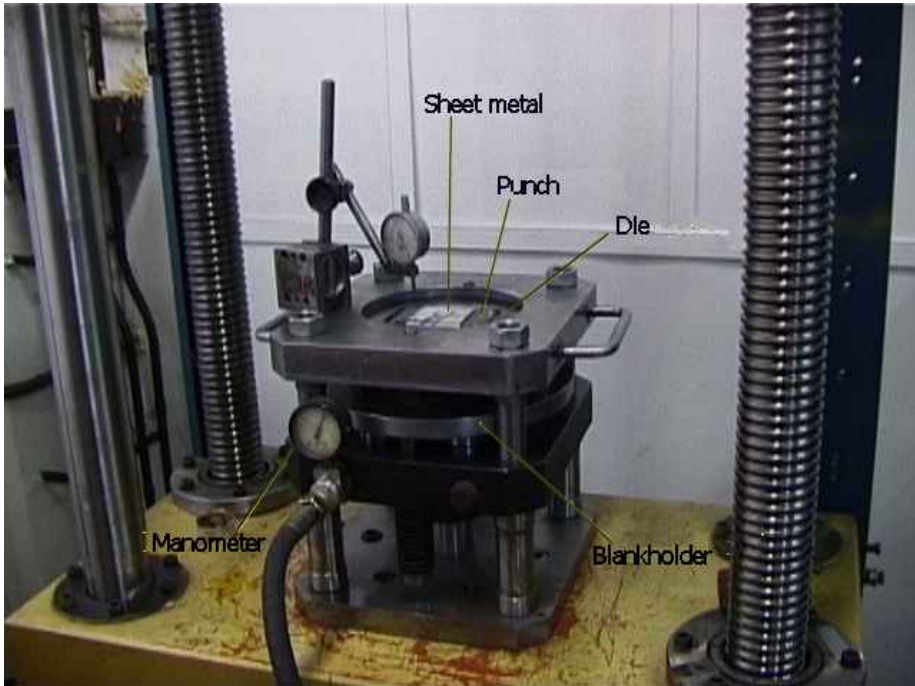


Fig. 1. Experimental set-up

The strips used are 220×30 mm and 1 mm thick. The strips were cut out of the sheets in the rolling direction and then milled in order to obtain a constant edge thickness.

Geometric parameters of tools are presented in Table 1.

Table 1. Geometric parameters of tools

Punch size (mm)	78.5×120
Punch radius (mm)	8
Die opening (mm)	80
Die radius (mm)	12
Punch travel (mm)	50
Blankholder force (kN)	5...45

Blankholder force variation was obtained using a hydraulic device manually driven and a manometer indicating the pressure.

3. Results of investigations concerning the influence of constant blankholder force on spring-back intensity

The spring-back parameters (Figure 2) whose variation was observed during experimental research are as follows:

- θ_1 – the angle between the bottom of the part and the sidewall;
- θ_2 – the angle between the flange and the sidewall;
- ρ – the curvature radius of the sidewall.

The final shapes of aluminium alloy parts after spring-back are illustrated in Figure 3 for different values of blankholder force. The left half-profiles of the parts are presented in Figure 4.

The blankholder force was limited to 45 kN because higher values led to broken parts.

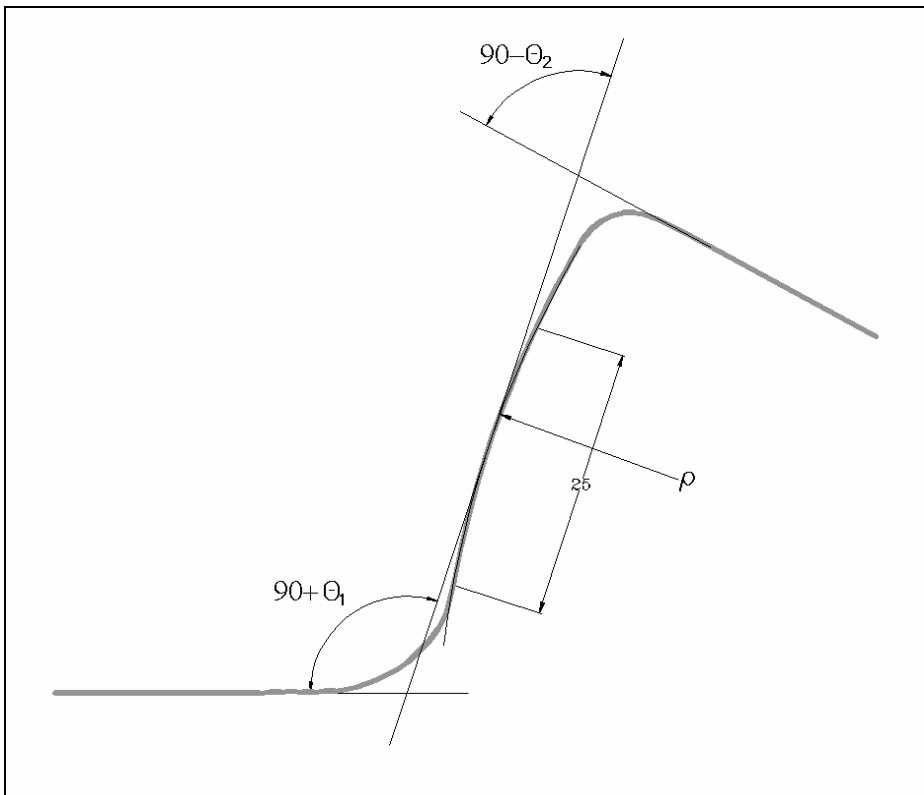


Fig. 2. Spring-back parameters



Fig. 3. The shape of aluminium alloy parts after spring-back

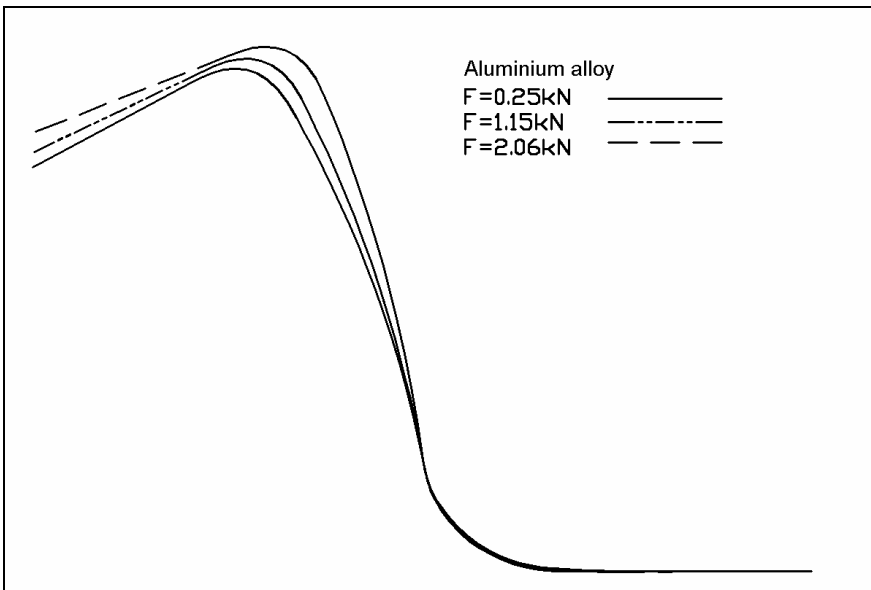


Fig. 4. Influence of blankholder force on spring-back

The measured values of spring-back parameters are presented in Table 2.

Table 2. Spring-back parameters for aluminium alloy parts

Blankholder force (kN)	θ_1	θ_2	ρ
5	15.57	10.16	113.89
10	12.33	9.27	119.2
15	11	8.48	123.5
20	10.26	7.71	126.6
25	9.9	7.17	129.7
30	9.6	7.06	132.8
35	9.32	6.93	141.5
40	9.1	6.93	172.3
45	8.97	6.82	237.48

Due to superimposing the graphs of parameters variation we obtain a nomogram presented in Figure 5. From its analysis the following conclusions can be drawn:

- The spring-back angles θ_1 and θ_2 vary more substantially for smaller values of blankholder force. An increase of blankholder force from 5 kN to 45 kN leads to a decrease of spring-back angles of approximately 42% for θ_1 and 32% for θ_2 .
- The sidewall-curvature radius varies more substantially for higher values of blankholder force. An increase of blankholder force from 5 kN to 45 kN leads to an increase of approximately 52% of sidewall curvature radius.

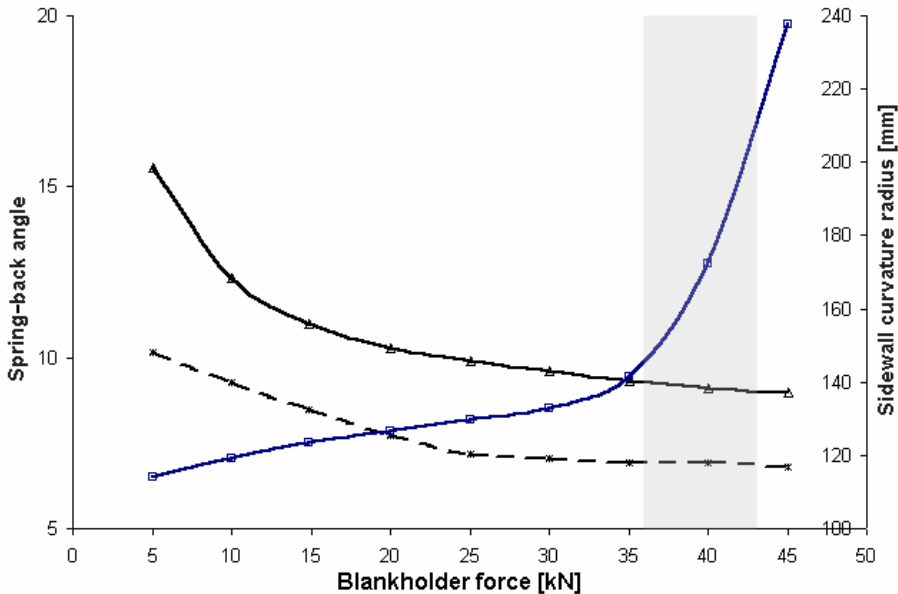


Fig. 5. Optimum blankholder force domain

Based on the results obtained and the facts presented above an optimum domain was chosen for the value of blankholder force. This domain can be considered as comprised between 36 and 43 kN and it is highlighted by grey colour in Figure 5. For this domain the parts result close to the desired shape without the risk of tearing.

4. Results of the investigations concerning the effect of variable blankholder force on spring-back intensity

Based on the method described by Liu et al. [2] the following steps and domains of variable blankholder forces were investigated:

- the application of a blankholder force in two steps: a low value equal to 0.25 kN until a drawing depth of 6 mm is reached followed by a higher value equal to 40 kN until the end of forming process;
- the application of blankholder force in three steps: the first value equal to 0.25 kN until the drawing depth of 6 mm is reached, the second value equal to 20 kN until the drawing depth of 30 mm is reached and the third blankholder force value of 40 kN until the end of forming process;
- the application of blankholder force in three steps: the first value equal to 0.25 kN until the drawing depth of 6 mm is reached, the second value equal to 40 kN until the drawing depth of 44 mm is reached and the third value of 0.25 kN for the final step of the forming process.

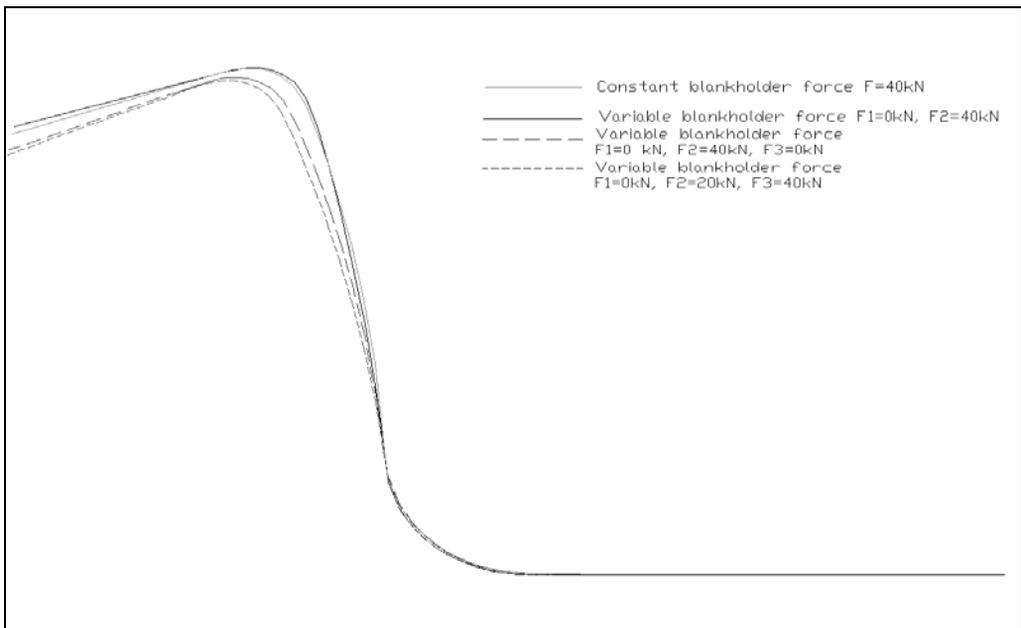


Fig. 6. Variable blankholder force

The analysis of the parts measured (Figure 6) leads to the following results and conclusions:

- In the first case, a small decrease of spring-back intensity is obtained. The use of two-step variable blankholder force leads to a higher value of sidewall curvature and smaller values of spring-back angles compared with the results of constant blankholder force.
- In the second and the third cases, the results clearly show that a constant blankholder force leads to better results.

5. Conclusions

The analysis of the experimental results highlighted the following aspects of the influence of blankholder force on spring-back:

- The increase of blankholder force results in a lower spring-back intensity. This fact is explained by stress distribution, which is more uniform through the thickness. The results obtained are in agreement with the data from literature [1], [2], [4].
- The variation of spring-back parameters is as follows: the angle at the bottom of the part, θ_1 , has decreased by 42% with the increase of the blankholder force from 5 kN to 45 kN, the angle between flange and sidewall, θ_2 , has decreased by 32%, and the sidewall curvature, ρ , has increased by 52% for increased blankholder force. Based on this variation an optimum domain of blankholder force that can be applied with beneficial effects on part shape may be determined.
- The spring-back intensity may be reduced due to application of a variable force of a blankholder. The optimum solution in this case consists in applying a blankholder force in two steps, the first starting with a small value for a small drawing depth followed by an increase of force to a value that determines the increase of all spring-back parameters. The main problem that must be solved using this method is an exact determination of the values of blankholder force and the moment of variation.

References

- [1] Samuel M.: *Experimental and numerical prediction of springback and side wall in U-bending of anisotropic sheet metals*, J. of Mat. Proc. Tech., 2000, pp. 382–393.
- [2] Liu G., Lin Z., Xu W., Bao Y.: *Variable blankholder force in U-shaped part forming for eliminating springback error*, J. of Mat. Proc. Tech., 2002, Vol. 120.
- [3] Tang C.S.: *Analysis of springback in sheet forming operation*, Advanced Technology of Plasticity, 2001, Vol. I.
- [4] Han S.S., Park K.C.: *An investigation of the factors influencing springback by empirical and simulative techniques*, Numisheet'99, Besancon, France, 13–17 September, 1999.

Badania wpływu siły dociskacza na powrotne odkształcenia sprężyste blach

Powrotne odkształcenia sprężyste są zasadniczą wadą wyrobów tłoczonych w kształcie litery U. Po usunięciu kształtujących narzędzi zmieniają się istotnie kąty pomiędzy dnem, ścianami bocznymi i kołnierzem wyrobu, a także pojawia się krzywizna ścian bocznych. Siła dociskacza jest bardzo ważnym czynnikiem decydującym o wartości sprężystych odkształceń powrotnych. W pracy przedstawiono badania wpływu siły dociskacza na zjawisko powrotnego sprężynowania wyrobów w kształcie litery U. Do badań użyto blachy ze stopu aluminium o grubości 1 mm. Siłę dociskacza zmieniano w zakresie od 0,25 do 2,06 kN, zgiębnienie stempla było stałe i wynosiło 50 mm. Stwierdzono, że zwiększenie siły dociskacza powoduje zmniejszenie kątów powrotnych odkształceń sprężystych pomiędzy dnem a ścianami bocznymi oraz ścianami bocznymi a kołnierzem, natomiast zwiększa się krzywizna ścian bocznych. Jest to wynikiem bardziej równomiernego rozkładu naprężeń wzdłuż grubości blachy.

Reliability of bridge beams with hybrid cross-sections

PAWEŁ ŚNIADY, RÓŻA SIENIAWSKA, STANISŁAW ŻUKOWSKI
Wrocław University of Technology, Wybrzeże Wyspiańskiego 25, 50-370 Wrocław

Reliability of bridge beams with hybrid cross-sections is considered. The beams made of elastoplastic material and loaded quasistatically are regarded as failure-free. Dead load and the load caused by a tram described by random variables are taken into account. Furthermore, material capacity and the dimensions of the cross-sections are also described by random values. In order to calculate the reliability shakedown, limit conditions are used. Some theoretical considerations and the results obtained are shown.

Keywords: *reliability, shakedown, hybrid cross-section, bridges*

1. Introduction

Steel bridge beams of an I-type cross-sections are often made hybrid by using materials of different properties for the flanges and the webs. Moreover, bridges are subjected to repeated load caused by a traffic flow. During many years of a bridge exploitation its overload can occur, for example, as a result of load increase, which can cause plastic strains. Therefore it is necessary to analyse the bridge condition in the elastoplastic range, which is possible thanks to the shakedown theory [1]. Furthermore, both the bridge load process and some parameters that characterize the structure are random and should be considered in the structure analysis and reliability estimation.

In the paper, an algorithm for calculating the reliability of the bridge beams with hybrid cross-sections taking into account the plastic reserve of the material according to the shakedown theory has been formulated. Random nature of the cross-section dimensions, the load and the material load-bearing capacity have also been taken into account [2], [3], [4]. As an example of the approach application, the reliability of steel bridge beams with hybrid cross-sections loaded with a tram rolling stock has been calculated.

2. Shakedown conditions of hybrid cross-section

A basic assumption of the shakedown theory is that in the range of elastoplastic work of the structure the stresses can be shown as a sum of the stresses as for the linear-elastic material of unlimited load-bearing capacity and residual stresses. It is essential that the residual stresses, which are the results of plastic strains, must be constant (invariable in time), which secures the elastic work of the structure outside the

load cycles in which the shakedown occurs. One considers the steel I-beam cross-sections of the IKSH type in which the web is made of the steel type St3S of the yield point Re_w and the flanges are made of the steel of the type 18G2 or 10HA of the yield point Re_f . The analysed cross-section is shown in Figure 1a, the graph of the normal stresses corresponding to the load with the moment M of the range $Me \leq M \leq Mo$ is shown in Figure 1b. The stresses shown in Figure 1b can be presented as a sum of elastic stresses (Figure 1c) and residual stresses (Figure 1d).

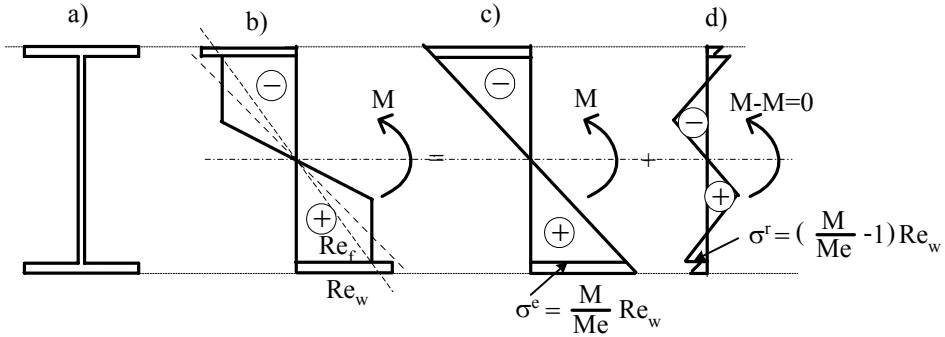


Fig. 1. Graphs of the stresses

In Figure 2, the following pictures are shown: the analysed cross-section (Figure 2a), the graph of the normal stresses corresponding to the elastic load-bearing capacity of the cross-section (Figure 2b), to the plastic load-bearing capacity (Figure 2c), to the load equal to $2Me$ assuming unlimited elastic load-bearing capacity (Figure 2d), and the normal stresses caused by the load equal to $Mo-2Me$ (Figure 2e).

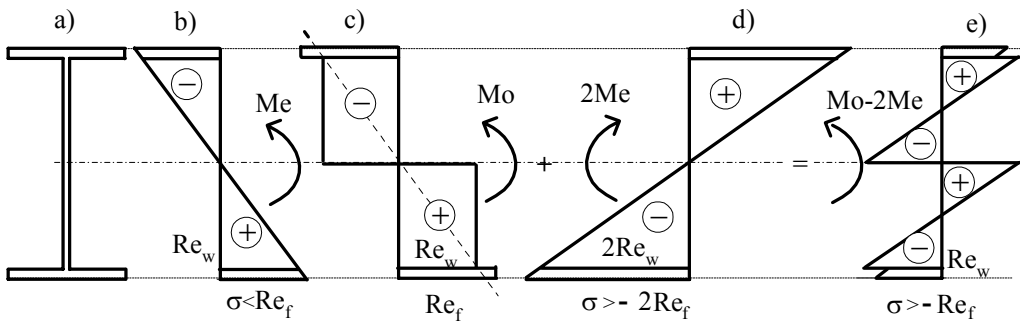


Fig. 2. Graphs of the stresses

The analysis of the stresses presented in Figure 1 and Figure 2 is followed by the assumption that the i -th cross-section will adopt to the given load if conditions (1) are satisfied

$$\begin{aligned}
 M_i^r(x) + \max_t M_i^e(x) &< Mo_i(x), \\
 -M_i^r(x) - \min_t M_i^e(x) &< Mo_i(x), \\
 \max_t M_i^e(x) - \min_t M_i^e(x) &< 2 \cdot Me_i(x),
 \end{aligned}
 \tag{1}$$

where $M_i^r(x)$ is the constant (invariable in time) residual moment corresponding to the plastic strains, $\max_t M_i^e(x)$, $\min_t M_i^e(x)$ are the extreme (in exploitation time) bending moments in the cross-section, $Mo_i(x)$ is the limit load-bearing capacity of the cross-section, $Me_i(i)$ is the so-called elastic limit load-bearing capacity of the cross-section.

Acceptable ranges of the change of the bending moment in the cross-section have been presented in Figure 3. The row (c) concerns the limit-load capacity theory $M_i^r(x) = M_i^r(x, t)$, the rows (s) concern the shakedown theory $M_i^r(x) = \text{const}$ and the row (e) concerns the elasticity theory $M_i^r(x) = 0$.



Fig. 3. Acceptable ranges of the change of bending moment in a cross-section

3. Shakedown of the system

The system is considered adaptable if conditions (1) are satisfied in each cross-section. It is sufficient for these conditions to be satisfied in the so-called critical cross-sections in which the expressions

$$\frac{M_i^r(x) + \max_t M_i^e(x)}{Mo_i(x)}, \quad -\frac{M_i^r(x) + \min_t M_i^e(x)}{Mo_i(x)} \quad \text{and} \quad \frac{\max_t M_i^e(x) - \min_t M_i^e(x)}{2 \cdot Me_i(x)}$$

take maximum values with respect to geometrical coordinates of the system. The shakedown conditions can be presented in the form

$$\max_x \left(\frac{M^r(x)}{Mo(x)} + \frac{\max_t M^e(x)}{Mo(x)} \right) < 1, \quad -\min_x \left(\frac{M^r(x)}{Mo(x)} - \frac{\min_t M^e(x)}{Mo(x)} \right) < 1, \quad (2)$$

$$\max_x \left(\frac{\max_t M^e(x)}{2 \cdot Me(x)} - \frac{\min_t M^e(x)}{2 \cdot Me(x)} \right) < 1.$$

The above conditions prove that in general the critical cross-sections could not be identified with the cross-sections in which the extreme bending moments from the elastic solution appear, which is especially significant in the case of the loads changing their locations.

Assuming that the residual stresses are self-equilibrated $\sum_i M_i^r \cdot (\varphi_{ij}^+ - \varphi_{ij}^-) = 0$, where i is the number of the critical cross-section, the two first conditions are followed by the incremental shakedown conditions (3), which must be satisfied for each possible mechanism of the plastic flow

$$\sum_i \left(\max_t M_i^e \cdot \varphi_{ij}^+ - \min_t M_i^e \cdot \varphi_{ij}^- \right) < \sum_i Mo_i \cdot (\varphi_{ij}^+ + \varphi_{ij}^-), \quad (3)$$

where $\varphi_{ij}^+, \varphi_{ij}^-$ are the strains in the yield (plastic) hinges.

In further considerations, we will use normalized safe conditions according to the shakedown theory in the form (4)

$$Y_j = \frac{\sum_i \left(\max_t M_i^e \cdot \varphi_{ij}^+ - \min_t M_i^e \cdot \varphi_{ij}^- \right)}{\sum_i Mo_i \cdot (\varphi_{ij}^+ + \varphi_{ij}^-)} < 1, \quad Y_z = \frac{\max_t M_i^e - \min_t M_i^e}{2 \cdot Me_i} < 1, \quad (4)$$

where the functions Y_j and Y_z denote normalized loads.

4. Loads

Let us consider bridge beams under the dead load (g) and the moving load caused by the tram rolling stock $Q(t)$ (Figure 4).

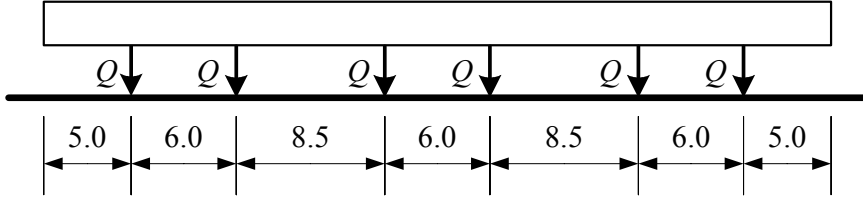


Fig. 4. Diagram of the load caused by a tram rolling stock

It has been assumed that the dead load is described by a random value of normal distribution [2], and the moving load is described by a random value of beta distribution [4]. Moving vehicles occupy each possible location on the beam, therefore in determining the maximal bending moments with respect to the geometrical coordinate the most unfavourable location of the load is assumed in a deterministic way. It is also assumed that the moving load acts statically and a dynamic influence is taken into account using a dynamic coefficient.

5. The load-bearing capacity

In relationships (4), the load-bearing capacity is expressed by the limit moments with respect to the “plastic” load-bearing capacity Mo_i and elastic load-bearing capacity Me_i , which are expressed by geometrical parameters and yield points of the material the elements are made of. The probabilistic characteristics of these moments are determined unambiguously by their joint probability density functions. These functions can be determined by recurrent application of relationships (5) to the boundary distributions of the functions of the random variables $U = U(X, Y)$, $V = V(X, Y)$:

$$f_u(u) = \int_{-\infty}^{\infty} f(x(u, v), y(u, v)) \cdot |J| \cdot dv, \quad (5)$$

$$\text{where } J = \begin{bmatrix} \frac{\partial x}{\partial u} & \frac{\partial x}{\partial v} \\ \frac{\partial y}{\partial u} & \frac{\partial y}{\partial v} \end{bmatrix} \text{ is the Jacobian of the transformation} \quad \begin{aligned} x &= x(u, v), \\ y &= y(u, v). \end{aligned}$$

6. Reliability of a system

Assuming the reliability measure as the probability that the load bearing capacity will not be exceeded, the reliability condition has the following form

$$p_r = (1 - p_f) = P\{Y < 1\} \geq 1 - p_{\text{limit}}, \quad (6)$$

where $p_f = P\{Y \geq 1\}$ is the probability of failure, and p_{limit} is the limit value of the probability of failure.

An equivalent reliability measure may also be the probability index β connected with the probability of failure by relationship (7)

$$p_f = \Phi(-\beta) = \frac{1}{2} \cdot \left(1 + \text{Erf} \left[\frac{-\beta}{\sqrt{2}} \right] \right), \quad (7)$$

where $\Phi(-\beta)$ is the cumulative distribution function of standardized normal distribution. It leads to the reliability condition

$$\beta = \sqrt{2} \cdot \text{InversErf}(1 - 2 \cdot p_f) \geq \beta_{\text{limit}}, \quad (8)$$

where $\beta_{\text{limit}} = \sqrt{2} \cdot \text{InversErf}(1 - 2 \cdot p_{\text{limit}})$.

In order to estimate the system reliability, it is indispensable to determine the probability of failure (or perhaps the reliability index) by calculating the joint probability density function of the normalized load Y . The reliability index (or perhaps the probability of failure) can be also calculated by means of FORM and SORM methods.

In the paper presented, the first approach, i.e. calculating the joint probability density function of the normalized load Y , has been applied. When the structure is loaded with two types of the loads, the normalized loads Y (4) for each failure form can be shown as

$$Y = \frac{C_g \cdot g + C_q \cdot q}{M_c}, \quad (9)$$

where C_g, C_q, C_m are the numerical coefficients, g, q, M_c describe respectively the dead load, the moving load and the limit moment with respect to the elastic or plastic load-bearing capacity. It has been assumed that these three variables are independent random variables of known probability density functions $f_g(g)$, $f_q(q)$ and $f_{M_c}(m)$. Using relationship (5) for the probability density functions of random values recurrently one obtains the relationship for calculating the probability density function of the variable Y in the form

$$f_y(y) = \left| \frac{1}{C_q} \right| \cdot \int_{-\infty}^{\infty} |m| \cdot f_{M_c}(m) \cdot \int_{-\infty}^{\infty} f_g(g) \cdot f_q \left(\frac{m \cdot y - C_g \cdot g}{C_q} \right) \cdot dg \cdot dm, \quad (10)$$

while the probability of failure is determined by the expression

$$p_f = \int_1^{\infty} f_y(y) \cdot dy. \quad (11)$$

7. Numerical analysis

In order to illustrate the approach presented, the two-span beam of the span length equal to $L = 20$ m solution has been shown. The beam is loaded with the uniformly distributed dead load and the moving load caused by tram rolling stock. The dead load is described by the normal distribution of the mean value equal to $\bar{g} = 17.5$ kN/m and the coefficient of variation equal to $V_g = 0.05$. The scheme of the moving load according to the Polish code PN-85/S-10030 (Figure 4) is built of the point forces Q , whose characteristic values are equal to $Q_k = 150$ kN. It has been assumed that this variables are described by the beta distribution with the parameters $\alpha = 2.12$, $\beta = 3.77$, their mean values are equal to $\bar{Q} = 97.6$ kN and the coefficients of variation are equal to 0.3.

$$f_q(q) = \begin{cases} 0 & \text{for } q \leq 40 \text{ kN,} \\ f_\beta(q) & \text{for } 40 \text{ kN} \leq q \leq 200 \text{ kN,} \\ 0 & \text{for } q \geq 200 \text{ kN.} \end{cases} \quad (12)$$

Two beams of different typical I-beam cross-sections, namely the beam of the type IKSH 1200×12×300×12 and the beam of the type IKSH 1300×10×400×16, have been analysed. In both cross-sections, the webs are made of the steel type St3S and the flanges are made of the steel type 18G2. It has been assumed that the yield points of each steel are random variables of normal distributions. Due to the lack of real values for such distributions it has been assumed that the mean values are equal to the minimal guaranteed values, i.e. $\bar{R}e_w = 235$ MPa and $\bar{R}e_f = 355$ MPa, respectively, and the coefficients of variation is equal to $Vr = 0.02$. The mass of the first I-beam is equal to 170.5 kg/m, while the mass of the second I-beam is equal to 211.8 kg/m. It has been assumed that the cross-section dimensions are random variables of normal distribution with the mean values given by means of describing the I-beams and the coefficients of variation equal to $V = 0.02$. For the data described above the probability density functions of the limit moments and their probabilistic characteristics have been calculated. The following mean values have been obtained for the first I-beam: $\bar{M}e = 1800$ kNm,

$\bar{M}_o = 2493$ kNm and the coefficients of variation $V_e = 0.308$, $V_o = 0.304$; for the second I-beam the mean values are as follows: $\bar{M}_e = 2585$ kNm, $\bar{M}_o = 3861$ kNm and the coefficients of variation $V_e = 0.309$, $V_o = 0.305$. In Figure 5, the calculated probability density function of plastic limit moment (solid line) and the normal probability density function (dashed line) are shown. As one can see both probability density functions are almost the same and therefore it can be assumed, with no risk of a gross error, that the limit moments are random variables of normal distribution.

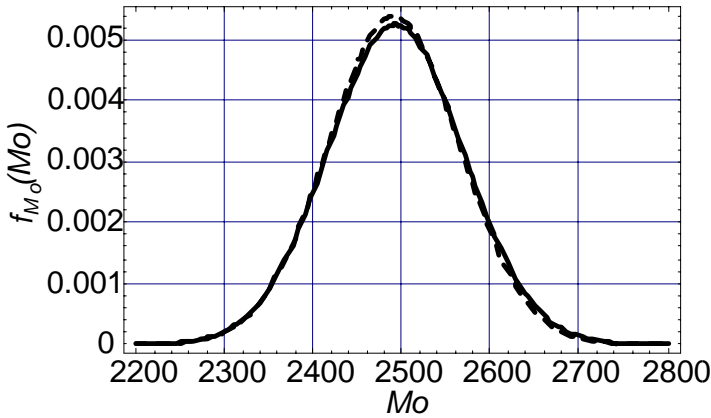


Fig. 5. The probability density functions of the limit moments

In order to verify the above assumption, the expressions $P[M \geq m] = \int_m^{\infty} f_m(m) \cdot dm$

for the real distribution (the 2-nd column of table 1) and for the normal distribution (the 3-rd column of table 1) of M have been calculated.

Table 1

m	$P [M \geq m]$	$P [M \geq m]$	Error, %
1	2	3	4
2700	0.00	0.00	26.6
2750	0.00	0.00	35.4
2800	0.00	0.00	44.5
2850	$1.3323/10^6$	$6.2055/10^7$	53.4
2900	$4.3328/10^8$	$1.654/10^8$	61.8
2950	$9.2607/10^{10}$	$2.8296/10^{10}$	69.4

In the case of the failure probabilities, the following reliability indices β would correspond.

Table 2

m	β	β	Error, %
1	2	3	4
2700	2.72	2.82	3.68
2750	3.38	3.49	3.25
2800	4.04	4.17	3.22
2850	4.70	4.84	2.98
2900	5.36	5.52	2.99
2950	6.01	6.19	3.00

As can be seen, in the range of failure probabilities the error is equal to a few dozen per cent, and in the range of reliability indices it is equal just to a few per cent. In our opinion, such an error can be treated as a real measure of the error because in the range of small probabilities the order of the quantities, not the values, is essential. For example, we assume that the structure where the failure probability equals $2/10^8$ is safe yet, the structure with the failure probability at the level of $6/10^8$ is also safe enough, though the difference between these two probabilities is equal to 200%.

In Figures 6 and 7, the probability density functions of the normalized loads Y according to the shakedown theory (solid line) and according to the elastic load-bearing capacity (dashed line) for respectively the first I-beam (Figure 6) and for the second I-beam (Figure 7) have been shown. The vertical line in Figures 6 and 7 is a limit line – the areas under the curves on its right-hand side are the measure of the probabilities of failure, and the left-hand side areas stand for the probabilities of no failure (reliability).

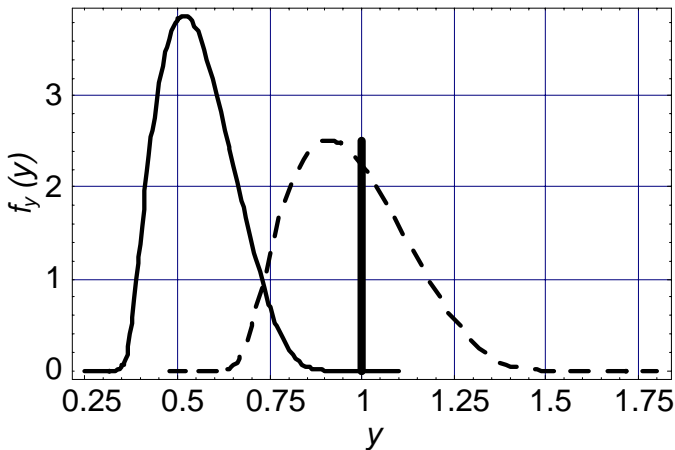


Fig. 6. The probability density functions of the normalized loads Y for the first I-beam

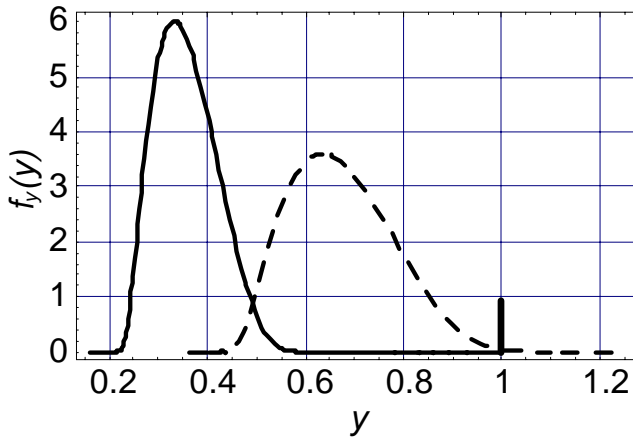


Fig. 7. The probability density functions of the normalized loads Y for the second I-beam

The following probabilities of exceeding the load bearing-capacity have been obtained for the first I-beam: according to the shakedown theory $p_f=2/10^8$ and according to the elastic load-bearing capacity theory $p_f=0.34$ and for the second I-beam $p_f=2/10^{30}$ and $p_f=4/10^6$, respectively. The first I-beam can be accepted as fulfilling the safety conditions following the shakedown theory, with a great probability however that the elastic capacity conditions are violated. The second I-beam can be accepted as fulfilling the elastic load-bearing capacity conditions with a surplus capacity according to the shakedown theory.

8. Summary

In the work presented, an algorithm for estimating the reliability of a bridge beam with a hybrid cross-section taking into account the plastic reserve of the material according to the shakedown theory has been discussed. Such an approach allows a more complete reliability analysis than in the case of the elasticity theory. One of the important elements in the reliability analysis of hybrid beams is verification of the reliability of the connection between the flanges and webs. Such calculations can be done similarly to those made for the beam's cross-section. The calculations carried out show that the structure reliability analysed according to the shakedown theory is much higher than that obtained by applying the elasticity theory. In the example presented, it allows the material saving at the level of 20%. The algorithm presented seems to be especially useful for estimating the reliability of existing structures, while the calculations carried out according to the elasticity theory give the results which do not fulfil the safety conditions.

Acknowledgement

This work was supported by the State Committee for Scientific Research in Warsaw under the grant No. 7TO7E 01418. This support is gratefully acknowledged.

References

- [1] König J.A.: *Shakedown of elastic-plastic structures*, PWN, Warszawa, 1987.
- [2] Mendera Z.: *Probabilistic theories of structure loads*, [in:] *Random loads and load bearing capacity of structures* (in Polish), Ossolineum, Wrocław, 1979, pp. 171–203.
- [3] Murzewski J.: *Probabilistic analysis and synthesis of elastoplastic structures*, [in:] *Reliability-based design of structural systems* (in Polish), PAN, Ossolineum, 1968.
- [4] Sakano M., Mikami I., Miyagawa K.: *Simultaneous Loading Effect of Plural Vehicles on Fatigue Damage of Highway Bridges, Reliability and Optimization of Structural Systems*, V (B-12), edited by P. Thoft-Christensen and H. Ishikawa, Elsevier Science Pub., 1993, 221–228.

Niezawodność belek mostowych o przekroju hybrydowym

Sformułowano algorytm umożliwiający probabilistyczną ocenę niezawodności belek mostowych o przekroju hybrydowym z wykorzystaniem rezerwy plastycznej materiału według teorii przystosowania. Uwzględniono losowy charakter wymiarów przekroju, nośności materiałów i obciążenia. Algorytm zilustrowano obliczeniami niezawodności hybrydowych stalowych belek mostowych obciążonych taborem tramwajowym.

Podstawowym założeniem teorii przystosowania, w odróżnieniu od teorii nośności granicznej, jest to, że naprężenia resztkowe będące wynikiem odkształceń plastycznych muszą być stałe (niezmiennie w czasie), co zapewnia sprężystą pracę konstrukcji poza cyklami obciążeń, w których następuje przystosowanie. Następnie przyjęto przekroje stalowe dwuteowe typu IKSH, dla których granica plastyczności materiału półki jest o tyle większa od granicy plastyczności materiału środnika, że o nośności „sprężystej” przekroju na zginanie decyduje druga z granic. Analizie poddano belki mostowe, zakładając, że działa na nie obciążenie stałe i obciążenie ruchome taborem tramwajowym złożonym z układu sił skupionych. Przyjęto, że wartość obciążenia stałego jest zmienną losową o rozkładzie normalnym, a wartość obciążenia ruchomego – zmienną losową o rozkładzie beta. Przejeżdżające pojazdy zajmują każde z możliwych położeń, dlatego wyznaczając ekstremalne momenty zginające, przyjęto najmniej korzystne położenie względem współrzędnej geometrycznej w sposób deterministyczny. Dynamiczny charakter działającego obciążenia uwzględniono we współczynniku dynamicznym.

Nośność układu jest reprezentowana przez momenty graniczne ze względu na nośność „plastyczną” Mo_i i nośność „sprężystą” Me_i . Momenty te są funkcjami parametrów geometrycznych przekroju i granic sprężystości materiału. Charakterystyki probabilistyczne tych momentów są jednoznacznie określone przez ich łączne funkcje gęstości rozkładów prawdopodobieństwa. Jako miarę niezawodności przyjęto prawdopodobieństwo nieprzekroczenia nośności oraz sprzężony z nim wskaźnik niezawodności β . Prawdopodobieństwo awarii wyznaczono, budując funkcję gęstości rozkładu łącznego obciążenia unormowanego.

Influence of structure on strain-rate sensitivity index at hot forming of steel

IVO SCHINDLER

Institute of Modelling and Control of Forming Processes, VSB, Technical University of Ostrava, 17. listopadu 15, 708 33 Ostrava, Czech Republic. E-mail address: ivo.schindler@vsb.cz

EUGENIUSZ HADASIK

Department of Mechanics and Metal Forming, The Silesian University of Technology, Krasińskiego 8, 40-019 Katowice, Poland

The methodology of determination of strain-rate sensitivity index was developed based on rolling of a set of samples with the same draught but different speed at a defined temperature. It was shown that an initial grain size has nearly negligible influence on the variable investigated, in contrast to phase composition whose influence is considerable.

Keywords: *steels, hot working, microstructure, phase transformations*

1. Introduction

Strain-rate sensitivity m of steels has been a traditional object of extensive research. It can be applied in the description of hot and/or warm deformation behaviour (flow stress), e.g. [1]–[3]. The efficiency of power dissipation given by $2m/(m + 1)$ can be plotted as a function of temperature and strain rate which allows us to draw a processing map, being interpreted on the basis of the dynamic model of materials [4]. Accurate strain-rate sensitivity measurements have been used for determining the solid solution component of interstitials in ferritic stainless steel [5]. High strain-rate sensitivity value plays a key role in superplasticity of duplex stainless steel [6] as well as in superplastic-like deformation behaviour during creep deformation [7]. Of course, there exist even some extraordinary functions of the m -value. The effects of strain hardening and strain-rate sensitivity on the plastic flow and deformation inhomogeneity during equal-channel angular pressing were studied [8]. Steel foams fabricated in a powder metallurgical process were subjected to compression tests to explore the dependence of defects on strain-rate sensitivity [9]. The influence of friction coefficient on material strain-rate sensitivity was assessed by dynamic friction measurements at sliding velocities representing the high-speed machining processes [10], etc.

In former experimental works [11], [12], a combined influence of mean strain rate $\dot{\epsilon}$ [s^{-1}] and temperature T [K] on mean deformation resistance σ [MPa] of various types of steel was studied. At the same time a universal validity of a simple model for

mean deformation resistance was verified, particularly of its member for speed expressed in the form of

$$\sigma \approx \dot{\epsilon}^m, \quad (1)$$

where m is strain-rate sensitivity index dependent on a temperature according to the following relationship

$$m = D - F/T, \quad (2)$$

where D and F are material constants. The laboratory rolling mill Tandem with computer-aided registration of experimental data was used for this purpose [13].

2. Experimental procedure

Coincident samples belonging to one set are rolled with the same draught but various speed at selected temperature levels. For each draught mean values of the rolling force F [kN] and/or the revolutions of rolls N [rev/min] are evaluated; of course, revolutions are not constant during the pass (Figure 1). Variables σ and $\dot{\epsilon}$ in Equation (1) are substituted for variables F and N . In reference [44], mathematical proofs of justification of this simplifying procedure are given. This procedure assumes a linear relationship between strain rate and mean deformation resistance in the region of strengthening (at comparatively small strains).

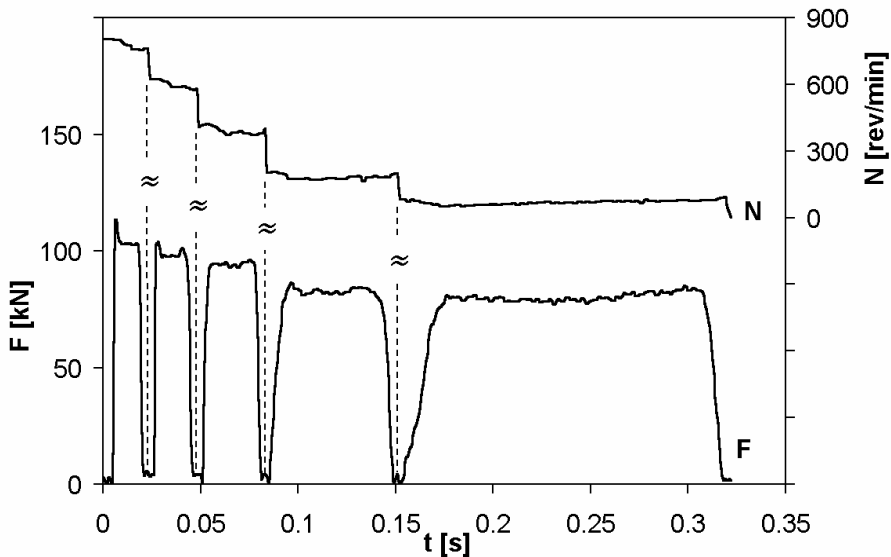


Fig. 1. Example of the course of rolling forces in relation to fluctuating rolling speed (tool steel, identical reduction, temperature of 950 °C; in reality, individual draughts do not link to each other so quickly, long dwells have been removed in the plot)

Determination of the material constants D and F requires that two types of regression have to be accomplished. First of all the values of index m are found out for individual temperature levels by means of the procedure shown in Figure 2 (an exponential relationship). Then temperature relationship of strain-rate sensitivity index m is determined after plotting the values m (acquired in this way) in the graph, which is shown as an example in Figure 3 (a linear regression).

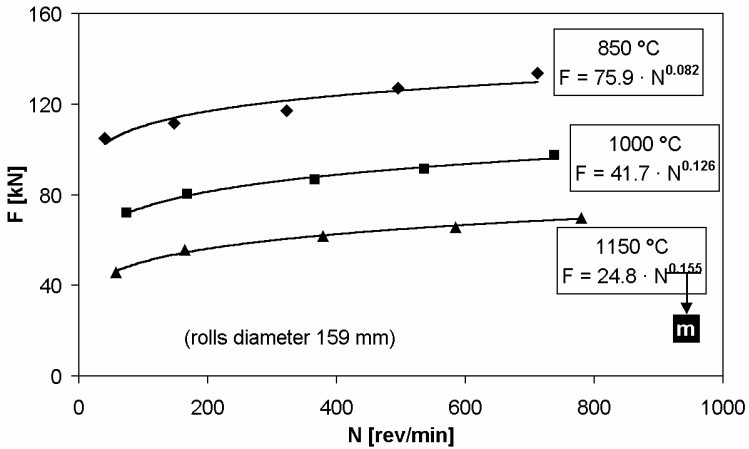


Fig. 2. Determination of strain-rate sensitivity index values from rolling forces measured at individual temperature levels (low-alloyed steel with Cr)

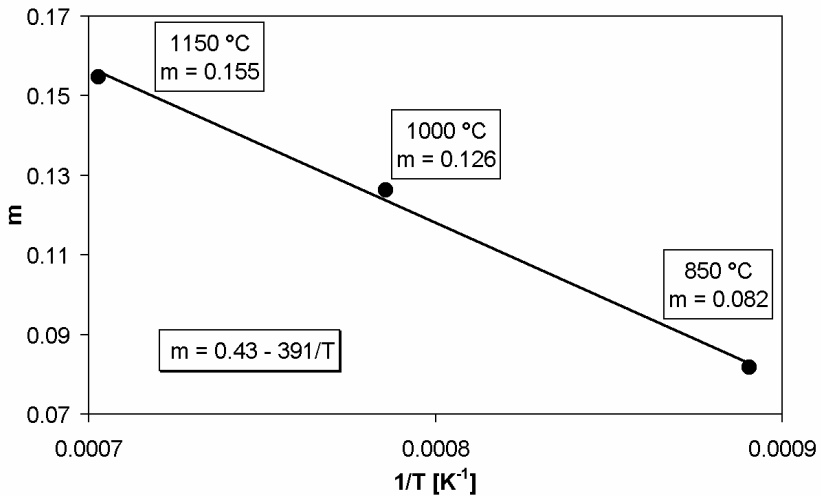


Fig. 3. Determination of temperature relationship of strain-rate sensitivity index m (values transferred from Figure 2)

The aim of this stage of the work was to find out to what extent the value of strain-rate sensitivity index m is influenced by the state of material structure – its phase composition and initial grain size.

3. Results and discussion

3.1. Impact of phase transformations

For the evaluation of the impact of structural state, ELC steel has been chosen (Table) because it changes fundamentally in the temperature course of rolling forces in the region of transformations A_{r3} and A_{r1} [15]. In Figure 4, impact of structural state on hot deformation resistance is demonstrated. When determining the values of strain-rate sensitivity index m , forming temperatures were selected in such a way that rolling with the same draught was always realized in the phase-defined region. Three temperature levels were selected for the austenite region: 1200 °C, 1075 °C, and 950 °C. In the two-phase and purely ferritic region, rolling was realized at two temperature levels: 870 °C and 820 °C – for the mixed structure region – or 750 °C and 650 °C – for the ferritic region. Data representing calculated values of strain-rate sensitivity index were then added to the summary plot in Figure 4.

Table. Chemical composition (wt %) of the steels used

Steel	C	Mn	Si	P	S	Cr	Ni
ELC	0.013	0.33	0.07	0.006	0.009	0.05	–
18/9-S	0.055	1.52	0.46	0.035	0.248	17.84	8.97

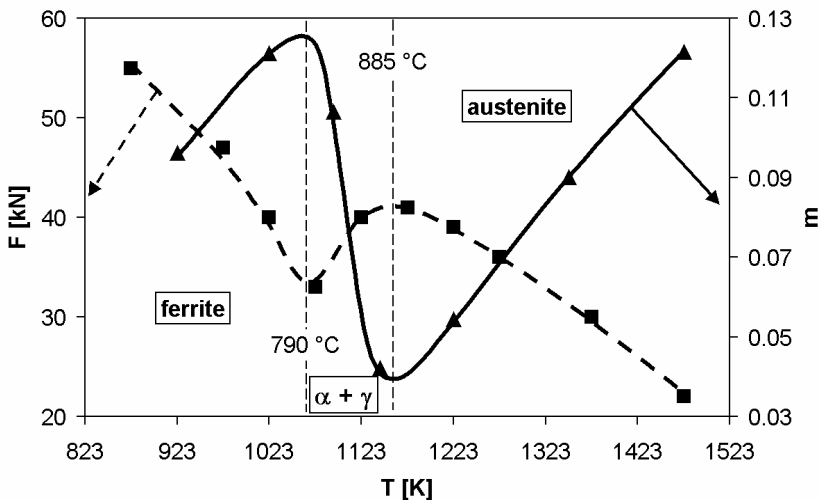


Fig. 4. Impact of temperature and phase composition of ELC steel on rolling forces and values of strain-rate sensitivity index m

The direction of inclination of the curve $m=f(T)$ in both monophasic regions is qualitatively identical. On the contrary, the inclination in the two-phase ferritic-austenitic region has the opposite direction. Temperature relationships of strain-rate sensitivity index for the given ELC steel in all three-phase regions (concerning only linear sections of pertinent curves) could be described by the following simple linear regressions:

$$m = 0.45 - 484/T \quad \text{for austenite,} \quad (3)$$

$$m = 1911/T - 1.64 \quad \text{for austenite + ferrite,} \quad (4)$$

$$m = 0.39 - 272/T \quad \text{for ferrite.} \quad (5)$$

From what was stated above there follows the importance of selection of experimental temperatures in determination of strain-rate sensitivity index m , because the data achieved at the temperature corresponding to another structural state will cause significant falsification of results.

3.2. Impact of grain size

Samples from free-cutting steel of the type 18/9-S (see Table 1) were soaked at a temperature of 1275 °C, and then rolled with the same draught but various speed at a temperature of 1000 °C, or heated directly to the rolling temperature of 1000 °C. The initial size of austenitic grain is demonstrated by micrographs in Figure 5. Dark points or stretched aggregates in streaks are sulphides (MnS). Their orientation corresponds to the direction of rolling of the initial block. Grains after laboratory heating and quenching of the sample are equiaxed. Their mean diameter is ca 0.2 mm after heating to 1275 °C, or 0.03 mm after heating to 1000 °C. The plot in Figure 6 demonstrates the effect of an initial grain size (in different order of magnitude) on strain behaviour of particular steel. The value of strain-rate sensitivity index at a forming temperature of 1000 °C ($m_{1000} = 0.07$ or 0.08) fluctuates in the range of statistical error which is quite usual at hot testing used. It follows from this that it is possible to take no account of the impact of grain size on the value of strain-rate sensitivity index m in calculations of deformation resistance and rolling force in practice.

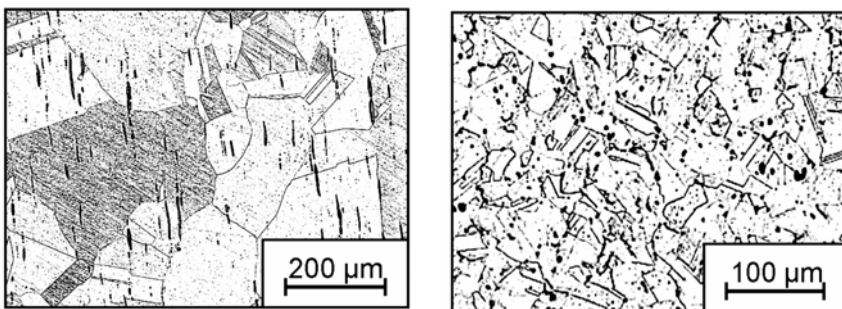


Fig. 5. Grain size of austenitic steel 18/9-S after heating to 1275 °C (on the left) or 1000 °C (on the right)

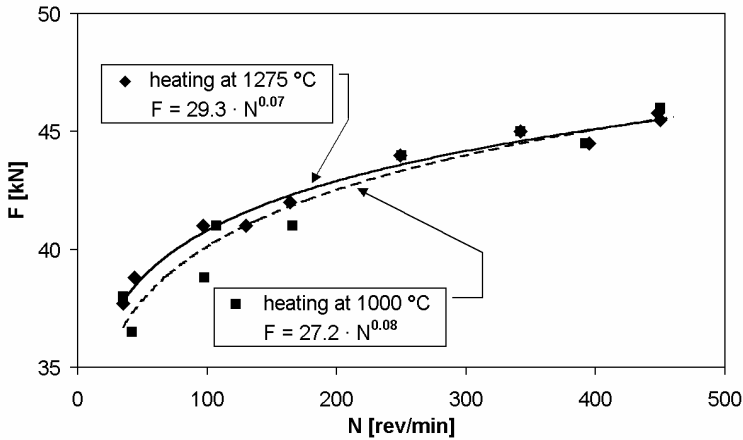


Fig. 6. Impact of initial grain size on rolling forces and value of strain-rate sensitivity index m during forming of steel 18/9-S at a temperature of 1000 °C

4. Summary

It is necessary to stress that Equation (2) may exclusively be applied to the description of strain behaviour of particular steel in the region of qualitatively identical phase composition, most often in the region of austenite. In case a given steel exhibits the phase transformation (e.g. austenite/ferrite), validity of the derived relation is principally limited to the temperature region above a temperature A_{r3} . As it was proved by the research into strain behaviour of ELC steel, the tendency of temperature relationship $m = f(T^{-1})$ is the same in the austenitic and ferritic regions, but quite opposite in the two-phase region of the co-existence of austenite and ferrite.

The experiments showed only very weak impact of grain size on strain behaviour of corrosion-resistant austenitic steel. Adaptive control of rolling mills can normally work with deviations of real versus predictable values of mean deformation resistance or rolling force by more than 10%. From this point of view it is legitimate to neglect in practical calculations the impact of grain size on the value of strain-rate sensitivity index and forming force as well.

Acknowledgements

Development of necessary laboratory equipment and experimental works were performed under financial support of MSMT ČR (projects MSM 273600001 and LN 00B029).

References

- [1] Maehara Y.: *Effect of Microstructure on Hot Deformation in Duplex Stainless Steels*, Scripta Metallurgica et Materialia, 1992, Vol. 26, No. 11, 1701.

- [2] Jaipal J. et al.: *Work hardening and strain rate sensitivity of 0.06 wt.% C steel*, Proc. of the Biennial Materials Conference of the Institute of Materials Engineering, Wollongong University Press, 1998, Vol. 2, 541.
- [3] Gilat A., Wu X.: *Plastic deformation of 1020 steel over a wide range of strain rates and temperatures*, International Journal of Plasticity, 1997, Vol. 13, No. 6–7, 611.
- [4] Venugopal S., Mannan S.L., Prasad Y.V.R.K.: *Influence of State of Stress on the Processing Map for Hot Working of Stainless Steel Type AISI 304L: Compression vs. Torsion*, Materials Science and Engineering A, 1993, Vol. A160, No. 1, 63.
- [5] MacDonald W.D., Carpenter G.J.C., Saimoto S.: *Using strain rate sensitivity measurements to determine phase relations in A430 stainless steel*, Materials Science and Engineering A, 1995, Vol. 190, No. 1–2, 33.
- [6] Song J.L., Blackwell P.L.: *Superplastic behaviour of commercial duplex stainless steel SAF 2304*, Materials Science and Technology, 1999, Vol. 15, No. 11, 1285.
- [7] Lee S.C., Kim Y.H., Lee Y.D.: *Analysis of creep deformation behaviors of type 2205 duplex stainless steel under continuous annealing conditions*, Journal of Materials Processing Technology, 2002, Vol. 123, No. 1, 185.
- [8] Kim H., Hong S.I., Seo M.H.: *Effects of strain hardenability and strain-rate sensitivity on the plastic flow and deformation homogeneity during equal channel angular pressing*, Journal of Materials Research, 2001, Vol. 16, No. 3, 856.
- [9] Park C., Nutt S.R.: *Strain rate sensitivity and defects in steel foam*, Materials Science and Engineering A, 2002, Vol. 323, No. 1–2, 358.
- [10] Espinosa H.D., Patanella A.J., Fischer M.: *Dynamic friction measurements at sliding velocities representative of high-speed machining processes*, Journal of Tribology (Transactions of the ASME), 2000, Vol. 122, No. 4, 834.
- [11] Radina M. et al.: *Verifikace modelu deformačních odporů v podmínkách vysokorychlostního válcování oceli za tepla*, Proc. of FORMING 99, Silesian Technical University, Katowice, 1999, 196.
- [12] Schindler I. et al.: *Deformační odpory při vysokorychlostním válcování oceli za tepla*, Hutnicke listy, 2001, Vol. 56, No. 6–7, 67.
- [13] Schindler I. et al.: *Optimization of the hot flat rolling by its modelling at the laboratory mill Tandem*, Proc. of the 6th International Conference on Technology of Plasticity, Springer-Verlag, Berlin, 1999, Vol. 1, 449.
- [14] Radina M. et al.: *Strain Rate Sensitivity of Steels: Influence of Chemical Composition, Structure and Temperature*, Proc. of FORMING 2000, Silesian Technical University, Katowice, 2000, 137.
- [15] Schindler I. et al.: *Vliv dotvarecí teploty na strukturu IF oceli*, Proc. of METAL 2000, Tanger Ostrava, 2000, Paper No. 227.

Wpływ struktury na wskaźnik czułości naprężenia na prędkość odkształcenia podczas przeróbki plastycznej na gorąco

Opracowano metodę wyznaczania wskaźnika czułości naprężenia na prędkość odkształcenia, opierając się na wynikach walcowania na gorąco zestawu próbek dla zadanych temperatur i prędkości walcowania i zachowując stały gniot. Badania realizowano dla zróżnicowanych wartości prędkości odkształcenia i temperatury oraz dla różnych typów stali. Stwierdzono, że

początkowa wielkość ziarna praktycznie nie ma wpływu na wyznaczony wskaźnik czułości naprężenia na prędkość odkształcenia, znaczny jest natomiast wpływ składu fazowego stali. Dla wybranych grup stali opracowano uniwersalne równania, które z dobrą dokładnością opisuje wpływ temperatury i składu chemicznego, wyrażonego przez równoważnik niklu, na wskaźnik czułości naprężenia na prędkość odkształcenia podczas walcowania na gorąco.

The improvement in fatigue characteristic of sintered steel by vacuum carburizing

KRZYSZTOF WIDANKA

Wrocław University of Technology, Wybrzeże Wyspiańskiego 25, 50-370 Wrocław

The P/M low-alloy steel with sintered density of 7.0 g/cm^3 was surface hardened by means of vacuum carburizing method. The fatigue strength of steel in case-hardened and sintered state was determined. Fatigue tests were conducted in the axial loading mode ($R = -1$, $f = 25 \text{ Hz}$) on unnotched specimens. Comparing the $S-N$ curves obtained for case-hardened and sintered specimens, the influence of vacuum carburizing on fatigue limit of examined steel was estimated.

Keywords: *fatigue strength, sintered steel, vacuum carburizing*

1. Introduction

Recently an enormous advance in the production of sintered steel parts intended for long-term cyclic load service has been observed. The automotive, engineering, aircraft and electrical industries are the most representative examples of the trend. Static properties of sintered steels are usually close to those found in conventional steels. Fatigue properties, however, fail to repeat this pattern. They are highly dependent upon density (porosity) which in turn is affected by powder parameters, pressing and sintering conditions, alloying additions and temperature of sintering. A significant improvement of fatigue strength can be obtained by the post-sintering treatment, especially by the thermochemical operations. Among them, carburizing is the one that produces the best results as far as the core–surface interactions are concerned. In the carburizing of sintered components, the vacuum carburizing is a good alternative to the traditional gas treatment [1]–[3].

Evaluation of the effect of chemical composition and manufacturing process parameters on fatigue strength, understanding the phenomena underlying fatigue failure in sintered parts and, finally, reliable life prediction techniques have become recently the most challenging research objective. The present study was aimed at determining the effect of vacuum carburizing on the fatigue strength of selected P/M steel.

2. Experimental

Test specimens were prepared of Hoeganaes iron powder grade ASC100.29 and Mn, Cr, Mo elementary powders with addition of graphite and lubricant to nominal “green” density of 7.0 g/cm^3 . The chemical composition and static properties of speci-

mens sintered at 1170 °C for 60 minutes in an atmosphere consisting of 90% of N₂ and 10% of H₂ are given in Table.

Vacuum carburizing was performed in a laboratory vacuum furnace (Seco/Warwick) according to diagram shown in Figure 1 in propan atmosphere with the working pressure of 20 hPa. Process parameters (carburizing temperature: 1040 °C; total carburizing time: 40 minutes) were selected in such a way as to obtain the surface carbon content of 0.8% and about 1.1 mm case depth. After carburizing the specimens were subsequently oil-quenched at 830 °C and tempered for 120 minutes at 140 °C in the air.

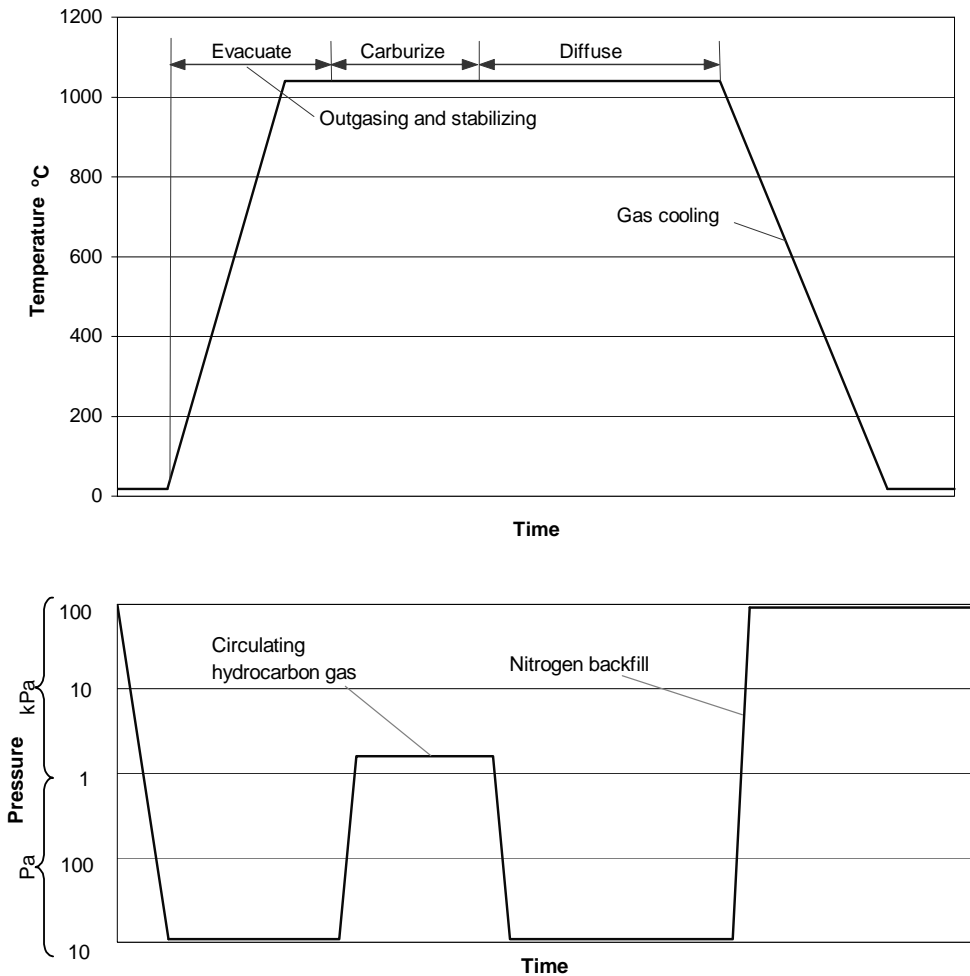


Fig. 1. Vacuum carburizing process (scheme)

Table. Chemical composition (wt. %) and static properties of sintered specimens

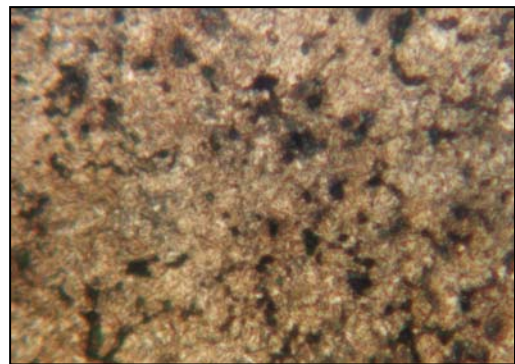
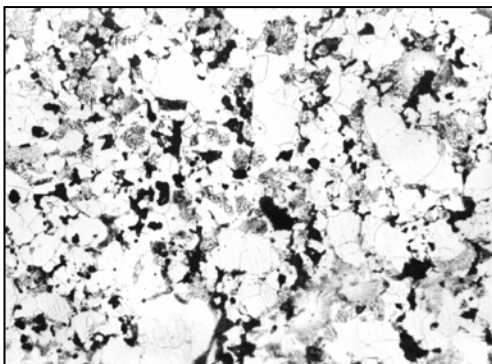
C [%]	Mn [%]	Cr [%]	Mo [%]	Fe [%]	UTS [MPa]	$\sigma_{0.2}$ [MPa]	A [%]
0.21	0.64	0.45	0.4	Balance	280	160	6.2

The microstructure investigations were carried out with the use of light microscope. The unnotched specimens (in the form of standard test specimens according to ISO 2740) were subjected to alternating tension–compression ($R = -1$, $f = 25$ Hz) under stress amplitude control. A sinusoidal loading spectrum was applied. The tests were conducted on a hydraulic MTS-810 pulsar in the finite and high-cycle fatigue range, with 5 specimens for each stress level in order to determine the S – N curve and the fatigue limit σ_{aE} at the assumed endurance $N_E = 2 \cdot 10^7$ cycles. The S – N curve is presented in terms of the nominal stress amplitude σ_{an} and the cycles to failure N_f (log). A mean slope k of the S – N curve with the survival probability of $P_s = 50\%$ was calculated.

3. Results and discussion

3.1. Microstructure

The microstructure of sintered specimens consisting of ferrite and pearlite areas was shown in Figure 2. Figure 3 presents the case microstructure obtained after vacuum carburizing and subsequently hardening and tempering. Its main element is the martensite with low content of retained austenite (about 8 percentage estimated by means of X-ray diffraction analysis). The microstructure of examined steel as sintered and as case hardened in more detail was discussed [3], [4]. The hardness of case was also determined and the obtained microhardness profile is presented in Figure 4.

Fig. 2. Microstructure of sintered specimens (100 \times)Fig. 3. Case microstructure of specimens (500 \times)

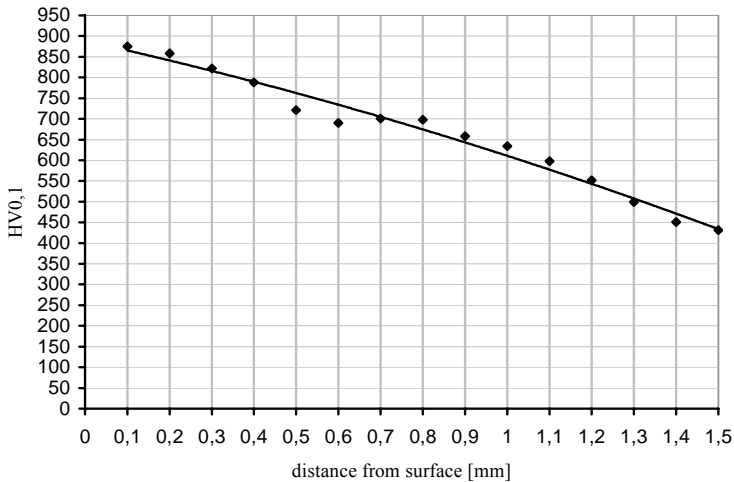


Fig. 4. The representative microhardness profile in the case of treated specimens

3.2. Fatigue strength

The $S-N$ curves plotted on the basis of experimental results of fatigue tests obtained for plain specimens as case hardened as well as sintered are shown in Figure 5. The fatigue limits estimated from these $S-N$ curves are equal to 160 MPa and 80 MPa for case hardened and sintered specimens, respectively. These values show that the use of vacuum carburizing method for producing the hardened surface layer containing highly compressive residual stresses allows obtaining a hundred-per-cent increase in the fatigue limit of the examined steel. They confirm also the well-known fact that surface hardening techniques produce a beneficial effect on improvement of fatigue strength of porous and non-porous steels. With regard to vacuum carburizing of P/M steels, this effect, and exactly the influence of mentioned treatment on fatigue behaviour of sintered low-alloyed steels, has been discussed in [3], [5], [6]. In comparison with the results obtained for plain specimens tested in direct stress by other investigators [7], [8], who have found that the increase of endurance limits was in the range of 10–30 and 50–100 per cent for heat treated and case hardened alloyed P/M steels, respectively, this growth of 100 per cent in fatigue limit of examined steel is very promising. This twofold increase in the fatigue limit was obtained as the ratio of the hardness of the surface to that of the core equal to 3.03 and as the ratio of the case depth to specimen diameter (thickness) equal to 0.183. It's common knowledge that the fatigue limit of case-hardened steels (wrought and sintered) depends on a lot of factors, and some of them are given above. For example, for wrought steels the maximum fatigue limits reported in [9] correspond to the values of this latter ratio of 0.01–0.2, depending on the steel and case-hardening technique. At present, these similar examination results do not exist for sintered steels.

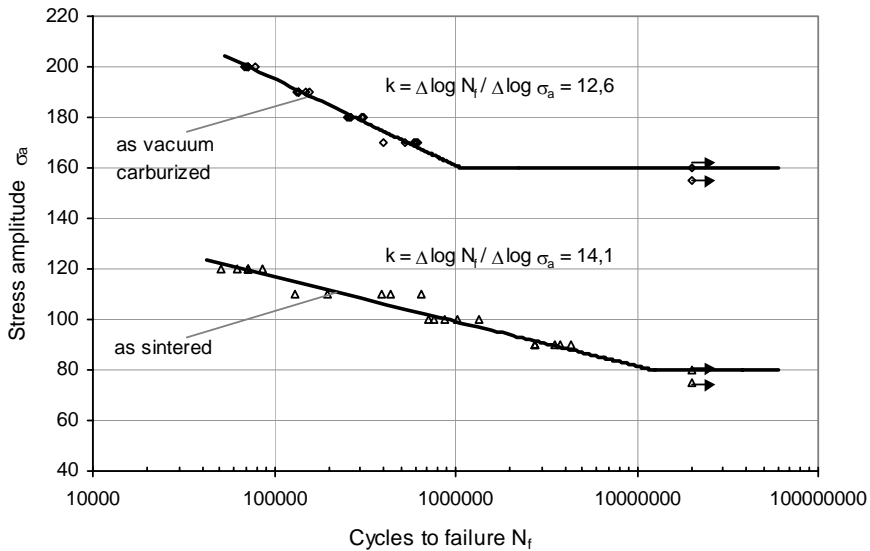


Fig. 5. The direct stress S - N curves for examined sintered steel as sintered and as case hardened

4. Conclusions

The use of vacuum carburizing method to produce the hardened surface layer on the sintered steel being examined significantly improved its fatigue characteristic. After the treatment proposed the fatigue limit increases from 80 MPa (as sintered) to 160 MPa (as case hardened).

The results obtained show that vacuum carburizing as the method used for improving fatigue limit is very effective and may be applied, also due to the other advantages [1]–[4], to the components manufactured by P/M technology.

References

- [1] Rosso M., Scavino G., Ubertaini G., Drozda M.: *Surface Hardening of P/M Steels by Vacuum and Glow Discharge Carburizing*, Proc. Conf. International Conference Secondary Operations, Quality and Standards, MPIF Princeton, 1992, Vol. 4, pp. 25–39.
- [2] Rosso M., Scavino G., de Rege A., L'Esparance G., Hong B.D.: *Low Pressure and Plasma Carburizing of Ni, Mo, Mn Alloyed P/M Steels*, Advances in Powder Metallurgy and Particulate Materials, Princeton, NJ, 1996, Vol. 4, pp. 13–235-13–247.
- [3] Widanka K.: *Vacuum Carburizing of Sintered Steels*, Ph. D. Thesis, Wrocław University of Technology, 2002.
- [4] Widanka K., Dudziński W.: *The surface layer of the P/M alloy steel after vacuum carburizing and gas quenching*, Proceedings of European Congress on Powder Metallurgy PM2001, 2001, Vol. 4, pp. 357–362.

- [5] Widanka K.: *Effect of case microstructure on fatigue behaviour of vacuum carburized sintered steel*, DF PM 2002 Proceedings, Stara Lesna, Slovak Republic, 2002, Vol. 2, pp. 18–21.
- [6] Widanka K., Kaleta J.: *The effect of vacuum carburizing on cyclic properties of sintered low-alloyed steel*, The 19th Symposium on Experimental Mechanics of Solids, Jachranka, 2000, pp. 549–553.
- [7] Sonsino C.M.: *Einfluss verschiedener Wärmebehandlungsverfahren auf die Schwingfestigkeit von Sinterstählen*. Mat.-wiss. und Werkstofftechnik, 1991, 22, pp. 308–315.
- [8] Sonsino C.M., Schlieper G.: *Improvement of Mechanical Properties of Diffusion and Prealloyed Sintered Steels by Heat Treatments*, Powder Metallurgy, 1992, Vol. 24, No. 6, pp. 339–344.
- [9] Tauscher H.: *Symposium on fatigue damage in machine parts*, 1960, Prague, pp. 238.

Poprawa charakterystyki zmęczeniowej stali spiekanej przez nawęglanie próżniowe

Przedstawiono sposób poprawienia charakterystyki zmęczeniowej niskowęglowej i nisko-stopowej stali spiekanej o gęstości $7,0 \text{ g/cm}^3$. Poprawę wytrzymałości zmęczeniowej na rozciąganie–ściskanie osiągnięto dzięki zastosowaniu nawęglania próżniowego połączonego z hartowaniem i niskim odpuszczaniem. Proces nawęglania według tak dobranych parametrów, aby otrzymać założone parametry warstwy wierzchniej, prowadzono w laboratoryjnym piecu próżniowym (Seco/Warwick) typu V3/2. Wykorzystano tu własne oprogramowanie do sterowania i kontroli przebiegu procesu. Próby zmęczeniowe przeprowadzono na pulsatorze hydraulicznym MTS 810 w warunkach wahadłowego rozciągania–ściskania ($R = -1$, $f = 25 \text{ Hz}$) próbek płaskich bez karbu o kształcie i wymiarach zgodnych z normą PN-86/H-04937. Wyniki prób na próbkach w stanie spiekającym i utwardzonym powierzchniowo przedstawiono w postaci krzywych Wöhlera na wykresie w skali półlogarytmicznej i wyznaczono wartości wytrzymałości na zmęczenie materiału w stanie spiekającym i obrabionym. Porównując otrzymane wartości, stwierdzono, że w wyniku zastosowania wspomnianej obróbki nastąpił 100-procentowy wzrost wytrzymałości zmęczeniowej z 80 MPa dla stanu spiekanego do 160 MPa dla stanu utwardzonego powierzchniowo. Uzyskany rezultat wskazuje na bardzo korzystny wpływ tej metody nawęglania próżniowego na poprawę charakterystyki zmęczeniowej badanej stali i jednocześnie potwierdza celowość jej stosowania – także ze względu na inne jej zalety szczególnie istotne w przypadku porowatości otwartej [1]–[3] – do stalowych wyrobów spiekanych.



A contribution to optimal loading/unloading performance in automatic press feeding: the MANPRESS robot

J. FALCÃO CARNEIRO, A. PESSOA DE MAGALHÃES, F. GOMES DE ALMEIDA

Departamento de Engenharia Mecânica e Gestão Industrial da Faculdade de Engenharia da Universidade do Porto, Rua Dr. Roberto Frias 4200-465 Porto Portugal.

Tel: +351 22 508 14 00; Fax: +351 22 508 14 40

Instituto de Engenharia Mecânica, IDMEC, Pólo FEUP, Portugal

A. BARATA DA ROCHA

Instituto de Engenharia Mecânica e Gestão Industrial, INEGI, Portugal, E-mail addresses: {jpbrfc.apmag.fga.abrocha}@fe.up.pt

Departamento de Engenharia Mecânica e Gestão Industrial da Faculdade de Engenharia da Universidade do Porto, Rua Dr. Roberto Frias 4200-465 Porto Portugal.

Tel: +351 22 508 14 00; Fax: +351 22 508 14 40

This paper presents the MANPRESS robot: a simple, low-cost and newly developed industrial device primarily devoted to press feeding. This robot exhibits two major features: great flexibility to accommodate different machines and products, and optimal performance in loading/unloading one or more machines. The first is due to the usage of modular, off-the-shelf and easy to control system components. The second is the result of the devising and implementing modern control algorithms derived from discrete event-systems theory. Loading/unloading strategies that can be used in automatic press feeding and their associated performance are considered to be an actual and important subject, but seldom noticed in current scientific literature. Contributing to fill this gap, this is the major subject of the present paper. A case study is provided illustrating the theory developed. Moreover, the same case study shows that in a realistic scenario a gain in performance of 15% can be easily achieved when the proper loading/unloading strategy is used. However, and in practice, such a benefit can only be attained from a simple to control and very flexible loading/unloading device such as the MANPRESS robot. Thus, the main mechanical and control features of the robot are also described in this paper.

Keywords: strategies for machine loading/unloading, performance analysis, flexible manufacturing cells, intelligent processing of materials

1. Introduction

In modern manufacturing, two major requirements for automated loading/unloading devices are high productivity and great flexibility to accommodate both different machines and products. Manufacturing plants based on industrial robots are highly flexible in terms of machine and product accommodation. Yet, the price to pay is only acceptable for high-scale production. Made-to-order devices are usually less expensive than industrial robots, but their low flexibility to accommodate different products is often a severe limitation to productivity. As such, it is very pertinent to design and develop new automated loading devices providing

both flexibility and low cost. The system developed at INEGI, named MANPRESS and primarily devoted to press feeding, tries to overcome the mentioned problems: it represents a low-cost solution with excellent modularity and accommodation features.

High performance is another crucial issue for modern industry. This paper considers the performance of a manufacturing cell where one or more robots load one or more machines with raw parts and later unload the machined parts. As usual, the performance of the cell is measured by its cycle time, i.e., the time to produce two consecutive parts — see [2] and [3] for details on common performance metrics. Accepting this metrics, one finds that sequences of operation requiring synchronization between devices (a robot and a press, for example) may lead to the poor timing performance of a manufacturing cell. This is particularly notorious when the co-operating devices always work in opposition, i.e., one is idle when the other performs its job. It is therefore important to devise sequences of operations (strategies) that may minimize machine and robot idle times due to synchronization constraints.

Several loading/unloading strategies for press feeding do exist and are presented in this paper. It is also shown that the timing performance of each strategy depends on the time a machine takes to produce a part. However, a central issue is the flexibility of the robotic feeding device to easily execute different sequences of movements, and gracefully cope with mode changes whenever required. As a consequence, the flexibility and the organization of robot controllers' are another fundamental issues. In the case of the MANPRESS robot, a supervisory controller that can devise and impose the best loading/unloading strategy and a logic controller for direct control are required. However, they are both simple and inexpensive.

As far as the authors know, no studies similar to this exist. In [4], several analytical methods based on queuing theory are proposed. The aim is to measure the performance of a cell consisting of three machines and one device that loads and unloads them. In [5] and [6], a general-purpose system consisting of two processes and one shared resource is studied. Here, the aim is to define the sequence of allocation of the resource to the processes such that the idle time of the resource is minimized. The main goal of the present work is therefore distinct from those usually found in manufacturing literature: it assumes a process requiring two resources and tries to minimize the idle time of both, optimizing thus the cycle time of the system.

This paper is organized as follows: Section 2 portrays the MANPRESS robot describing and discussing its most important features. Section 3 presents several loading/unloading strategies showing their impact upon the timing performance of a manufacturing system. This view is illustrated at the end of section 3, where an application example relating the MANPRESS robot is presented. Section 4 discusses the design of the supervisory and direct controllers used in the MANPRESS robot. Section 5 ends the paper highlighting its main conclusions.

2. The MANPRESS robot

Press systems underwent major improvements over the last decades leading to a growing automation of the loading processes since they directly affect safety and productivity issues. The feeding processes heavily depend on the type of product to be manufactured, although one can classify them in two types: feeding by coils and feeding blank by blank. Feeding by coils presents several advantages in terms of productivity and safety. Nevertheless, its application is somehow limited for cutting jobs using progressive tools due to specific product and tool shapes. The system developed in this work is devoted to blank by blank feeding.

The most important requirements of loading/unloading press systems were determined with two main surveys. One identified the state-of-the-art of commercial systems by means of several visits to national and international sheet metal automation fairs. The other identified the crucial features that small/medium sheet metal industries require. In this last survey, several representative industries were inquired. The results (see [1] for more details) showed that there is a strong need for low priced and flexible automation systems. The prototype system developed at INEGI was designed to provide those features.

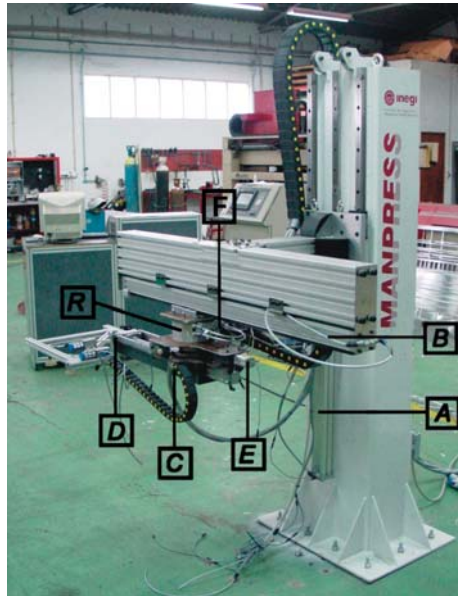


Fig. 1. The MANPRESS robot

The developed system (see Figure 1) has seven pneumatic actuators allowing three degrees of freedom. Actuators A, B, C, D, E, F are linear and Actuator R is angular. These actuators are designed to offer different modules of movements.

Actuator D allows movements along the ZZ axis to place the blank on the tool (Figure 2).

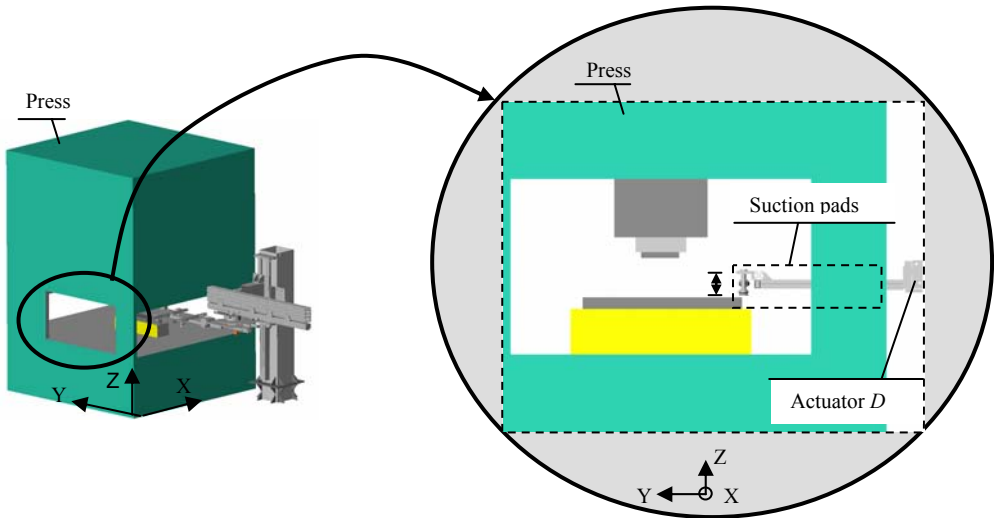


Fig. 2. Movements provided by Actuator D

Let Actuator D and the suction pads system be named Module 1. Actuator C moves this module along the YY axis (see Figure 3).

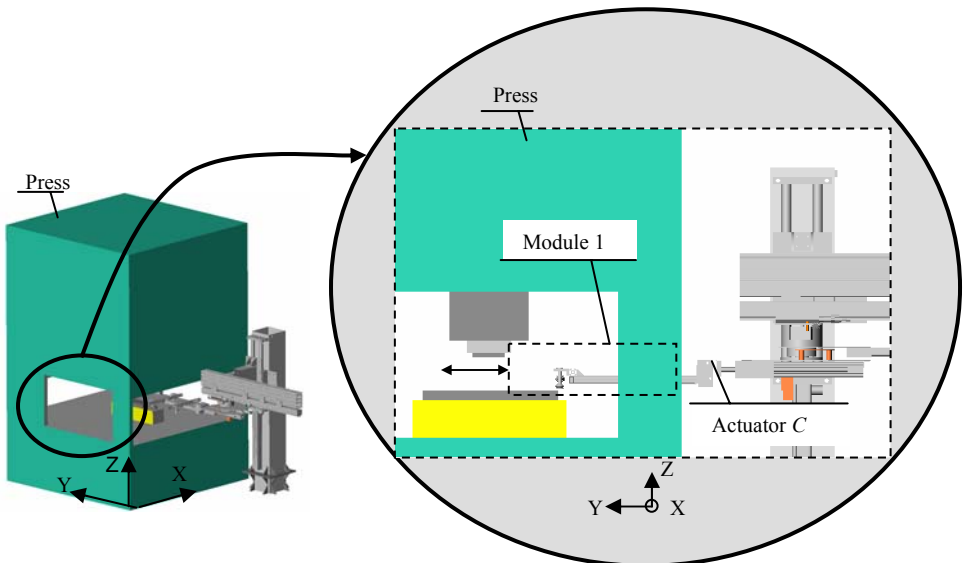


Fig. 3. Movements provided by Actuator C

Let Actuator C and Module 1 be named Module 2. Module 2 can be rotated along the ZZ axis by Actuator R (see Figure 4). Three discrete positions at 0° , 90° and 180° are currently available.

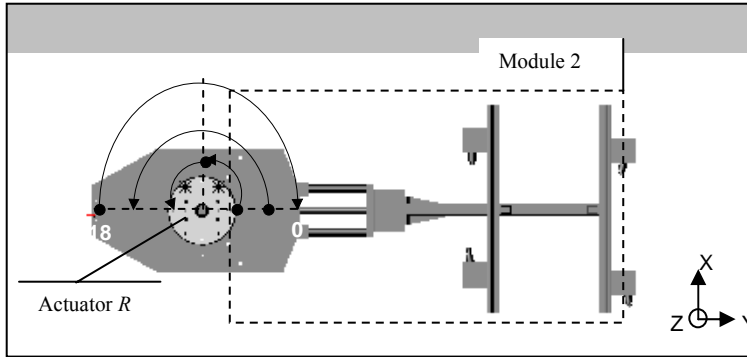


Fig. 4. Movements provided by Actuator R

Let Actuator R and Module 2 be named Module 3. This module can be moved along the YY axis by Actuator B (see Figure 5).

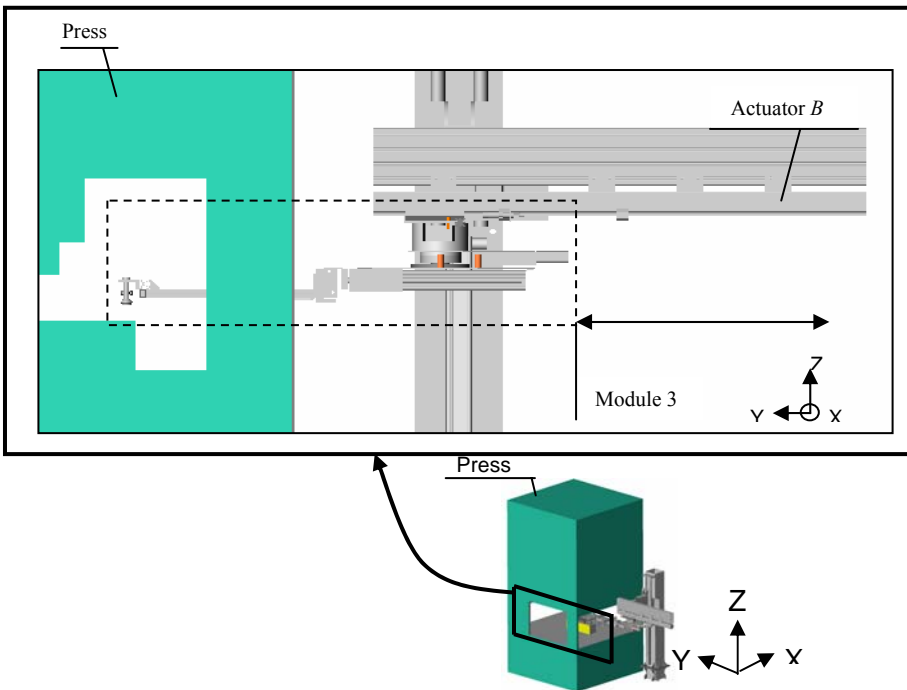


Fig. 5. Movements provided by Actuator B

Finally, let Actuator B and Module 3 be named Module 4. This module can be moved along the ZZ axis by Actuator A (see Figure 6).

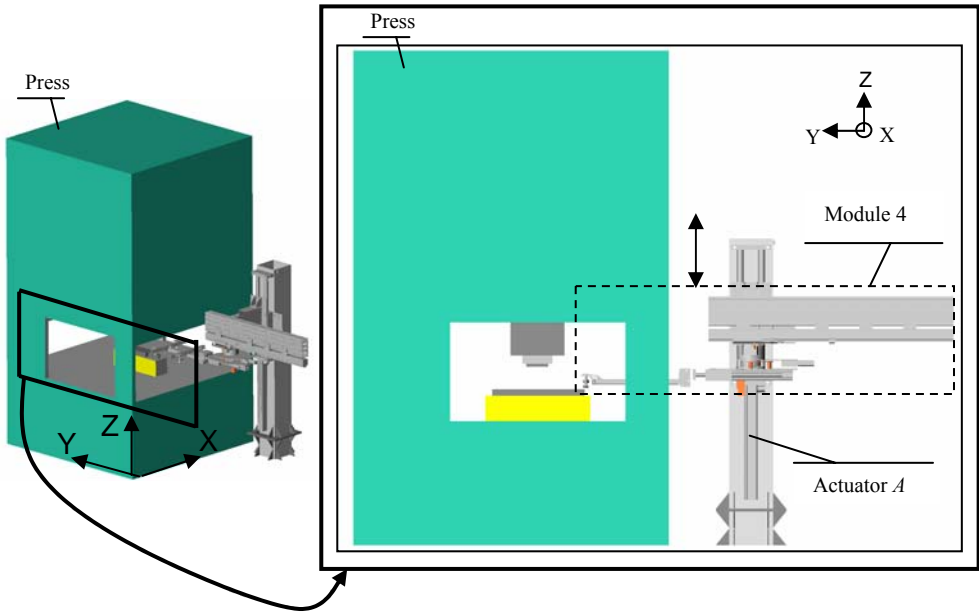


Fig. 6. Movements provided by Actuator A

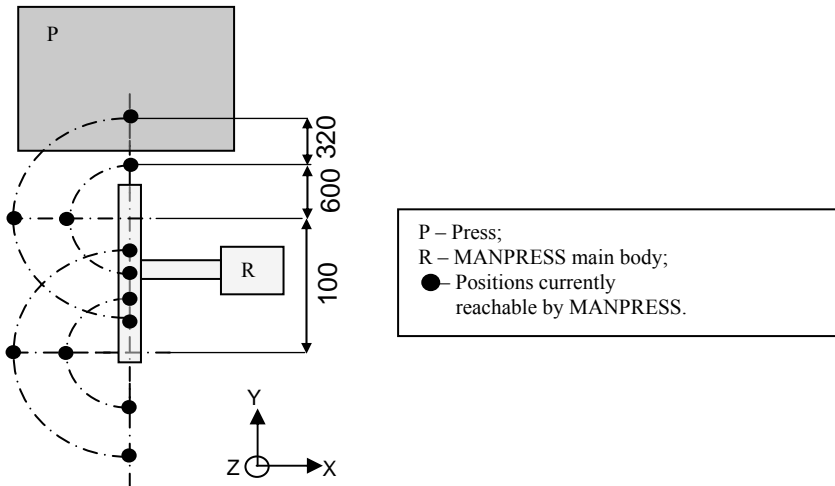


Fig. 7. Reachable areas and overall dimensions

All modules of MANPRESS can be easily added or removed to assure the requirements of each specific case. This solution allows not only the accommodation of different blank geometries and weights, but also an easy adaptation to different presses. Furthermore, small changes in the system arm allow its use for loading/unloading other machines than presses.

Loading and unloading devices must typically reach at least three distinct areas: one for loading raw parts, one for unloading the machined ones and one for loading the machine. MANPRESS provides a total of twelve reachable areas, identified by spots in Figure 7, if blank dimensions are smaller than a 250×250 mm square. Above these dimensions and up to a maximum of 500×500 mm square blank, a total of six areas are available. The maximum blank weight is 25 N and the overall dimensions of the system are also depicted in Figure 7.

3. Achieving optimal timing performance

3.1. The typical loading/unloading strategy

Four basic resources are required when a single robot feeds a single machine: a robot (R), a machine (M), an input buffer for raw parts (ZC), and an output buffer for the machined parts (ZD). This is sketched in Figure 8.

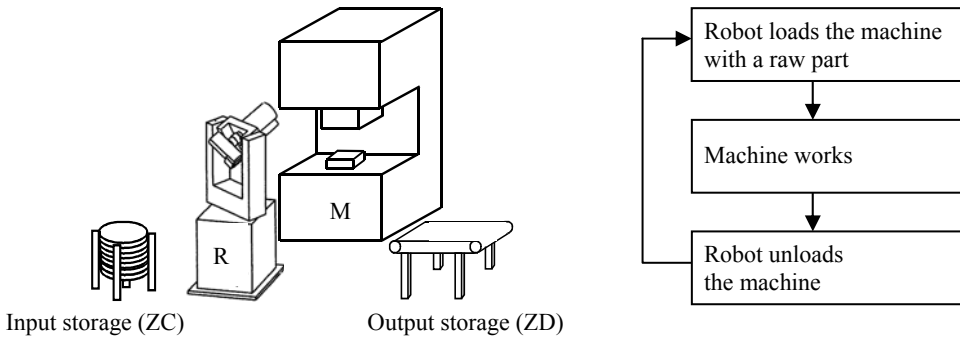


Fig. 8. RM strategy: elements and sequence of operations

In this scenario, each loading/unloading sequence requires that the robot loads the machine with a raw part, waits for the machine to finish its work and then unloads it, moving the machined part to the output buffer. Using this sequence — let's call it the RM sequence — the robot and the machine work in opposition: when the robot is working the machine is idle and *vice versa*. Thus, the cycle time for the RM sequence — i.e., the time elapsed between the production of two consecutive parts — is the sum of the time that the machine takes to machine a part and the time the robot takes to load and unload it.

Decreasing the cycle time is only possible by the usage of a faster robot or a faster machine. Both options are usually highly expensive, if possible at all. Thus, other loading/unloading strategies that can improve the timing performance of the system, while keeping its cost as low as possible, are worth devising.

3.2. Other strategies

An informal analysis of the RM strategy reveals that when the working time of the machine is long, the robot has to wait a lot. In this case, it seems reasonable that, instead of just waiting, the robot takes a new raw part from the input storage, ZC , and moves it near the machine, so that the loading time will be reduced in the next loading operation. However, this strategy implies the addition of a new element to the system: a buffer B_1 where a single raw part may be temporarily stored.

Using this new strategy — denoted RMB_1 (Robot, Machine, Buffer B_1) — a significant decrease in the cycle time may be achieved, specially when the machine requires a significant amount of time to process a part and one or more procedures need to be performed over a raw part before loading it into the machine — like lubrication, dimension control or other. Using the RM strategy the time spent in performing those previous tasks is included in the cycle time; yet, for the RMB_1 strategy, they are hopefully performed while the machine is processing the previous part. Figure 9 presents the sequence of actions for this strategy.

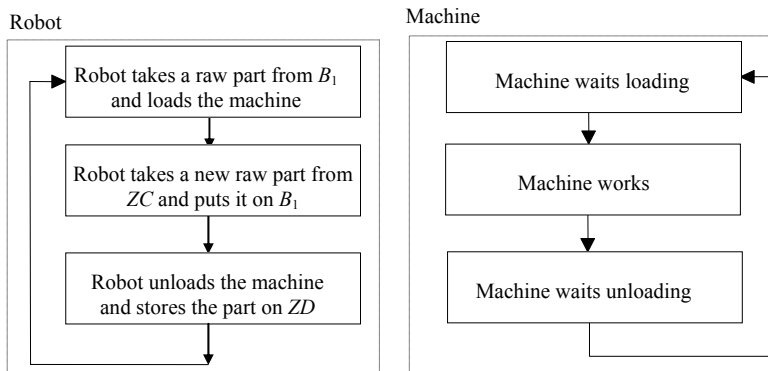


Fig. 9. RMB_1 strategy: sequence of operations

Other strategies can also improve systems' timing performance. For instance, when the time required for carrying a raw part from the input storage, ZC , to the machine is shorter than the time required for moving a machined part to the output storage, ZD , then this later task must be performed while the machine is working. In this case, the temporary buffer is used to store a machined part instead of a raw one — RMB_2 strategy. On the other hand, if the machine takes a considerable time to process a part, then the robot may move a raw part from ZC to B_1 , and then move the previously machined

part from B_2 to ZD , all while the machine is working. Two temporary unit buffers are required in this last case — the RMB^2 strategy — whose sequence of actions is shown in Figure 10.

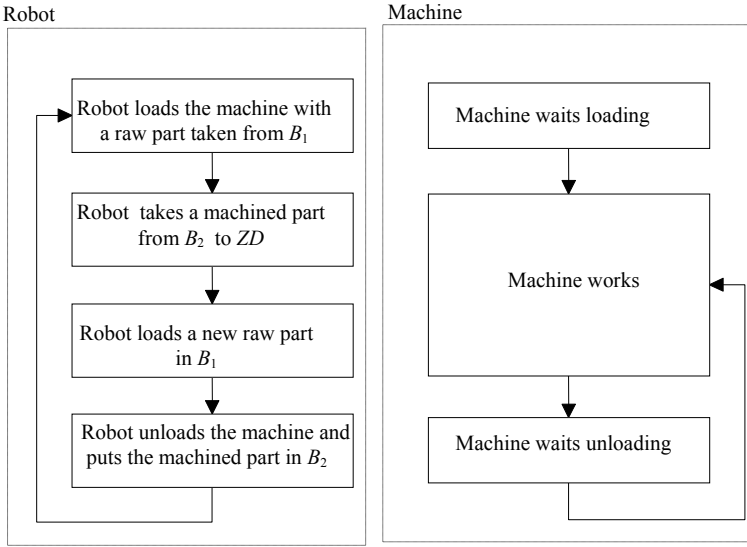


Fig. 10. RMB^2 strategy: sequence of operations

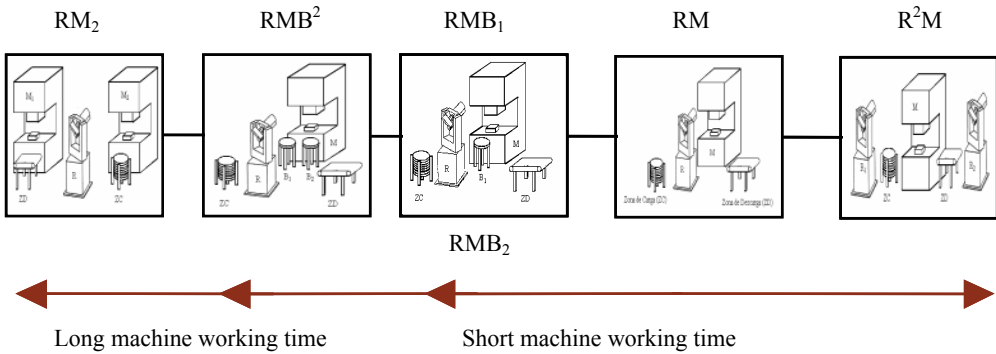


Fig. 11. The strategies proposed

Another possibility is to have a single robot feeding two machines — the RM^2 strategy. This is an interesting approach when the time a machine takes to process a part is relatively long. On the other hand, if the machine takes a very short time to process a part, having two robots, one for loading and the other for unloading, is a good strategy — the R^2M strategy. Figure 11 summarizes the drawn strategies.

3.3. Logical models

Formal logical models for the proposed strategies are required to prove systems' fundamental properties like liveness or reachability. By its turn, the devising of the strategy that leads to the best timing performance for a given pressing work requires the addition of time information to such models. Since manufacturing systems are Discrete Event Systems (DES), Automata theory [8] and Petri Nets [10] are the most used tools to model these systems. Petri nets are used in this work as they lead to more compact models.

To illustrate how a Petri net can model the above mentioned loading/unloading strategies, an informal graphical representation such as the one presented in Figure 12 is a good starting point — it represents the sequence of the robot movements for the RM strategy. The sequence begins with the robot loading the (idle) machine with a raw part (movement “1”). While the machine is working (“W”), the robot waits (“2”). When the machine work is completed, the robot unloads it and stores the machined part in the output storage (“3”). Then, the robot approaches the input storage “4”, grabs a new raw part and the process restarts.

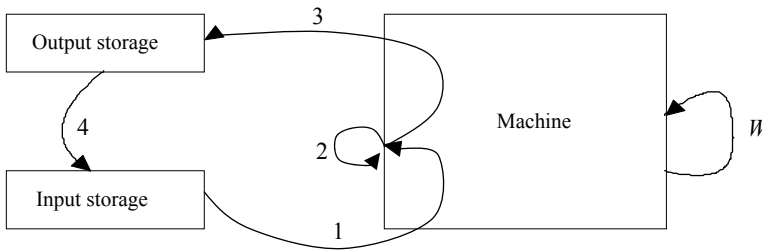


Fig. 12. Robot movements in RM strategy

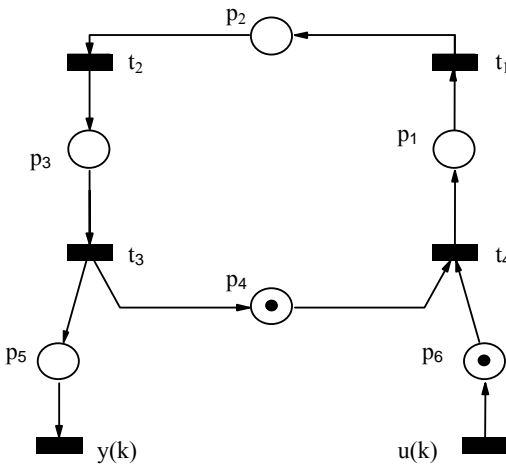
Petri nets can produce much more formal models. In order to explain how they are developed, some basic definitions and notations of Petri nets are briefly introduced. For complete background and details see, for example, [10].

Definition 1: A Petri net is a five-tuple $Z = (P, T, I, O, M_0)$, where:

- P is a set of places, $P = \{p_1, p_2, p_3, p_4, \dots\}$; places are graphically represented by circles.
- T is a set of transitions, $T = \{t_1, t_2, t_3, t_4, \dots\}$, with $P \cup T \neq \emptyset$ and $P \cap T = \emptyset$; transitions are represented by rectangular bars.
- $I = P \times T \rightarrow \{0, 1\}$ is the pre-incidence function, specifying directed arcs from places to transitions.
- $O = P \times T \rightarrow \{0, 1\}$ is the post-incidence function, specifying arcs from transitions to places; $M: P \rightarrow \mathbb{N}$ is a vector $M = (m_1, m_2, m_3, m_4, \dots) = \{m(p_1), m(p_2), \dots\}$.

$m(p_3), m(p_4), \dots$ whose i^{th} component is the marking of the place p_i at a given time instant. The evolution of the marking of the net is denoted by the index of M : $M_0 = \{m_1, m_2, m_3, \dots\}$ is a vector representing the initial marking (at time instant 0), $M_1 = \{m_1, m_2, m_3, \dots\}$ represents the marking of Z after the first firing of a transition. The marking of a place is graphically represented by the number of tokens (black dots) it contains.

- The set of input and output transitions of a place p are the *pre-* and *post-*sets of p and are notated, respectively, by $\bullet p$ and $p\bullet$; the set of input and output places of a transition t are the *pre-* and *post-*sets of t and are notated, respectively, by $\bullet t$ and $t\bullet$;
- A transition t is enabled and can be fired *iff* $m_p > 0$ when $I(p,t) = 1, \forall p \in \bullet t$; this means that t is enabled if all of its pre-places contain at least one token.
- If a transition is enabled, it can be fired. Firing a transition t consists of removing a token from each $p \in \bullet t$ and adding a token to each $p \in t\bullet$.



Place	Description
p_1	Robot loads the machine with a raw part
p_2	Robot waits while machine is working
p_3	Robot unloads machine and stores machined part in <i>ZD</i>
p_4	Robot approaches <i>ZC</i> and grabs a raw part
p_5	Machined part exits the system
p_6	Raw part enters the system

Fig. 13. Petri net model for the RM strategy

In the present case, places denote system states and associated actions; transitions represent conditions leading to state transitions. Using a Petri net, the informal model depicted in Figure 12 reverts to the one presented in Figure 13.

This net has the set of places $P = \{p_1, p_2, p_3, p_4, p_5, p_6\}$ and the set of transitions $T = \{t_1, t_2, t_3, t_4, x(k), y(k)\}$, where $u(k)$ – source transition – and $y(k)$ – sink transition – denote blanks entering and leaving the system, respectively. The initial marking $M_0 = \{0, 0, 0, 1, 0, 1\}$ represents the situation where the robot is ready to load the machine – p_4 is marked – and a raw part is available – p_6 is also marked. Since $\bullet t_4 = \{p_4, p_6\}$, transition t_4 is enabled at time 0 and will fire, giving rise to the new marking $M_1 = \{1, 0, 0, 0, 0, 0\}$, which denotes that the robot is loading the machine. This process continues, with transitions t_1, t_2 and t_3 firing in this order, so the initial marking is reached again.

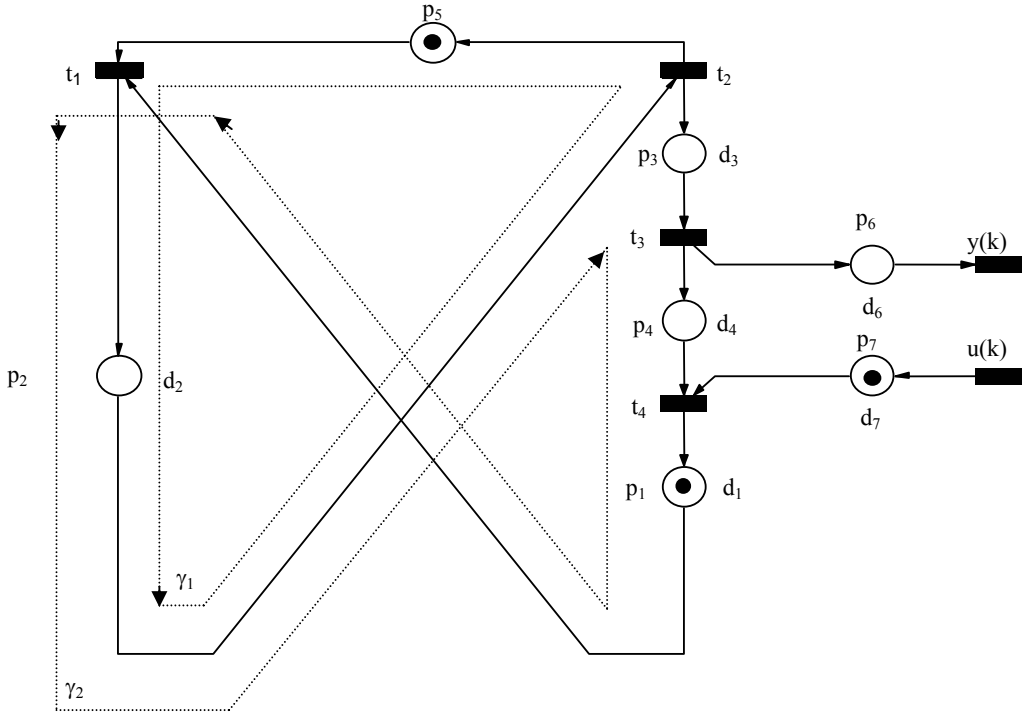


Fig. 14. Petri net model for the RMB² strategy

Based on a similar reasoning, particular models for the strategies proposed in 3.2 were achieved. Figure 14* illustrates and describes the logic model for the most complex strategy concerning a single robot and a single machine: the RMB² strategy. This net has derived from more complex Petri net that was simplified according to the well-known Petri nets reduction rules described in current literature. As a result, each place in Figure 14 describes an action or a *sequence* of actions. For instance, p_1 represents the following set of actions: the robot loads the input buffer B_1 with a raw part taken from the input storage and approaches the machine. Place p_5 represents the machine work. While the machine is working, actions represented by places p_3 and p_4 are executed: the robot stores the previous machined part in the output storage and approaches the input storage.

When the machine work is concluded, the set of actions represented by p_2 will be executed: the robot unloads the machine, stores the machined part in the output buffer B_2 and loads a new raw part into the machine. The cycle then restarts.

After developing formal models for the strategies, the next step is to use Petri nets formalisms to prove a set of properties that must be guaranteed in manufacturing systems — safeness, liveness and reversibility [2]. Such properties are trivially proved

* Please ignore for the moment the notations d_i , $i = 1 \dots 7$ and γ_i , $i = 1, 2$. They will be explained in the next subsection.

using coverability graphs as illustrated in [7]. It is worth noting that transient paths related to the first and final cycles were not considered in Figure 14. However, as also shown in [7], those simplifications eliminate some unnecessary complexity, since they do not have any impact on the major logic properties of the model.

Table. Description of the places of Figure 14

Place	Description
p_1	Movements "1": robot loads B_1 with a raw part taken from ZC and approaches the machine
p_2	Movements "2": the robot unloads the machine, stores the machined part in B_2 and loads a new raw part, taken from B_1 , into the machine
p_3	Movement "3": robot stores grabs previous machined part from B_2 and stores it in ZD
p_4	Movement "4": robot approaches input storage
p_5	Machine working
p_6	Machined part exists in the system
p_7	Raw part enters the system

3.4. Timed models

Performance evaluation requires timed models. Timed Petri nets [13] can be easily used for this purpose, as it suffices to add timing information to the logical models already defined.

Definition 2: A timed Petri net is a six-tuple $Z = (P, T, I, O, M_0, D)$ where P, T, I, O and M_0 are defined according to Definition 1 and D is a set $D = \{d_1, d_2, d_3, d_4, \dots\}$ such that each place p_i is timed by an amount d_i . The time d_i starts to count when a token appears in p_i , meaning that when a token reaches a place p_i it remains unavailable until d_i runs out.

Timed Petri nets are thus important in modelling those discrete event systems whose actions (associated with places) require a given amount of time to be performed. As an example, Figure 15 presents the timed Petri net model associated with the RM strategy. It can be seen that a time d_i is allocated to each place p_i , representing the time required to perform the action given by p_i .

Timed Petri nets are not trivial to analyze in general. However, in the present case, the performance analysis is easy to perform, since the Petri net models achieved are event graphs — each place has exactly one input and one output transition. The following definitions apply to event graphs ([2], [3]):

Definition 3: In an event graph, a sequence of places and transitions $\langle p_1, t_1, p_2, t_2, \dots, t_{n-1}, p_n \rangle$ is called a directed path from p_1 to p_n if $t_i \in p_i^\bullet$ and $t_i \in {}^\bullet p_{i+1}$ for $1 \leq i \leq n-1$.

Example 1: in the net of Figure 14, $\langle p_3, t_3, p_4 \rangle$ is a directed path from p_3 to p_4 ; in the net of Figure 15, $\langle p_1, t_1, p_2, t_2, p_3 \rangle$ is a directed path from p_1 to p_3 .

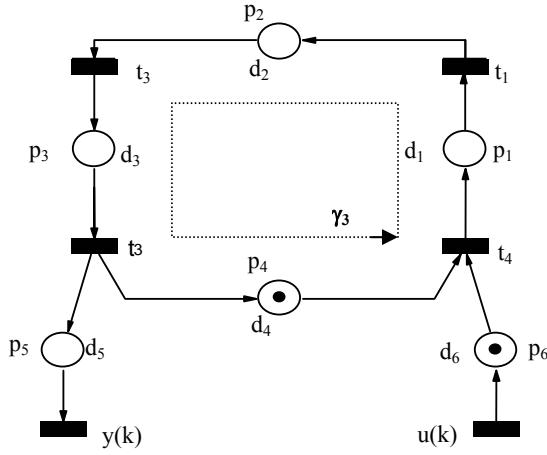


Fig. 15. Timed Petri model for RM strategy

Definition 4: In an event graph, a directed path $\langle p_1, t_1, p_2, t_2, \dots, t_{n-1}, p_n \rangle$ in which $p_1 = p_n$, or an oriented path $\langle t_1, p_2, t_2, \dots, p_{n-1}, t_n \rangle$ in which $t_1 = t_n$, without repetition of places or transitions is called an elementary or directed circuit γ .

Example 2: in the net of Figure 14, the directed path $\langle p_2, t_2, p_5, t_1, p_2 \rangle$ is a directed circuit named γ_1 ; in the net of Figure 15, the directed path $\langle p_1, t_1, p_2, t_2, p_3, t_3, p_4, t_4, p_1 \rangle$ is a directed circuit named γ_3 .

The procedure to determine the cycle time for each strategy requires the introduction of following theorems. Let Γ be the set of directed circuits of an event graph Z :

Theorem 1 [2]: For a timed event graph, the minimum average cycle time is:

$$TC = \max_{\gamma \in \Gamma} \left\{ \frac{D(\gamma)}{N(\gamma)} \right\}, \quad (1)$$

where $D(\gamma) = \sum_{p_i \in \gamma} d_i$ is the sum of times of places in directed circuit γ , and $N(\gamma)$ the

number of tokens in the places in directed circuit γ .

Theorem 2 [11]: The total number of tokens in any elementary circuit is *invariant* by transition firings.

The procedure to determine the cycle time for each strategy applies these theorems and involves four steps:

1. Determine the directed circuits on the graphs of each strategy.

Example 3: Figure 14 has two directed circuits γ_1 and γ_2 and Figure 15 one directed circuit γ_3 .

2. For each directed circuit i , determine its cycle time $D(\gamma_i)$.

Example 4: In Figure 14, $D(\gamma_1) = d_2 + d_5$, $D(\gamma_2) = d_1 + d_2 + d_3 + d_4$; in Figure 15, $D(\gamma_3) = d_1 + d_2 + d_3 + d_4$.

3. For each directed circuit, determine its token count $N(\gamma_i)$, which is, by Theorem 2, the token count for the initial marking.

Example 5: In Figure 14, $N(\gamma_1) = 1$ and $N(\gamma_2) = 1$; in Figure 15, $N(\gamma_3) = 1$.

4. Determine the cycle time for each strategy using Theorem 1.

Example 6: In Figure 14, $TC = \max(D(\gamma_1), D(\gamma_2))$; in Figure 15, $TC = D(\gamma_3)$.

Applications of this procedure can be found in [12] and [2]. It is worth mentioning that transient paths related to the first and last cycles are not included in the performance analyses described above. However, the error introduced by this simplification is minimum, as loading/unloading a machine is usually performed in the context of a batch involving the processing of hundreds or thousands of parts in a row.

3.5. Application example

The procedures referred in the last section were applied to a realistic simulation of the MANPRESS robot feeding a mechanical press [7]. Figure 16 presents the cycle time for different loading/unloading strategies as a function of the time that the press takes to process a part — press working time. Naturally that the RM^2 strategy provides an output of two machined parts *per* cycle and therefore comparisons must be made against half of its cycle time — the dotted line in Figure 16.

The strategies that provide the lower cycle times are RM^2 and R^2M . However, both require additional investments — an extra machine or an extra robot — that may or may not be rewarding.

Comparing the RM , RMB_1 , RMB_2 and RMB^2 strategies, i.e., those that include a single robot and a single machine, one can find that the RM strategy is the best one for press working times shorter than nearly 3 s. If the press working time briefly exceeds this time, then the RMB_2 strategy leads to a minimum cycle time. If the machine working time exceeds 4 s, then the RMB^2 is the best strategy.

The same results are shown in a different way in Figure 17. From there it is possible to note that, for a press working time of about 4.5 s, the RMB^2 strategy can improve the cycle time by about 15% compared to the typical RM . From here, it is possible to conclude that loading/unloading strategies play a major role in the timing performance of flexible automation systems. In the presented example, a good strategy was able to reduce the cycle time by about 15% compared to a traditional one.

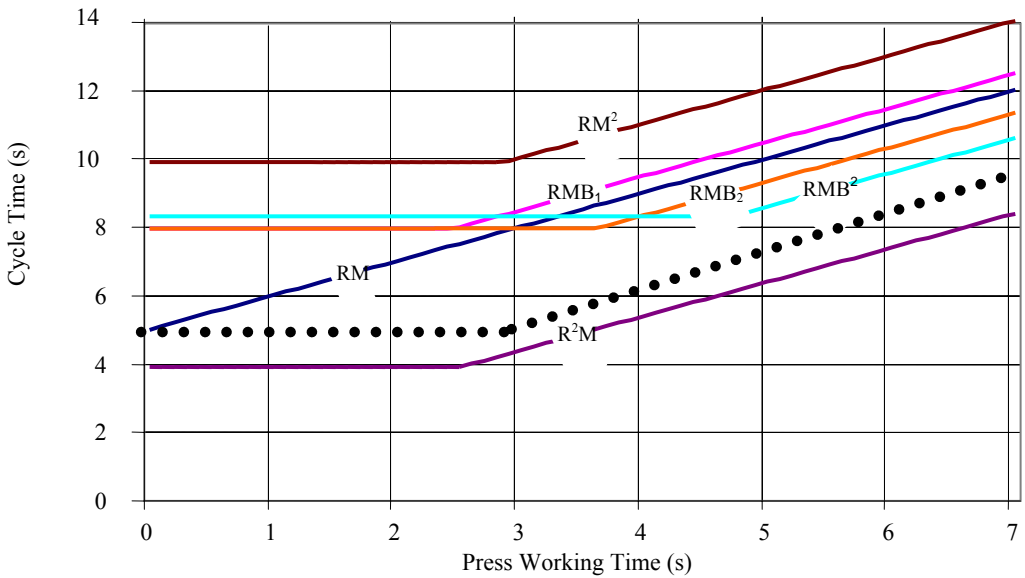


Fig. 16. Cycle time vs. press working time

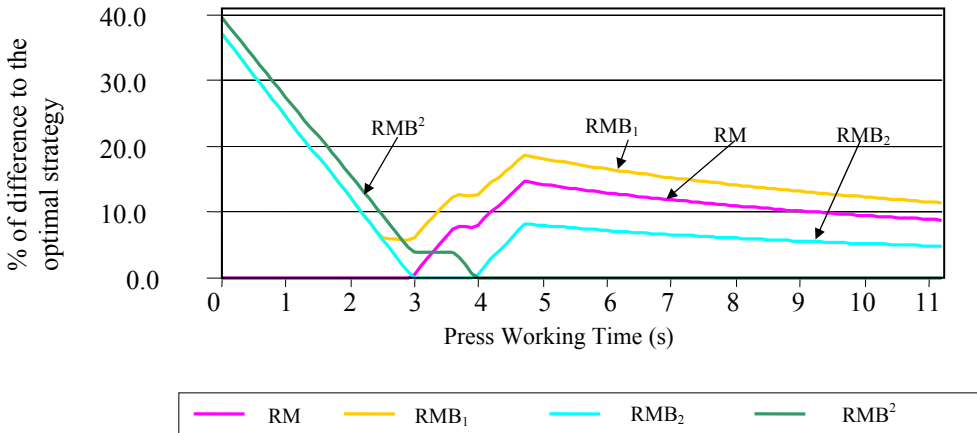


Fig. 17. Difference, in percentage, between the cycle time of RM, RMB₁, RMB₂ and RMB² strategies and the cycle time of the optimal strategy

4. MANPRESS controllers

The hierarchical structure of the MANPRESS controllers appears very naturally: a supervisor is entrusted with decision on the best loading/unloading strategy for

a given pressing work — according to the time that the press takes to process a part — while a direct controller interacts with the actuators and sensors of the robot implementing the selected strategy (see Figure 18).

The behavioural aspects of both direct and supervisory controllers were specified using GRAFCET [9]. Not only because GRAFCET is easy to implement on a real or soft PLC [7] but also because it is very simple and intuitive to translate a Petri net to a Grafcet.

In this case, direct control was implemented on a PC-based soft-PLC; more precisely on a modern graphical programming language simulating sequences of steps drawn on a GRAFCET based style (Figure 19) [14]. This is because the graphical front-end provided by a modern PC is a much more interesting human-machine interface than those provided by programmable terminals attached to standard PLCs. Standard and low-cost electromechanical devices were used as the interface between the discrete I/O computer boards to the MANPRESS actuators and sensors.

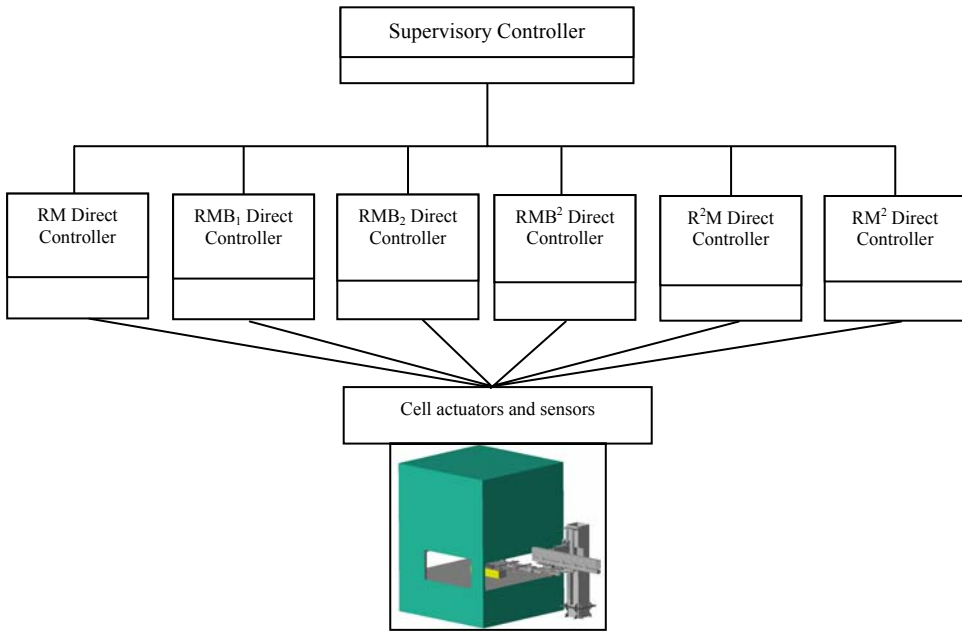


Fig. 18. The structure of the cell controllers

The specification of the supervisory control is concluded, but its final design is still in progress. It has been simulated using a SCADA software package communicating with real PLCs controlling a PC-based simulation of several manufacturing cells. The results completely met the expectations. In the final stage, the SCADA software will run on a PC, communicating with the direct controller via a standard local network. The benefits of using a PC-based PLC as a direct controller are evident in this field:

the proliferation of standards and hardware and software resources for connecting two or more PC. However, if a standard PLC were used, no major difficulties would arise, as modern SCADA packages include communication drives for the most popular PLCs.



Fig. 19. Direct control of MANPRESS — image of a PC screen

It is worth mentioning that direct and supervisory controllers do not impose special requirements to press controller. Therefore, standard press controllers can be easily integrated in the presented solution. Moreover, the usage of a SCADA package allows data acquisition and integration to be easily performed, providing thus a major contribution to production management.

5. Conclusions and future work

This paper has presented the mechanical and control features of a low-cost loading/unloading device mainly devoted to press feeding: the MANPRESS robot. The main features of this robot are flexibility and optimal performance in press feeding. A set of strategies for loading and unloading machines was formally proposed and analysed. From there, it was possible to show that loading/unloading strategies play a major role in the timing performance of flexible automation systems. In the presented example, a good strategy was able to reduce the cycle time by about 15% compared to a traditional strategy. However, such a benefit can only be attained with the help of a controller that can impose to the MANPRESS robot the proper loading/unloading strategy. The design and implementation of such a controller, that includes a direct controller and a supervisory controller, was discussed in the final part of the paper, showing they are both simple and relatively inexpensive. As such, the MANPRESS robot emerges as a serious contribution to optimal loading/unloading performance in automatic press feeding.

Acknowledgements

This work was developed at INEGI, being partially funded by the Portuguese Foundation for Science and Technology (FCT) to whom the authors are grateful.

References

- [1] Falcão Carneiro J., Barata da Rocha A.: *Manpress: Alimentador Automático de Prensas Mecânicas e Hidráulicas* (in Portuguese), PRAXIS Activities Report, Project PRAXIS /3/3.1/CEG/2613/95, 2000.
- [2] Park E., Tilbury D., Khargonekar P.: *Modular Logic Controllers for Machining Systems: Formal Representation and Performance Analysis Using Petri Nets*, IEEE Trans. on Robotics and Automation, 1999, Vol. 15, No. 6.
- [3] Hillion H., Proth J.-M.: *Performance Evaluation of Job-Shop Syst. Using Timed Event-Graphs*, IEEE Trans. On Automatic Control, 1989, Vol. 34, No. 1, pp. 3–9.
- [4] Suri R., Ramakrishna D.: *Performance Analysis of Flexible Manufacturing Systems with a Single Discrete Material-Handling Device*, The International Journal of Flexible Manufacturing Syst., 1997, 9, pp. 223–249.
- [5] Gaujal B., Jafari M., Baykal-Gursoy M., Alpan G.: *Allocation Sequences of Two Processes Sharing a Resource*, IEEE Trans. on Robotics and Automation, 1995, Vol. 11, No. 11, pp. 748–753.
- [6] Alpan G., Jafari M.: *Dynamic Analysis of Timed Petri Nets: A Case of Two Processes and a Shared Resource*, IEEE Trans. on Robotics and Automation, 1997, Vol. 13, No. 3.
- [7] Falcão Carneiro J.: *Desenvolvimento de Controlador para Célula Robotizada* (in Portuguese), Master Thesis, 2001, FEUP, Portugal.
- [8] Ramadge P., Wonham W.: *The Control of Discrete Event Systems*, Proceedings of the IEEE, 1989, Vol. 77, No. 1.
- [9] David R.: *Grafcet: A Powerful Tool for Specification of Logic Controllers*, IEEE Trans. on Control Syst. Technology, 1995, Vol. 3, No. 3.
- [10] Cassandras C., Lafortune S.: *Introduction to Discrete Event Systems*, Kluwer Academic Publishers, 1999.
- [11] Commoner A., Holt A., Even S., Pnueli S.: *Marked directed graphs*, J. Comput. Syst. Sci., 1971, Vol. 5, No. 5, pp. 511–523.
- [12] Di Febbraro A., Minciardi R., Sacone S.: *Deterministic Timed Event Graphs for Performance Optimization of Cyclic Manufacturing Processes*, IEEE Trans. on Robotics and Automation, 1997, Vol. 13, No. 2, pp. 169–180.
- [13] Wang J.: *Timed Petri Nets*, Kluwer Academic Publishers, 1998.
- [14] National Instruments LabView Users Manual, July 2000 edition.

Wkład do optymalnego automatycznego podawania i odbierania wyrobów z pras: robot MANPRESS

Przedstawiono robota, nazwanego MANPRESS, który opracowano w Centrum Transferu Technologii INEGI w Porto. Robot charakteryzuje się prostotą i niskim kosztem, jest przeznaczony głównie do współpracy z prasami w operacjach podawania i odbierania półproduktów

i produktów końcowych. Dwie jego główne cechy to duża elastyczność w przystosowaniu się do różnych maszyn i wyrobów oraz optymalne osiągnięcia w operacjach podawania i odbierania produktów zarówno do jednej prasy, jak i do wielu pras. Pierwszą cechą osiągnięto dzięki zastosowaniu modułowego i samokontrolującego się systemu. Drugą zaś jest wynikiem wynalezienia i zastosowania nowoczesnego algorytmu sterującego opartego na teorii systemów zjawisk dyskretnych. Strategia operacji podawania i odbierania wyrobów w prasach automatycznych i wynikające z tego zwiększenie efektywności są często pomijane w bieżącej literaturze naukowej. Głównym celem pracy było wypełnienie tej luki. Przewieziono rozwój teorii oraz wykazano, że zwiększenie efektywności podawania i odbierania produktów o 15% można łatwo osiągnąć, stosując właściwą strategię tych operacji. W praktyce jest to możliwe jedynie wtedy, gdy zostanie zastosowane urządzenie o prostym sterowaniu i dużej elastyczności operacji podawania i odbierania wyrobów, jakim jest robot MANPRESS. Opisano też główne mechaniczne i sterujące właściwości tego robota.

State analysis of time-varying linear systems via Walsh-wavelet packets

WOJCIECH GLABISZ

Wrocław University of Technology, Wybrzeże Wyspiańskiego 27, 50-370 Wrocław

Algorithms using wavelet-packet bases for solving initial-value problems described by systems of linear differential equations with constant or variable coefficients have been demonstrated. Algorithms which use expansions of the derivative of state variables and expansions of the state variables in any wavelet-packet basis were described and compared. The results of the analyses were compared with the results yielded by classical methods of solving initial-value problems in their differential formulation and with exact results. The convergence, computational accuracy and efficiency of the algorithms were tested. Special attention was devoted to different possible forms of operational matrices, which generalize the latter's conventional formulations and significantly affect computational accuracy.

Keywords: *state analysis, wavelet analysis, Walsh packet basis*

1. Introduction

Functions have been represented in orthogonal function bases for a long time, and not only in mathematics. Since the 1970s this way of representing functions has been widely used to solve differential equations describing dynamics of mechanical systems, control and identification problems. Finlayson [1] and Villadsen and Michelson [2] solved differential equations, using orthogonal polynomial approximations. Orthogonal Walsh functions were applied by Corrington [3] and Chen and Hsiao [4], who were the first to define the notion of an operational integration matrix for this type of functions. Operational matrices, as essential components of algorithms analyzing differential equations, have been formulated for different basis functions. Chen, Tsay and Wu [5], among others, defined an operational matrix for block pulse functions, Hwang and Shih [6] and King and Paraskevopoulos [7] did it for Laguerre functions, Chang and Wang [8] for Legendre polynomials, Paraskevopoulos [9] for Chebyshev functions and Paraskevopoulos, Sparcis and Monroursos [10] for Fourier series.

Recently, wavelet bases have been increasingly used in descriptions of different classes of functions [11], [12]. Owing to their properties, wavelet bases have proved to be a convenient and universal tool for the analysis of different technical problems, including the ones whose description reduces itself to differential equations. Chen and Hsiao [13] were the first to present an operational integration matrix based on Haar wavelets and they applied it to the analysis of lumped and distributed parameters of dynamic systems. State analysis of time delayed systems via Haar wavelets was pro-

posed by Hsiao [14]. Hsiao and Wang [15] applied the Haar operational matrix to optimization in linear control problems. On the basis of the Haar operational matrix Chen and Hsiao [16] worked out a complete simple procedure for optimizing linear dynamic systems. Recently, Hsiao and Wang [17, 18] applied Haar wavelets to the state analysis and parameter estimation of bilinear systems and to the analysis of nonlinear stiff systems.

This paper's goals are:

- to formulate, using the Walsh-wavelet packet bases, algorithms for analyzing linear differential equations of initial-value problems with constant and variable coefficients,
- to present the forms of the so-called modified operational matrices and to investigate their effect on computational accuracy.

The application of Walsh-wavelet packets represents a generalization of the conventional Haar and Walsh bases which are special cases of the wavelet packet bases considered here. The form of operational matrices is modified by assuming different characteristic points for the intervals of piecewise constant packet bases and in this way a whole class of matrices, whose special cases are Haar and Walsh operational matrices, is generated.

In chapter 2 of this paper, basic terms relating to wavelet packet analysis are explained. In chapter 3, algorithms (which can be used with any Walsh-wavelet packet basis) for analyzing linear differential equations with constant and variable coefficients are presented. In chapter 4, the so-called modified operational matrices are defined. In chapter 5, exemplary analyses are provided and their results are discussed. In chapter 6, general conclusions emerging from the application of packet bases and modified operational matrices are presented.

2. Walsh-wavelet packets

A wavelet transformation consists in the representation of function $f(t) \in L^2$ (a square-integrable function) in orthogonal subspaces $\{W_j\}$ with the bases in the form of wavelets $\{\psi_j(t)\}$ and in subspace $\{V_j\}$ with a basis of scaling functions $\{\phi_j(t)\}$ [11], [12]. The successive wavelet decomposition of space V_J into a sum of orthogonal subspaces can be represented as follows

$$V_J = W_{J-1} \oplus V_{J-1} = W_{J-1} \oplus W_{J-2} \oplus V_{J-2} = \dots = \bigoplus_{j=1}^{J-1} W_j \oplus V_0. \quad (1)$$

From multiresolution it is known that basis functions $\{\phi_{1k}(t)\}$ of V_1 , $\{\phi(t-k)\}$ and $\{\psi(t-k)\}$ constitute an orthonormal basis for V_0 and W_0 , respectively, and $V_1 = W_0 \oplus V_0$, where

$$\phi(t) = \sqrt{2} \sum_k h_k \phi(2t-k),$$

$$\psi(t) = \sqrt{2} \sum_k g_k \phi(2t - k). \tag{2}$$

Filter factors are denoted by h_k and g_k for a low-pass filter and a high-pass filter, respectively. It should be noted that only subspaces V_j are subject to wavelet decomposition in the subsequent stages of the analysis.

The wavelet analysis algorithm can also be used to decompose subspace W , which leads to the so-called wavelet packet analysis.

If by analogy with (2) we define

$$\begin{aligned} w_2(t) &= \sqrt{2} \sum_k h_k \psi(2t - k), \\ w_3(t) &= \sqrt{2} \sum_k g_k \psi(2t - k), \end{aligned} \tag{3}$$

then $\{w_2(t - k)\}$ and $\{w_3(t - k)\}$ constitute an orthonormal basis of functions of two subspaces whose direct sum is subspace W_1 .

Generally, for $n = 0, 1, \dots$ one can define the following sequence of functions

$$\begin{aligned} w_{2n}(t) &= \sqrt{2} \sum_k h_k w_n(2t - k), \\ w_{2n+1}(t) &= \sqrt{2} \sum_k g_k w_n(2t - k) \end{aligned} \tag{4}$$

which form a sequence of basis functions of space V_J . Various combinations of the functions and their dilatations and translations can give rise to a whole collection of different orthonormal bases $\{w_n(t)\}$ for the function space. We call this collection a ‘‘library of wavelet packet bases’’ and a function having the form: $w_{n,j,k} = 2^{j/2} \cdot w_n(2^j t - k)$ is called a wavelet packet. If we refer to a space with basis $\{w_{n,j,k}(t)\}$ as $w_{n,j}$, the diagram shown in Figure 1 may serve as an illustration of the decomposition of space $w_{0,3}$ (V_3) by means of a wavelet packet.

In this paper, wavelet packets generated from the Haar filter for which $h_0 = h_1 = g_0 = -g_1 = 1/\sqrt{2}$ are used.

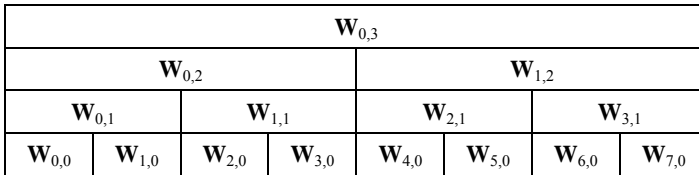


Fig. 1. The decomposition diagram of the space $w_{0,3}$ (V_3) using wavelet packets

Obviously, different wavelet packet bases can be used to describe a space. Four possible combinations of basis functions for decomposition of space V_3 are shown in Figure 2. Their locations were marked by filling in the areas representing subspaces V_3 with black.

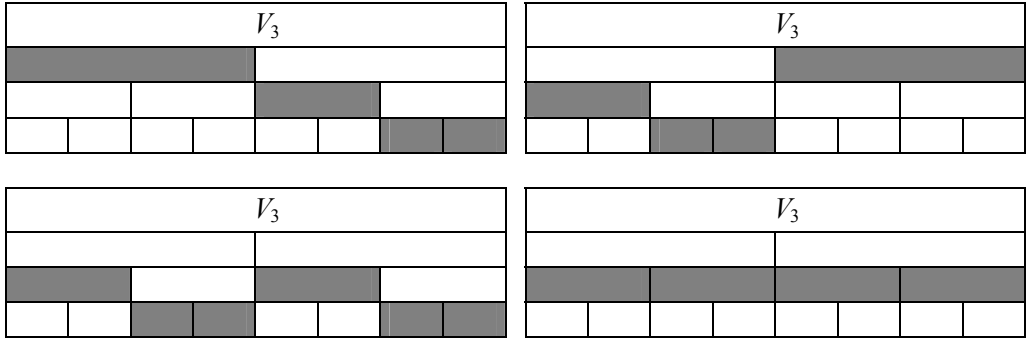


Fig. 2. Examples of wavelet-packet basis locations of the space V_3

The locations of the classical wavelet analysis basis and the Walsh basis functions (being the product of Rademacher functions [4]) on the decomposition diagram of space V_3 are shown in Figure 3.



Fig. 3. Diagram of the wavelet basis (left) and Walsh basis (right) locations

The algorithms presented in the next chapter work with any Walsh-wavelet packet basis.

3. State analysis of linear systems

Let us consider the following system of n ordinary differential equations

$$\dot{\mathbf{x}}(t) = \mathbf{A}\mathbf{x}(t) + \mathbf{B}\mathbf{u}(t), \quad \mathbf{x}(0) = \mathbf{x}_0, \tag{5}$$

where $\mathbf{x}(t) \in \mathbb{R}^n$ is a vector of state variables, vector $\mathbf{u}(t) \in \mathbb{R}^r$ represents a prescribed arbitrary excitation, matrices \mathbf{A} and \mathbf{B} are known $n \times n$ and $n \times r$ coefficient matrices and t is an independent variable which is further referred to as time. A dot denotes a derivative of vector \mathbf{x} with respect to time.

First we shall consider a case in which the system of equations (5) has constant coefficient matrices \mathbf{A} and \mathbf{B} and then a case in which the matrices' coefficients can be any functions of time t .

Let us assume that we have an arbitrary Walsh-wavelet packet basis vector represented in a discrete form by matrix $\mathbf{H}(t)$ with size $m \times m$ where parameter $m = 2^J$ is further referred to as a degree of approximation. Matrix $\mathbf{H}(t)$ can be represented by the Haar basis, the Walsh basis or any wavelet packet basis. Since the bases are defined for $t \in [0,1)$, analysis time t ($0 \leq t \leq t_f$) should be normalized by introducing variable τ so that $t = t_f \tau$. As a result, system (5) assumes this form

$$\dot{\mathbf{x}}(\tau) = t_f [\mathbf{A}\mathbf{x}(\tau) + \mathbf{B}\mathbf{u}(\tau)], \quad \mathbf{x}(0) = \mathbf{x}_0, \quad (6)$$

where a dot denotes differentiation with respect to τ .

Known excitation function $\mathbf{u}(t)$ can be represented in a function basis $\mathbf{H}(\tau)$ as

$$\mathbf{u}(\tau) = \mathbf{C}\mathbf{H}(\tau), \quad (7)$$

where \mathbf{C} is a matrix of expansion coefficients. At this moment $\mathbf{u}(\tau)$ is a discrete representation of excitation functions which takes a $n \times m$ matrix form.

For constant matrices \mathbf{A} and \mathbf{B} we shall consider two cases in which $\dot{\mathbf{x}}(\tau)$ or $\mathbf{x}(\tau)$ is represented in basis $\mathbf{H}(\tau)$.

If $\dot{\mathbf{x}}(\tau)$ is expanded in basis $\mathbf{H}(\tau)$

$$\dot{\mathbf{x}}(\tau) = \mathbf{F}\mathbf{H}(\tau), \quad (8)$$

then through integration (8) we arrive at

$$\mathbf{x}(\tau) = \int_0^\tau \dot{\mathbf{x}}(\tau) d\tau + \mathbf{x}_0 = \mathbf{F} \int_0^\tau \mathbf{H}(\tau) d\tau + \mathbf{x}_0 = \mathbf{F}\mathbf{P}\mathbf{H}(\tau) + \mathbf{x}_0, \quad (9)$$

where \mathbf{F} denotes the sought $n \times m$ matrix and $\int_0^\tau \mathbf{H}(\tau) d\tau \cong \mathbf{P}\mathbf{H}(\tau)$. Now $\mathbf{x}(\tau)$ is a discrete representation of state variables which takes a $n \times m$ matrix form. \mathbf{P} stands for the so-called operational matrix [4], [13]–[16] which is a matrix of coefficients of expansion, in basis $\mathbf{H}(\tau)$, of the integral from $\mathbf{H}(\tau)$. The approximate equality sign in definition \mathbf{P} is used to highlight the fact that the integral from $\mathbf{H}(\tau)$ in each of the m intervals is expressed (approximated) by one number which follows from setting a limit of integration in this interval. An analysis of the various possible forms of matrix \mathbf{P} is presented in the next chapter.

Taking into account (7), (8) and (9), Equation (6) can be written as

$$[\mathbf{F} - t_f \mathbf{A} \mathbf{F} \mathbf{P}] \mathbf{H}(\tau) = t_f \left\{ \left[\underbrace{\mathbf{A} \mathbf{x}_0, \dots, \mathbf{A} \mathbf{x}_0, \mathbf{0}, \dots, \mathbf{0}}_k \right] + \mathbf{B} \mathbf{C} \right\} \mathbf{H}(\tau), \quad (10)$$

where number k of non-zero columns of the matrix on the right side of Equation (10) depends on approximation degree m and the form of assumed basis $\mathbf{H}(\tau)$. For the Haar basis and the Walsh basis, $k = 1$ and for other possible wavelet packet bases, k is equal to the number of basis functions from the lowest order subspace V_l which occurs in the decomposition of considered space V ($V = V_l \oplus \dots$).

If the sum in braces on the right side of Equation (10) is denoted by \mathbf{G}

$$\mathbf{G} = t_f \left[\underbrace{\mathbf{A} \mathbf{x}_0, \dots, \mathbf{A} \mathbf{x}_0, \mathbf{0}, \dots, \mathbf{0}}_k \right] + t_f \mathbf{B} \mathbf{C}, \quad (11)$$

then equation (10) can be expressed as

$$[\mathbf{f}_0, \mathbf{f}_1, \dots, \mathbf{f}_{m-1}] - t_f \mathbf{A} [\mathbf{f}_0, \mathbf{f}_1, \dots, \mathbf{f}_{m-1}] \mathbf{P} = [\mathbf{g}_0, \mathbf{g}_1, \dots, \mathbf{g}_{m-1}], \quad (12)$$

where \mathbf{f}_i and \mathbf{d}_i are $i+1$ columns of sought matrix \mathbf{F} and given matrix \mathbf{G} , respectively. Equation (12) can be easily solved using the Kronecker product as in [19], [20]

$$\begin{bmatrix} \mathbf{f}_0 \\ \mathbf{f}_1 \\ \vdots \\ \mathbf{f}_{m-1} \end{bmatrix} = [\mathbf{I} - t_f \mathbf{A} \otimes \mathbf{P}^T]^{-1} \begin{bmatrix} \mathbf{g}_0 \\ \mathbf{g}_1 \\ \vdots \\ \mathbf{g}_{m-1} \end{bmatrix}, \quad (13)$$

where \mathbf{I} is a unit matrix, and Kronecker product $\mathbf{A} \otimes \mathbf{P}^T$ is defined as

$$\mathbf{A} \otimes \mathbf{P}^T = \begin{bmatrix} P_{11} \mathbf{A} & P_{21} \mathbf{A} & \cdots & P_{m-1,1} \mathbf{A} \\ P_{12} \mathbf{A} & P_{22} \mathbf{A} & \cdots & P_{m-1,2} \mathbf{A} \\ \vdots & \vdots & \cdots & \vdots \\ P_{1m} \mathbf{A} & P_{2m} \mathbf{A} & \cdots & P_{mm} \mathbf{A} \end{bmatrix}. \quad (14)$$

The solution of Equation (13) is the starting point for a search for state \mathbf{x} of analyzed system (6).

If we assume that expansion $\mathbf{x}(\tau)$ (instead of expansion $\dot{\mathbf{x}}(\tau)$) is sought in basis $\mathbf{H}(\tau)$

$$\mathbf{x}(\tau) = \tilde{\mathbf{F}} \mathbf{H}(\tau), \quad (15)$$

then after integrating Equation (6) and incorporating (7) we get an equation analogous to (10), which has this form

$$\left[\tilde{\mathbf{F}} - t_f \mathbf{A} \tilde{\mathbf{F}} \mathbf{P} \right] \mathbf{H}(\tau) = \left\{ \left[\underbrace{\mathbf{x}_0, \dots, \mathbf{x}_0}_{k}, \mathbf{0}, \dots, \mathbf{0} \right] + t_f \mathbf{B} \mathbf{C} \mathbf{P} \right\} \mathbf{H}(\tau). \quad (16)$$

The subsequent solution procedure (for seeking $\tilde{\mathbf{F}}$) is similar to the one described above.

Let the coefficients of matrices \mathbf{A} and \mathbf{B} be functions of independent variable τ ($\mathbf{A} = \mathbf{A}(\tau)$ and $\mathbf{B} = \mathbf{B}(\tau)$). Then if the sought solution is to have form (15), the procedure of solving system of Equations (6) becomes more complex. Time-dependent matrices $t_f \mathbf{A}(\tau)$ and $t_f \mathbf{B}(\tau) \mathbf{u}(\tau)$ in Equation (6) are represented as series

$$\begin{aligned} t_f \mathbf{A}(\tau) &= \sum_{i=1}^p \mathbf{A}_i \alpha_i(\tau), & p \leq n^2, \\ t_f \mathbf{B}(\tau) \mathbf{u}(\tau) &= \sum_{j=1}^q \mathbf{b}_j \beta_j(\tau), & q \leq n, \end{aligned} \quad (17)$$

where \mathbf{A}_i and \mathbf{b}_j are respectively a constant $n \times n$ matrix and an n -vector, and $\alpha_i(\tau)$ and $\beta_j(\tau)$ are scalar time functions.

If we use (17), Equations (6) assume this form

$$\dot{\mathbf{x}}(\tau) = \sum_{i=1}^p \mathbf{A}_i \alpha_i(\tau) \mathbf{x}(\tau) + \sum_{j=1}^q \mathbf{b}_j \beta_j(\tau), \quad \mathbf{x}(\mathbf{0}) = \mathbf{x}_0, \quad (18)$$

where p and q denote the numbers of time-dependent elements of matrix $\mathbf{A}(\tau)$ and product $\mathbf{B}(\tau) \mathbf{u}(\tau)$, respectively.

If we expand functions $\alpha_i(\tau)$ and $\beta_j(\tau)$ in basis $\mathbf{H}(\tau)$

$$\begin{aligned} \alpha_i(\tau) &= \mathbf{d}_i^T \mathbf{H}(\tau), \\ \beta_j(\tau) &= \mathbf{e}_j^T \mathbf{H}(\tau), \end{aligned} \quad (19)$$

integrate Equation (18) and use (15) and (19), we obtain

$$\tilde{\mathbf{F}} \mathbf{H}(\tau) - \left[\underbrace{\mathbf{x}_0, \dots, \mathbf{x}_0}_{k}, \mathbf{0}, \dots, \mathbf{0} \right] \mathbf{H}(\tau) = \sum_{i=1}^p \mathbf{A}_i \tilde{\mathbf{F}} \int_0^\tau \mathbf{H}(\tau) \mathbf{H}^T(\tau) \mathbf{d}_i d\tau + \sum_{j=1}^q \mathbf{b}_j \int_0^\tau \mathbf{e}_j^T \mathbf{H}(\tau) d\tau, \quad (20)$$

where \mathbf{d}_i and \mathbf{e}_j stand for the n -vectors of the expansions, in basis $\mathbf{H}(\tau)$, of the respective functions α_i and β_j . The first term of the right side of Equation (20) includes integral $\int_0^\tau \mathbf{H}(\tau)\mathbf{H}^T(\tau)\mathbf{d}_i d\tau$ which, after the expansion of the integrand in basis $\mathbf{H}(\tau)$

$$\mathbf{H}(\tau)\mathbf{H}^T(\tau)\mathbf{d}_i = \mathbf{D}_i\mathbf{H}(\tau), \quad (21)$$

can be written as $\mathbf{D}_i \int_0^\tau \mathbf{H}(\tau) d\tau$. Taking into account the above and substituting

$$\tilde{\mathbf{G}} = \left[\underbrace{\mathbf{x}_0, \dots, \mathbf{x}_0}_k, \mathbf{0}, \dots, \mathbf{0} \right] + \sum_{j=1}^q \mathbf{b}_j \mathbf{e}_j^T \mathbf{P}. \quad (22)$$

Equation (20) can be written as

$$\tilde{\mathbf{F}} = \sum_{i=1}^p \mathbf{A}_i \tilde{\mathbf{F}} \mathbf{D}_i \mathbf{P} + \tilde{\mathbf{G}}. \quad (23)$$

This is referred to as the generalized form of the Lyapunov equation whose solutions $\tilde{\mathbf{F}}$ can be obtained using the Kronecker product

$$\begin{bmatrix} \tilde{\mathbf{f}}_0 \\ \tilde{\mathbf{f}}_1 \\ \vdots \\ \tilde{\mathbf{f}}_{m-1} \end{bmatrix} = \left[\mathbf{I} - \sum_{i=1}^p \mathbf{A}_i \otimes (\mathbf{D}_i \mathbf{P})^T \right]^{-1} \begin{bmatrix} \tilde{\mathbf{g}}_0 \\ \tilde{\mathbf{g}}_1 \\ \vdots \\ \tilde{\mathbf{g}}_{m-1} \end{bmatrix}, \quad (24)$$

where $\tilde{\mathbf{f}}_i$ and $\tilde{\mathbf{g}}_i$ denote the $i+1$ columns of the respective matrices $\tilde{\mathbf{F}}$ and $\tilde{\mathbf{G}}$.

The algorithms introduce division of observation time t_f into m equal intervals in which the solution is piecewise constant. Obviously an analysis of long observation times requires that number m be increased, which necessitates the inversion of large $m.n \times m.n$ matrices. This inconvenience can be eliminated by dividing the observation time into z equal intervals and seeking a solution to the above equations in each of the intervals. The final solutions from the preceding step constitute the initial conditions for the next step. Proceeding in this way, we get a solution at $z.m$ points of analyzed time t_f , which even at a low approximation degree m but sufficiently large z is generally satisfactory.

4. Forms of operational matrix

Constant matrix \mathbf{P} , which enables the approximate representation of the integral of basis functions in the basis of the functions

$$\int_0^\tau \mathbf{H}(\tau) d\tau \cong \mathbf{P} \mathbf{H}(\tau), \quad (25)$$

is called (as already mentioned) an operational matrix and it is an essential component of the solution algorithms presented in chapter 3.

It has been shown [4], [5] that operational matrix \mathbf{P} assumes the following form:

- for the Haar basis

$$\mathbf{P}_m = \frac{1}{2m} \begin{bmatrix} 2m\mathbf{P}_{m/2} & -\mathbf{H}_{m/2} \\ \mathbf{H}_{m/2}^{-1} & \mathbf{0} \end{bmatrix}, \quad \mathbf{P}_1 = \begin{bmatrix} 1 \\ 2 \end{bmatrix}, \quad (26)$$

- for the Walsh basis

$$\mathbf{P}_m = \frac{1}{2m} \begin{bmatrix} 2m\mathbf{P}_{m/2} & -\mathbf{I} \\ \mathbf{I} & \mathbf{0} \end{bmatrix}, \quad \mathbf{P}_1 = \begin{bmatrix} 1 \\ 2 \end{bmatrix}. \quad (27)$$

Operational matrices (26) and (27) were determined assuming the midpoint as a representative point (limit of integration) for each of time division intervals m . We shall refer to matrices of this type as standard operational matrices. The notation of operational matrix \mathbf{P} , given by relation (27), is greatly simplified in comparison with the one found in [5]. Relations (26) and (27) provide a formula for determining operational matrices of order m if the operational matrices and a basis of order $m/2$ are given.

Let us assume that the position of the representative point for each of the m time division intervals τ is given by parameter $\gamma \in \langle 0, 1 \rangle$. If parameter $\gamma = 0$, the interval's representative point is located at its beginning, whereas if $\gamma = 1$, the point lies at the interval's end.

Operational matrices determined for different positions of representative points will be referred to as modified operational matrices. It can be easily demonstrated, by analogy with proof given in [13], that a modified operational matrix has the following form:

- for the Haar basis

$$\mathbf{P}_m = \frac{1}{2m} \begin{bmatrix} 2[m\mathbf{P}_{m/2} - (\gamma - 1/2)\mathbf{I}] & -\mathbf{H}_{m/2} \\ \mathbf{H}_{m/2}^{-1} & 2(\gamma - 1/2)\mathbf{I} \end{bmatrix}, \quad \mathbf{P}_1 = [\gamma], \quad (28)$$

- for the Walsh basis

$$\mathbf{P}_m = \frac{1}{2m} \begin{bmatrix} 2[m\mathbf{P}_{m/2} - (\gamma - 1/2)\mathbf{I}] & -\mathbf{I} \\ \mathbf{I} & 2(\gamma - 1/2)\mathbf{I} \end{bmatrix}, \quad \mathbf{P}_1 = [\gamma]. \quad (29)$$

At $\gamma = 1/2$ relations (28) and (29) become relations (26) and (27), respectively.

Although it is quite easy to obtain them, we do not show here modified operational matrices for other possible Walsh-wavelet packet bases since their notations are different each time, depending on the bases of the assumed series of subspaces. For any Walsh-wavelet packet basis it is easy to numerically obtain a modified operational matrix, using relation (25) from which it follows that

$$\mathbf{P}_m = \left(\int_0^\tau \mathbf{H}_m(\tau) d\tau \right) \mathbf{H}_m^{-1}. \quad (30)$$

The influence of different possible operational matrices on calculation accuracy for different Walsh-wavelet packets is analyzed below.

5. Numerical examples

We shall test here the influence of assumed basis $\mathbf{H}(\tau)$ and the forms of the assumed operational matrices on the solutions obtained for linear systems of differential equations with constant and variable coefficients. Let an exemplary system of equations with order $n = 4$ for the initial-value problem be given by relation

$$\dot{\mathbf{x}}(t) = \begin{bmatrix} 0 & 18 & 0 & 0 \\ 0 & 0 & 25 & 250 \\ 0 & 0 & 0 & 250 \\ -168 & -92.25 & 0 & -250 \end{bmatrix} \mathbf{x}(t) + \begin{bmatrix} 168 \sin(15t) \\ 0 \\ 0 \\ 168 \sin(15t) \end{bmatrix}, \quad \mathbf{x}(0) = \begin{bmatrix} 1.9 \\ 2 \\ 0 \\ 0 \end{bmatrix}. \quad (31)$$

The solution to system of equations (31) will be sought in time $0 \leq t \leq 0.5$ sec. for the solution form given by relation (8) and for the standard form of operational matrix \mathbf{P} for the Haar basis. It is assumed that analysis time division number $z = 1$, which means that the assumed basis \mathbf{H} is a global basis for this analysis time.

The variation of the third (x_3) component of state vector \mathbf{x} for different approximation degrees m is shown in Figure 4 by a solid line. The solution obtained using the Haar basis and relation (13) is represented by a solid piecewise constant line in each of the m intervals of analyzed time t . The solutions obtained by the 4th-order Runge–Kutta method, assuming that the analyzed time is divided into m equal intervals, are represented by a dotted line. The solutions for $m = 3$, $m = 4$, $m = 5$ and $m = 6$ are shown in Figures 4a–4d, respectively.

For other bases than basis \mathbf{H} (the Walsh basis or any other Walsh-wavelet packet basis) the obtained solutions are identical with the previous ones, which means that Walsh-wavelet packet bases are equivalent in sought solution approximation.

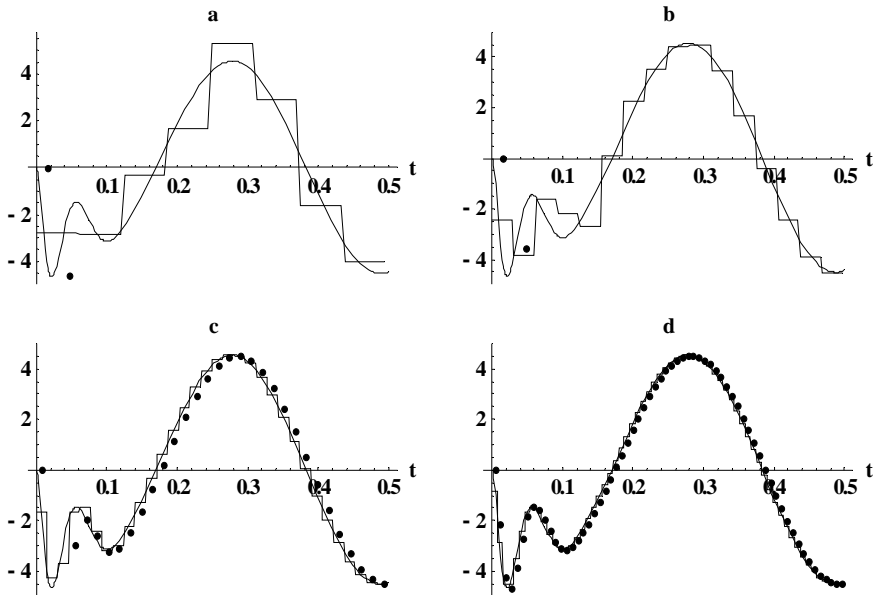


Fig. 4. Exact solution (solid line), Haar solution (piecewise constant line) and solution by Runge–Kutta method (dotted line) for the third component of vector \mathbf{x} of system (31) at different approximation degrees $m = 3$ (a), $m = 4$ (b), $m = 5$ (c) and $m = 6$ (d)

In special cases of systems of stiff equations, generally negligible differences between the results obtained using different wavelet-packet bases may occur. The differences are due to the different ranges of some or all basis functions $\mathbf{H}(\tau)$. In the Haar basis, one (constant) basis function covers the whole analyzed area, whereas the ranges of the other functions are narrower. In the Welsh basis, all the basis functions spread over the whole analyzed area. For other Walsh-wavelet bases, the basis functions' non-zero values areas are smaller than the analyzed area and in some cases, the functions may be local.

For low numbers m of division of the analyzed time, the Runge–Kutta method of the 4th kind is divergent, but at higher m the obtained solution may be satisfactory. Numerical tests do not confirm the conclusions, drawn in [18], that algorithms based on the Haar operational matrix are much more efficient than the Runge–Kutta algorithm of the 4th kind. The analysis time is comparable for the two algorithms, at least in the case of the linear problems considered here.

If relation (15) is assumed as the base of the analytical algorithm, the obtained solutions are identical to the ones yielded by the algorithm based on relation (8). If relation (15) is used, the analysis time is on the average about 10% shorter than the operating time of the algorithm based on (8). This is due to the different numbers of op-

erations necessary to determine state \mathbf{x} variables, which becomes apparent when compares relations (9) and (15).

The solutions presented below are based on algorithms using relation (15). Obviously, longer analysis times require a higher approximation degree m and consequently, among others, the inversion of a large matrix, which at high m may lead to a considerable increase in the analysis time. As already mentioned, a simple way out in such cases is to divide the analysis time into z equal intervals and assume a lower degree of approximation in each of them. It turns out that when the analysis time is divided into z intervals and the same degree of approximation is assumed in each interval, all the possible wavelet-packet bases yield equally accurate solutions in the same time. For a fixed number of divisions z , the analysis time depends on approximation degree m . The relationship between time T of analysis of system (31) and accuracy degree m for $z = 1000$ and $t_f = 3$ sec is shown in Figure 5.

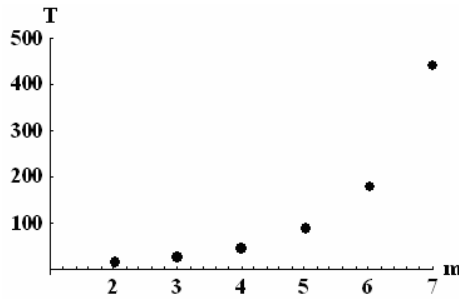


Fig. 5. System (31) analysis time versus accuracy degree m at $z = 1000$ and $t_f = 3$ sec

The above results were obtained using standard operational matrices in the algorithms. If modified operational matrices are used in the algorithms, the analysis time will change and a significant difference in computational error Δ_i^P will become apparent. The latter is measured here in percentage power of the difference between exact solution (x_i^e) and approximate solution (x_i^a), related to the power of the exact solution

$$\Delta_i^P = \left(\frac{\sum_{j=1}^{zm} |x_{i,j}^e - x_{i,j}^a|^2}{\sum_{j=1}^{zm} |x_{i,j}^e|^2} \right) \cdot 100\% \quad (32)$$

for parameter γ . $x_{i,j}^e$ and $x_{i,j}^a$ denote values of the i -th coordinate of state \mathbf{x} in the j -th central point of the analyzed interval for the exact solution and the approximate solution, respectively. Errors in computing component x_3 of equations system (31) at $m=3$ and $t_f=3$ sec for different parameters γ , specifying the form of the operational matrix, and different observation time division numbers z are given in Table 1.

Table 1. Errors in computing component x_3 of system (31) at $m = 3$ and $t_f = 3$ sec for different parameters γ and different observation time division numbers z

z	Δ_3^γ [%]				
	$\gamma = 0.00$	$\gamma = 0.25$	$\gamma = 0.50$	$\gamma = 0.75$	$\gamma = 1.00$
4	$6.3 \cdot 10^8$	23.5	1.25	1.38	2.81
6	104.2	6.17	0.721	0.879	1.89
10	11.0	2.21	0.452	0.433	0.975
20	3.14	1.25	0.424	0.199	0.339
100	2.10	1.10	0.455	0.111	0.0188
200	2.09	1.10	0.463	0.110	0.00493
600	2.09	1.11	0.468	0.110	0.000566
1000	2.09	1.11	0.469	0.111	0.000205
1200	2.09	1.11	0.470	0.111	0.000142
2000	2.09	1.11	0.470	0.111	0.0000515

According to Table 1, the error defined by relation (32) decreases as number z increases and at a sufficiently high z it generally stabilizes, its value being a function of parameter γ . At $0 \leq \gamma < 0.5$ and a sufficiently high division number z , the solution error is asymptotically convergent towards values higher than the error generated in solutions based on the standard operational matrix. At $0.5 < \gamma \leq 1$ and a sufficiently high division number z , the solution error is considerably smaller than the error at $\gamma = 0.5$ and at $\gamma = 1$ it reaches the minimum value for all possible γ .

Table 2. Errors in computing component x_3 of system (31) at $z = 20$ and $t_f = 3$ sec for different parameters γ and different approximation degrees m

m	Δ_3^γ [%]				
	$\gamma = 0.00$	$\gamma = 0.25$	$\gamma = 0.50$	$\gamma = 0.75$	$\gamma = 1.00$
0	100.0	268.0	54.6	10.5	4.11
1	1073.2	43.5	10.0	2.88	2.30
2	22.2	6.46	1.94	0.765	0.975
3	3.14	1.25	0.424	0.199	0.339
4	0.631	0.278	0.0994	0.0512	0.103
5	0.143	0.0658	0.0240	0.0130	0.0288
6	0.0341	0.0160	0.00592	0.00329	0.00762
7	0.00834	0.00395	0.00146	0.000827	0.00196

Computational errors for component x_3 of system (31) at $z = 20$ and $t_f = 3$ sec and at different parameters γ and approximation degrees m are shown in Table 2. Values of

numbers in columns of this table testify to convergence of applied approach for any γ . It must be stressed that proposed here one-step integration method for initial-value problem gives results in m equidistance time points, which respond to m steps of traditional methods with fixed t_f/m integration step.

The computation time increases with m , while the computational error decreases. It turns out that at low values of m the error is the smallest at $\gamma = 1$ and as m increases, the error minimum shifts towards lower values of γ . For $m = 7$ and $z = 20$ the smallest error is obtained at $\gamma = 0.71$. The shift of the error minimum towards lower values of γ decreases as number z increases, e.g., for $z = 100$ ($m = 7$) the error minimum is reached at $\gamma = 0.98$.

Let an exemplary $n = 4$ system of differential equations with variable coefficients be given by this relation

$$\dot{\mathbf{x}}(t) = \begin{bmatrix} 0 & 18\cos(0.5t) & 0 & 0 \\ 0 & 0 & 25 & 250 \\ 0 & 0 & 0 & 250 \\ -168 & -92.25\cos(0.5t) & 0 & -250 \end{bmatrix} \mathbf{x}(t) + \begin{bmatrix} 168\sin(15t) \\ 0 \\ 0 \\ 168\sin(15t) \end{bmatrix}, \quad \mathbf{x}(0) = \begin{bmatrix} 1.9 \\ 2 \\ 0 \\ 0 \end{bmatrix}. \quad (33)$$

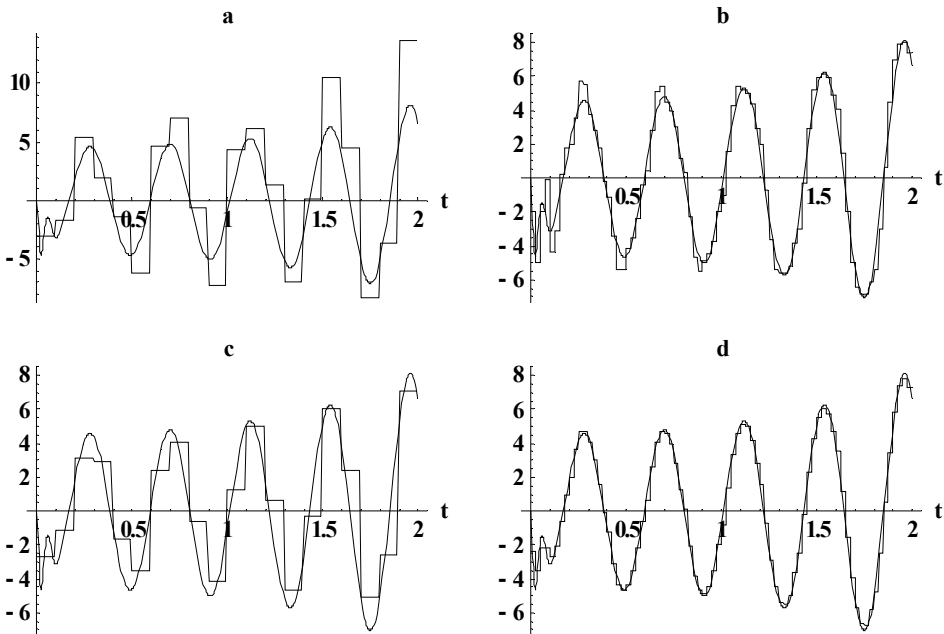


Fig. 6. Exact solution (solid line) and Walsh solution (piecewise constant line) for the second component of vector \mathbf{x} of system (33) at: $z = 5$, $m = 2$ and $\gamma = 0.4$ (a); $z = 5$, $m = 2$ and $\gamma = 0.6$ (c); $z = 10$, $m = 3$ and $\gamma = 0.4$ (b); and $z = 10$, $m = 3$ and $\gamma = 0.6$ (d)

Solutions to the second component of state vector \mathbf{x} of system (33) for $0 \leq t \leq 2$ sec are shown in Figure 6. Piecewise constant solutions which follow from relation (24) at: $z = 5$, $m = 2$ and $\gamma = 0.4$ (Figure 6a); $z = 5$, $m = 2$ and $\gamma = 0.6$ (Figure 6c); $z = 10$, $m = 3$ and $\gamma = 0.4$ (Figure 6b); and $z = 10$, $m = 3$ and $\gamma = 0.6$ (Figure 6d) are shown against the exact solution represented by a solid line.

All the observations made in the discussion of the results obtained from the analysis of system (31) have been fully corroborated by the results of the analysis of system (33) with variable coefficients.

6. Concluding remarks

The possibility of using wavelet-packet bases in algorithms for solving initial-value problems described by systems of linear differential equations with constant or variable coefficients has been demonstrated. Algorithms which use expansions of the derivative of state variables and expansions of the state variables in any wavelet-packet basis have been described and compared. The results of the analyses have been compared with the results yielded by classical methods of solving initial-value problems in their differential formulation and with exact results. The convergence, computational accuracy and efficiency (measured in computation time) of the algorithms have been tested. Special attention is devoted to different possible forms of operational matrices, which generalize the latter's conventional formulations and significantly affect computational accuracy. The so-called modified operational matrices have been formulated and their influence on computational accuracy has been tested for different bases and degrees of approximation of the solution space. Numerical tests have been run for exemplary systems of differential equations with constant and variable coefficients and several specific conclusions have been drawn on this basis.

The following general conclusions regarding the possibility of using wavelet-packet bases in the numerical analysis of linear initial-value problems emerge from this research:

- all the possible wavelet-packet bases of a given approximation order are equivalent in description of the state variables of differential initial-value problems and they generally lead to identical results in the same time;
- the form of the operational matrix assumed for the calculations has a significant effect on computational accuracy; when modified operational matrices are used at coefficient $0.5 < \gamma \leq 1$, generally more accurate solutions than the ones yielded by analyses based on conventional operational matrices are obtained in comparable computation time;
- for a given computational accuracy, algorithms employing dense analysis time division at a lower approximation degree are generally more efficient than algorithms using limited analysis time division at higher approximation degrees.

References

- [1] Finlayson B.A.: *The Method of Weighted Residuals and Variational Principles*, Academic Press, New York, 1972.
- [2] Villadsen J., Michelson M.L.: *Solutions of Differential Equation Models by Polynomial Approximation*, Prentice Hall, New Jersey, 1978.
- [3] Corrington M.S.: *Solution of differential and integral equations with Walsh functions*, IEEE Transactions on Circuit Theory CT-20, 1973, 470–476.
- [4] Chen C.F., Hsiao C.H.: *A state-space approach to Walsh series solutions of linear systems*, Int. J. System Sci., 1975, Vol. 6, 833–858.
- [5] Chen C.F., Tsay V.T., Wu T.T.: *Walsh operational matrices for fractional calculus and their application to distributed systems*, Journal of The Franklin Institute, 1977, Vol. 303, 267–284.
- [6] Hwang C., Shih Y.P.: *Laguerre operational matrices for fractional calculus and applications*, Int. J. Control, 1981, Vol. 34, 557–584.
- [7] King R.E., Paraskevopoulos P.N.: *Parameter identification of discrete time SISO systems*, Int. J. Control, 1979, Vol. 30, 1023–1029.
- [8] Chang R.Y., Wang M.L.: *Legendre polynomials approximation to dynamic linear state equations with initial or boundary value conditions*, Int. J. Control, 1984, Vol. 40, 215–232.
- [9] Paraskevopoulos P.N.: *Chebyshev series approach to system identification, analysis and optimal control*, Journal of The Franklin Institute, 1983, Vol. 316, 135–157.
- [10] Paraskevopoulos P.N., Sparcis P.D., Monroursos S.G.: *The Fourier series operational matrix of integration*, Int. J. System Sci., 1985, Vol. 16, 171–176.
- [11] Mallat S.: *A Wavelet Tour of Signal Processing*, Academic Press, San Diego, 1998.
- [12] Resnikoff H.L., Wells Jr R.O.: *Wavelet Analysis. The Scalable Structure of Information*, Springer-Verlag, New York, 1998.
- [13] Chen C.F., Hsiao C.H.: *Haar wavelet method for solving lumped and distributed-parameter systems*, IEE Proc. Control Theory Appl., 1997, Vol. 144, 87–93.
- [14] Hsiao C.H.: *State analysis of linear time delayed systems via Haar wavelets*, Mathematics and Computers in Simulation, 1997, Vol. 44, 457–470.
- [15] Hsiao C.H., Wang W.J.: *State analysis and optimal control of linear time-varying systems via Haar wavelets*, Optim. Control Appl Meth., 1998, Vol. 19, 423–433.
- [16] Chen C.F., Hsiao C.H.: *Wavelet approach to optimizing dynamic systems*, IEE Proc. Control Theory Appl., 1999, Vol. 146, 213–219.
- [17] Hsiao C.H., Wang W.J.: *State analysis and parameter estimation of bilinear systems via Haar wavelets*, IEEE Transactions on Circuits and Systems I: Fundamental Theory and Applications, 2000, Vol. 47, 246–250.
- [18] Hsiao C.H., Wang W.J.: *Haar wavelet approach to nonlinear stiff systems*, Mathematics and Computers in Simulation, 2001, Vol. 57, 347–353.
- [19] Brewer J.W.: *Kronecker products and matrix calculus in system theory*, IEEE Transactions on Circuits and Systems, 1978, Vol. CAS-25, 772–781.
- [20] Regalia P.A., Mitra S.K.: *Kronecker products, unitary matrices and signal processing applications*, SIAM Review, 1989, Vol. 31, 586–613.

Falkowe pakiety Walsh'a w analizie układów liniowych o zmiennych w czasie współczynnikach

Pokazano możliwość wykorzystania falkowych baz pakietowych w algorytmach rozwiązywania zagadnień początkowych mechaniki opisywanych układami liniowych równań różniczkowych ze stałymi bądź zmiennymi współczynnikami. Przedstawiono i porównano algorytmy wykorzystujące rozwinięcia pochodnej zmiennych stanu i rozwinięcia zmiennej stanu w dowolnej bazie pakietowej. Wyniki analiz porównano z wynikami otrzymywanymi z wykorzystaniem klasycznych metod rozwiązywania zagadnień początkowych i z wynikami dokładnymi. Testowano zarówno zbieżność i dokładność obliczeń, jak i efektywność algorytmów mierzoną czasem trwania analiz. Szczególną uwagę zwrócono na różne możliwe postaci macierzy operacyjnych, które uogólniają ich tradycyjne sformułowania i które mają istotny wpływ na dokładność obliczeń. Sformułowano tak zwane modyfikowane macierze operacyjne, których wpływ na otrzymywane wyniki testowano przy różnych bazach i różnych stopniach aproksymacji przestrzeni rozwiązań. Falkowe pakiety Walsh'a stanowią dobre bazy w metodach numerycznego całkowania zagadnień początkowych mechaniki ze stałymi bądź zmiennymi współczynnikami.

Probability of cracking of composite prestressed concrete bridges

CZESŁAW MACHELSKI

Wrocław University of Technology, Wybrzeże Wyspiańskiego 27, 50-370 Wrocław

The analysis of safety of composite prestressed concrete bridges in terms of cracking is presented. The analysis of the standard-based requirements was carried out. The assessment of safety is based on Cornell's reliability index taking into consideration two random factors: the tensile strength of concrete and the values of normal stresses at the bottom edge of girder. As random variables which affect normal stresses we adopt the effect of prestressing, dead load and live load. We also assume that the random variables are of normal distribution. The road multi-beam bridges are considered at the service stage, i.e. subjected to dead and to live loads and to the influence of prestressing under conditions of advanced rheologic processes. The paper does not deal with technological defects, thereby the problem of cracks before the prestressing of beam is neglected. The parametric analysis has shown that the standard-based cracking coefficient applied in the bridge design is neither effective nor efficient.

Keywords: *cracking, probability analysis, prestressed concrete bridge*

1. Introduction

In order to satisfy the requirements of transportation, the structure of a bridge is designed in such a way as to take account of the strength limit state and examination of the service limit state.

In the case of main prestressed concrete girders, the possibility of cracking is additionally examined. This condition is connected with the above-mentioned safety requirements concerning the strength and service limit state because the cracking of structure precedes the loss of capacity due to the break of steel and the crush of concrete. The cracking reduces the stiffness of structural member and in consequence can lead to the increase of permanent deformation (due to dead loads) and temporary deformation (due to live loads). The latter can cause the exceeding of allowable service conditions in the form of growth of deflection and undesirable changes of natural frequency. These situations are not usually taken into consideration in assumptions of design.

The measure of the code safety related to cracking [1]–[3] is the coefficient s_1 being determined on the basis of the cracking moment strength M_r and the bending moment M_k due to the permanent and transient loads:

$$s_1 = \frac{M_r}{M_k} \quad (1)$$

Condition (1) encompasses all kind of structures erected with using various techniques and methods of construction of prestressed bridge (for instance, the incremental launching, the balanced cantilever construction [3], span by span precast construction [4]), usually differing from each other on the level of prestressing. For the structural members made of homogeneous concrete (not composite section), the relationship between s_1 from (1) and standard-based level of prestressing [1] (for an appropriate class of concrete) has been found in [2]. Therefore the safety factor on cracking does not fulfill its function for homogeneous elements.

In the case of composite concrete bridges, the parameters for determining s_1 are complex owing to use of two different concretes in the cross-section of girder and owing to rheologic phenomena which occur simultaneously with dead loads [5]. Taking advantage of the probability-based approach we assessed the code of specifications-based safety on cracking [1], depending on the level of prestressing of composite bridges, expressed as the probability of cracking. The beam model is based on the Bernoulie's assumption and a full prestressing assumption (the conformity of unit deformation [5]) used usually for the contact surface of concretes at the composite zone.

2. The design conditions of the safety for the sake of cracking

◆ **Homogenous concrete girder.** Of great importance in the evaluation of safety for the sake of crack control is the level of prestressing of the beam $\sigma(S)$ [2], expressed as

$$M_r = W[(\sigma(S) + 2R_{bt0.50})]. \quad (2)$$

A normal stress at the bottom edge of the cross-section of girder due to prestressing is its measure

$$\sigma(S) = S \left(\frac{1}{A_b} + \frac{e \cdot v_d}{J_b} \right), \quad (3)$$

where:

A_b, J_b, v_d, e – the geometric parameters of the cross-section of the beam (Figure 1),
 S – the prestressing force,

$W = W_d = \frac{J_b}{v_d}$ – the section module of beam for the bottom edge of cross-section.

Within the value of cracking moment strength M_r from (2) there are included the reserves of safety resided in the possibility of plasticization of concrete at the tension zone, resulting from its physical properties and the shape of cross-section. For that reason the tensile strength of concrete [1] $R_{bt0.50}$ (the mean value of the tensile strength, that is 50% confidence that the cracks in the prestressed concrete structure will not occur) is corrected by a coefficient equal to 2.

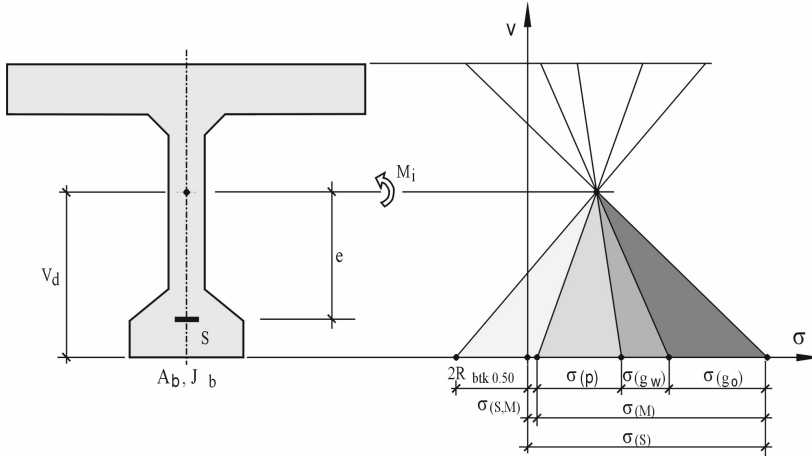


Fig. 1. Normal stresses in cross-section of homogeneous girder

Physical properties of concrete $R_{btk 0.50}$ can be expressed according to [1], [2], [3] in the form depending on the class of concrete or the guaranteed compressive strength (for example, for the concrete of class B50 $R_b^G = 50$ MPa):

$$R_{btk 0.50} = \frac{18 + R_b^G}{20}. \quad (4)$$

The bending moment due to external loading M_k from (1) consists of the effects of the dead load (g_0), the wearing surfaces and utilities load (g_w) and the live load (p)

$$M_k = M(g_0) + M(g_w) + M(p). \quad (5)$$

It can be expressed as the derivative of normal stresses (Figure 1)

$$M_k = W[(\sigma(S) - \sigma(S, M))] \quad (6)$$

when the total result of prestressing and all loads ($\sigma > 0$ stands for compression) is described by the following equation:

$$\sigma(S, M) = S \left(\frac{1}{A} + \frac{e}{W_d} \right) - \frac{M_k}{W_d} = \sigma(S) - \sigma(M). \quad (7)$$

In that case, the coefficient s_1 from (1) can be written on the basis of (2) and (6) as

$$s_1 = \frac{\sigma(S) + 2R_{btk 0.50}}{\sigma(S) - \sigma(S, M)}. \quad (8)$$

Formula (8) can be transformed in such a way as to determine the level of prestressing $\sigma(S)$

$$\sigma(S) = \frac{s_1 \cdot \sigma(S, M) + 2R_{bt0.50}}{s_1 - 1}. \quad (9)$$

Thus, the designed level of prestressing $\sigma(S)$ depends on the value of $\sigma(S, M)$, the tensile strength of concrete $R_{bt0.50}$ and the safety factor related to cracking s_1 .

According to the standard specifications [1] one can distinguish three levels of prestressing of a beam $\sigma(S)$ which gives the following values of normal stresses $\sigma(S, M)$:

- full prestressing (*SP*) when only normal stresses causing the compression are allowed to occur:

$$\sigma(S, M) \geq 0; \quad (10)$$

- partial prestressing (*SO*) when the normal stresses causing the tension do not exceed the 5% quantile of the tensile strength

$$|\sigma(S, M)| \leq R_{bt0.05}, \quad (11)$$

where $R_{bt0.05}$ depends on the class of concrete or the guaranteed compressive strength [1]

$$R_{bt0.05} = \frac{3(R_b^G + 30)}{100}; \quad (12)$$

- partial prestressing (*SC*) if

$$|\sigma(S, M)| \geq R_{bt0.05}. \quad (13)$$

Assuming $\sigma(S, M) = 0$ as the condition that differentiates between full prestressing and partial prestressing, one can obtain from (8) after having taken into account (4) the value of s_1

$$s_1 = 1 + \frac{18 + R_b^G}{10 \cdot \sigma(S)}. \quad (14)$$

As it follows from formula (14), condition (1) (for $s_1 < 1.20$) is effective if high values of $\sigma(S)$ are accompanied with relatively low class of concrete. These situations occur

very rarely [2], because high values of $\sigma(S)$ can lead to exceeding, in preliminary stage (at the moment of prestressing), the compressive strength of concrete.

◆ **The composite prestressed girder.** In the composite girder, the geometrical parameters A_p and I_p of the concrete deck slab (compare Figure 2) can be reduced to the material of beam [5], [6] using the parameter n_φ (substitute relation of elasticity modules) in the following form:

$$n_\varphi = \frac{E_b}{E_p} \cdot \frac{1 + \rho \cdot \varphi_p}{1 + \rho \cdot \varphi_b}. \quad (15)$$

In (15), we take into account the following physical properties of both components of the cross-section: E_b and E_p – the modules of elasticity of material of beam and deck slab, φ_b and φ_p – the creep coefficients for beam and deck slab. They are time-dependent parameters. The effect of their changes $\varphi(t)$ are corrected in (15) by applying the coefficient of relaxation ρ (for example, $\rho = 0.8$ [5]). Thus, the reduced moment of inertia of the slab is expressed as

$$I_{p\varphi} = I_p / n_\varphi, \quad (16)$$

and the reduced cross-sectional area of the deck slab is expressed as

$$A_{p\varphi} = A_p / n_\varphi. \quad (17)$$

The location of centroid of composite girder $a_d(t)$, as shown in Figure 2, depends on n_φ , so it varies with time. It can be calculated from the expression

$$\frac{a}{a_d} = \frac{A_b + A_{p\varphi}}{A_{p\varphi}}, \quad (18)$$

where a is the distance between the centroids of cross-sections of slab and beam (constant value). The change in location of centroids given in Figure 3 is expressed by the formula: $v_i = v_d + a_d$. At the beginning of action of permanent load g_w (for $\varphi_b = \varphi_p = 0$), the centroid of the composite cross-section is localized at the distance of v_p , as is for the temporary loads p . Under the influence of the creep of concrete of slab and beam, the distance v_p is reduced (the process runs in time) to the value of v_w . The parameter v change according to the relation $v_p > v_w$ because of the relationship $\varphi_b > \varphi_p$ which usually exists in the case of composite bridges made of an ordinary concrete.

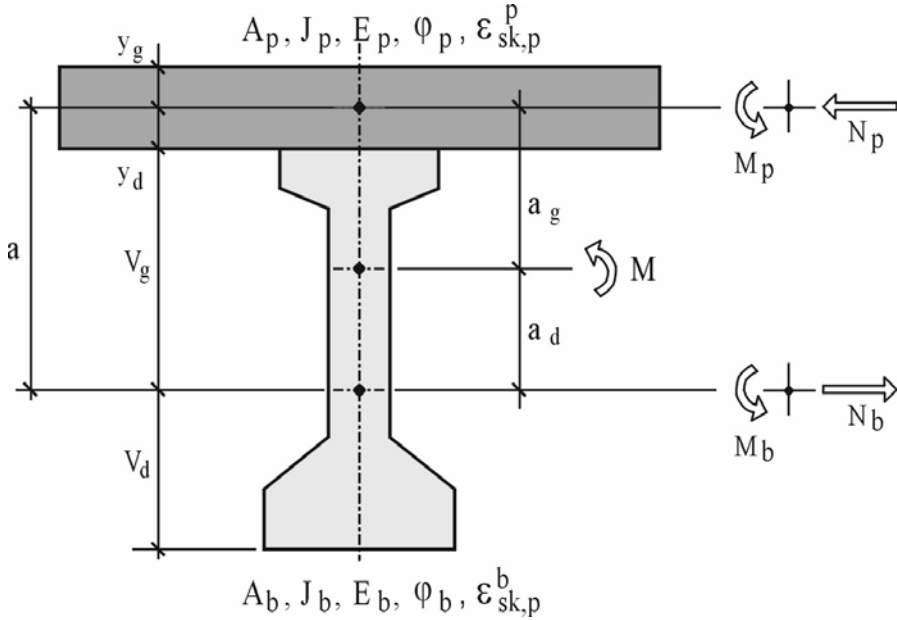


Fig. 2. Geometric, physical and static characteristics in cross-section of composite girder

Taking into consideration the equilibrium equations for static case in the cross-section of composite beam (as in Figure 2)

$$N_b - N_p = 0, \quad (19)$$

$$M = M_b + M_p + N_b \cdot a_d + N_p(a - a_d), \quad (20)$$

the conformity condition for unit deflections at the contact surface of two concrete elements (with considering the results of shrinkage and creep of concrete of beam $\varepsilon_{sk,p}^b$ and deck slab $\varepsilon_{sk,p}^p$)

$$(1 + \rho \cdot \varphi_b) \cdot \left(\frac{N_b}{E_b \cdot A_b} - \frac{v_g \cdot M_b}{E_b \cdot I_b} \right) + (1 + \rho \cdot \varphi_p) \cdot \left(\frac{N_p}{E_p \cdot A_p} - \frac{M_p \cdot y_d}{E_p \cdot I_p} \right) = \varepsilon_{sk,p}^b - \varepsilon_{sk,p}^p, \quad (21)$$

and the conformity condition for curvatures of deformed axis of components

$$\frac{M_p}{I_{p\varphi}} = \frac{M_b}{I_b}, \quad (22)$$

one can arrive at the set of equations [6]

$$\begin{bmatrix} \frac{I_b + I_{p\varphi}}{I_b} & 1 \\ -\frac{a \cdot a_d \cdot A_b}{I_b} & 1 \end{bmatrix} \cdot \begin{bmatrix} M_b \\ a \cdot N_b \end{bmatrix} = \begin{bmatrix} M \\ a_d \cdot N_{sk} \end{bmatrix}. \quad (23)$$

It can be applied to determining the internal forces in a precast beam. The results of shrinkage and creep of concrete of beam $\varepsilon_{sk,p}^b$ and deck slab $\varepsilon_{sk,p}^p$ expressed in the form of difference of unit deflections in (21) are connected with the creep of beam in the formula

$$N_{sk} = E_b \cdot A_b \frac{\varepsilon_{sk,p}^p - \varepsilon_{sk,p}^b}{1 + \rho \cdot \varphi_b}. \quad (24)$$

In the case, where the calculations concern only the external loads (and do not concern the shrinkage of concrete), the right-hand side of equation equals obviously zero. The results of action of the components of bending moment M_i from (5) include the following stages of behaviour of girder shown in Figure 3:

- non-composite action ($M = M(g_0) = M_b$ and $N_{sk} = 0$),
- composite action for the shrinkage of concrete ($M = 0$ and $N_{sk} = 0$ according to (24)),
- composite action for the dead load ($M = M(g_w)$ and $N_{sk} = 0$),
- composite action for the live load ($M = M(g_p)$ and $N_{sk} = 0$) and $\varphi_b = \varphi_p = 0$,

hence the parameter $n_\varphi = n = \frac{E_b}{E_p}$.

For a composite girder with a prestressed precast beam, one can calculate $\sigma(S)$ from Equation (3). As a result of dead load due to self-weight for non-composite action (g_0) and for composite action (g_w) and the shrinkage of concrete (ε_{sk}) and live loads (p) one can obtain the distribution of normal stresses shown in Figure 3. At the bottom fiber these stresses comprise the following components

$$\sigma(S, M) = -[\sigma(g_0) + \sigma(g_w) + \sigma(\varepsilon_{sk}) + \sigma(p)]. \quad (25)$$

In Figure 3, there are also presented the locations of centroids of composite cross-section corresponding to the stages of behaviour of structure.

For the composite girder the cracking moment strength M_r from (2) depends on the factors given in numerator of equation (26). In such a case, the safety factor related to cracking according to (1) is of the form

$$s_1 = \frac{W_z \{ \sigma(S) - [\sigma(g_0) + \sigma(g_w) + \sigma(\varepsilon_{sk})] + 2R_{bt0.50} \} + [M(g_0) + M(g_w)]}{M(g_0) + M(g_w) + M(p)}, \quad (26)$$

where W_z is the section module of cross-section girder under the temporary load $n_\varphi = n$ expressed as

$$W_z = \frac{J_x}{v_p} = \frac{J_b + A_b a_d^2 + \frac{1}{n}(J_p + A_p a_g^2)}{a_d + v_d}. \quad (27)$$

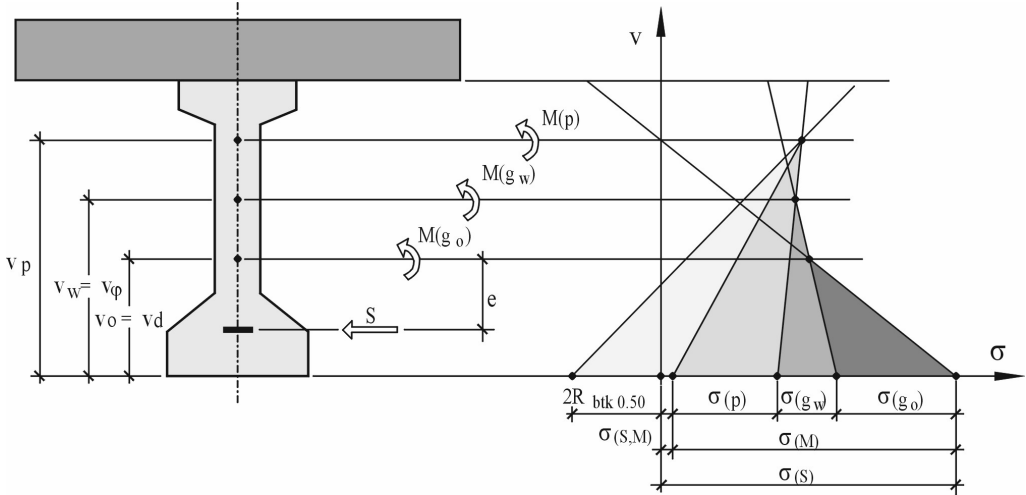


Fig. 3. Normal stresses in cross-section of composite girder

Formula (26) cannot be written in the form of (8) owing to different section modules appearing in the components of stress shown below

$$\sigma(S, M) = S \left(\frac{1}{A_b} + \frac{e \cdot v_d}{J_b} \right) - \frac{M_0}{J_b} v_d - \frac{M_w}{J_\varphi} v_\varphi - \frac{M_0}{J_x} v_p. \quad (28)$$

In the design practice, the component of stress is omitted $\sigma(\varepsilon_{sk})$, and the influence of both $\sigma(g_w)$ and $M(g_w)$ from (26) is corrected as follows:

$$s_1 = \frac{W_z \{ \sigma(S) - \sigma(g_0) + 2R_{btk 0.50} \} + M(g_0)}{M(g_0) + M(g_w) + M(p)}. \quad (29)$$

◆ **The parametric analysis.** The evaluation of the influence of simplifications established in (29) with reference to (26) is shown below. It is assumed that the geometrical characteristics of spans (length, width, the arrangement of girders, the cross-sectional dimensions of precast girders (Figure 4) and the width of roadway) and equip-

ment of those bridges are the same. Furthermore, some parameters are taken (compare Figure 2) for typical highway beam bridges. They are as follows:

- the geometry of cross-section of girder (Figure 2)
 $A_p = 0.315 \text{ m}^2$, $J_p = 0.001158 \text{ m}^4$, $y_g = y_d = 0.115 \text{ m}$,
 $A_b = 0.262 \text{ m}^2$, $J_b = 0.029276 \text{ m}^4$, $v_g = 0.5556 \text{ m}$, $v_d = 0.4444 \text{ m}$;

- the module of elasticity of concretes

$$n = \frac{E_b}{E_p} = 1.1963;$$

- the physical characteristics of concretes

$$\varphi_p = 2.18, \varphi_b = 0.80, \Delta\varepsilon_{sk} = 25 \cdot 10^{-5};$$

- the results of permanent loads

$$M_0 = 0.6588 \text{ MNm}, M_w = 0.5322 \text{ MNm}.$$

For those data the following constant parameters of analysis were calculated: $\sigma(g_o) = 10.0 \text{ MPa}$, $\sigma(g_w) = 5.0 \text{ MPa}$, $\sigma(\varepsilon_{sk}) = 1.45 \text{ MPa}$ and $W_z = 0.1144 \text{ m}^3$.

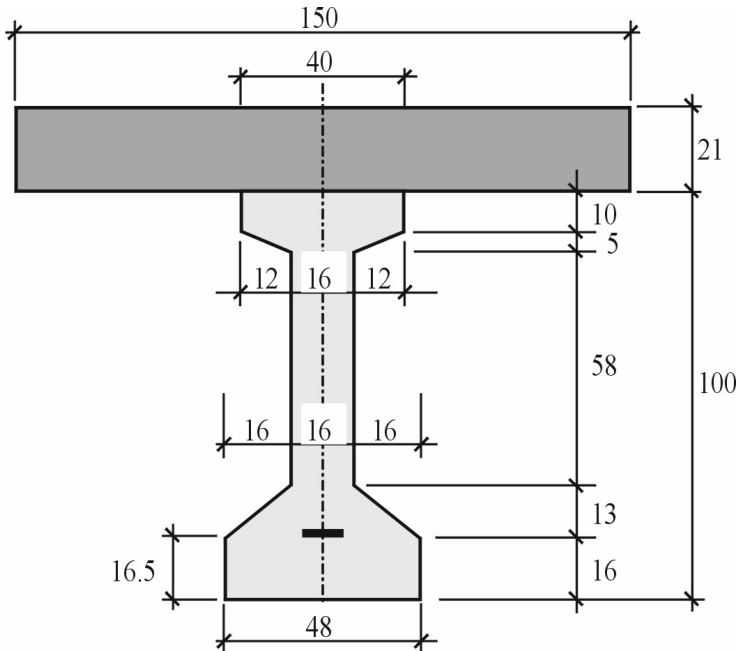


Fig. 4. Section dimensions of composite girder composed of the precast beams WBS and slab deck

As variable parameters are taken: the class of precast's concrete and the intensity of live load. In such a case, it is assumed that the effect of prestressing will be reduced by external forces $\sigma(S, M) = 0$ (Figure 3). For this reason the bending moments $M(p)$ are made dependent on the level of prestressing

$$M(p) = 0.1144 \sigma(S) - 1.716 \text{ [MPa]}. \quad (30)$$

For instance, if $\sigma(S) = 25$ MPa, then $M_p = 1.144$ MNm (if $M_p = 0$, then $\sigma(S) = 15$ MPa).

Taking account of the above, we arrive at Equation (26) written as

$$s_1 = \frac{\sigma(S) + 2R_{bt0.50} - 6.04}{\sigma(S) - 4.59}. \quad (31)$$

If $\sigma(\varepsilon_{sk})$ and the creep of concrete of the deck and beam are not taken into consideration, formula (26) can be written as follows:

$$s_1 = \frac{\sigma(S) + 2R_{bt0.50} - 4.24}{\sigma(S) - 4.59}. \quad (32)$$

The results of calculation done on the basis of formulas (26) and (29) (compare Figure 5) prove that the effect of creep and shrinkage of concrete can be significant in the evaluation of the coefficient s_1 . However, $s_1 > 1.20$ in both cases being analyzed.

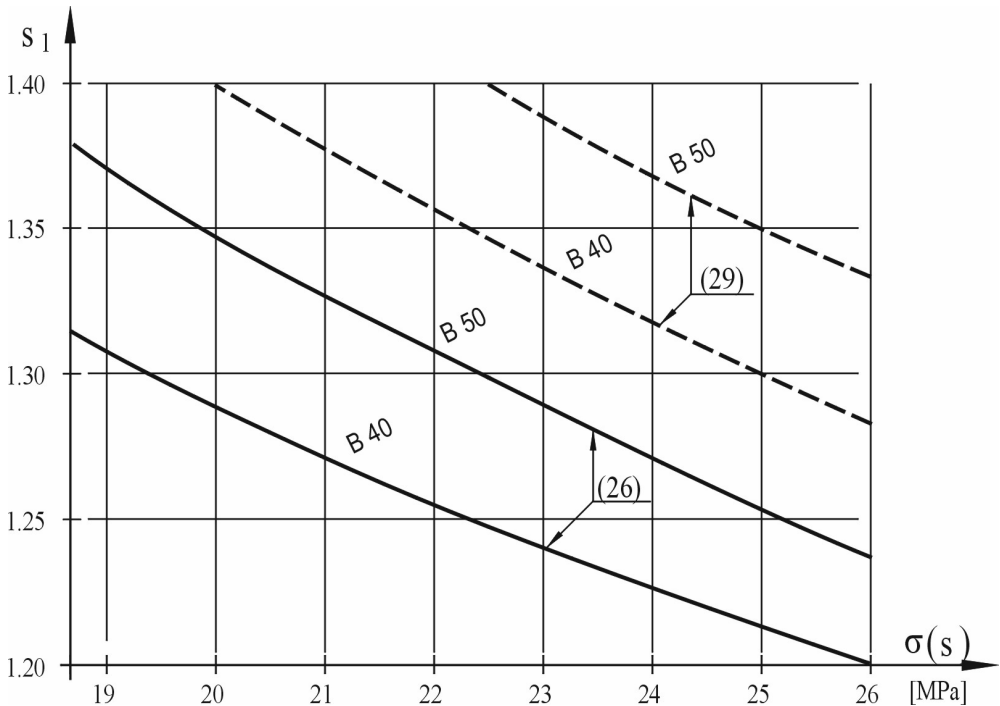


Fig. 5. Relationship between the coefficient s_1 and the level of prestressing $\sigma(S)$ for the concretes of class B40 and B50

3. The probability of cracking of precast beam

The relation between the standard coefficient s_1 given in [1] and the probability of cracking of structure of bridge is assessed using Cornell's reliability index β [3], [7]–[10]. In the case to be analyzed, the value of reliability index is expressed by two independent random variables: the tensile strength of concrete and the normal stresses at the bottom edge of flange of beam (compare Figure 6)

$$\beta = \frac{Z}{\sqrt{\sigma_r^2 + \sigma_{SM}^2}} = \frac{-m_r + m_{SM}}{\sqrt{\sigma_r^2 + \sigma_{SM}^2}} \quad \text{for } m_r < 0 \text{ (tension),} \quad (33)$$

where:

Z – the reserve of safety on cracking,

m_r – the mean value of the tension strength of concrete,

m_{SM} – the mean value of the normal stresses due to external forces and prestressing,

σ_r and σ_{SM} – the standard deviations.

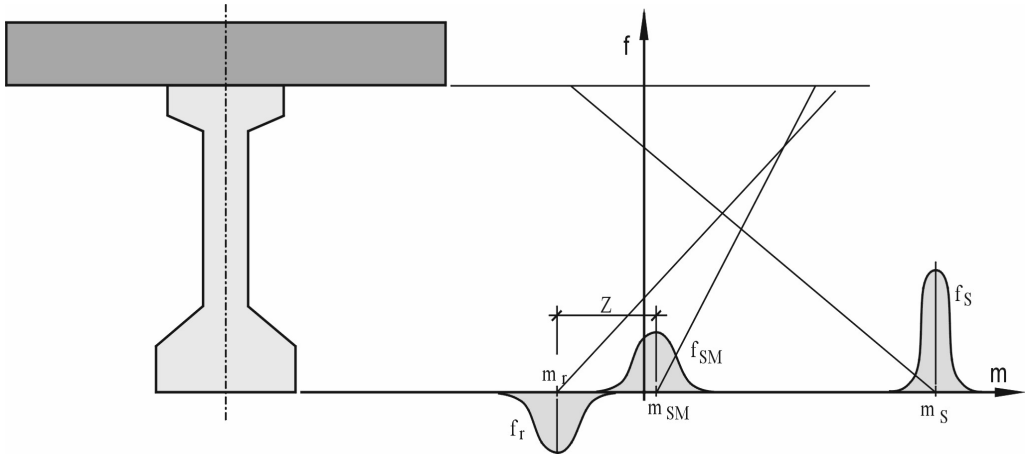


Fig. 6. The probability distribution of tensile strength and normal stresses at the bottom edge of girder

As a probabilistic model we assume [3], [4], [9] normal distributions $N[m, \sigma]$. Therefore the probability of cracking in the member, evaluated on the basis of β , is determined by

$$p_f = \Phi(-\beta), \quad (34)$$

where $\Phi(x)$ is a cumulative distribution function of normal distribution. In Figure 7, there is given the relationship $p_f(\beta)$ for the range of β being considered in the analysis of crack results.

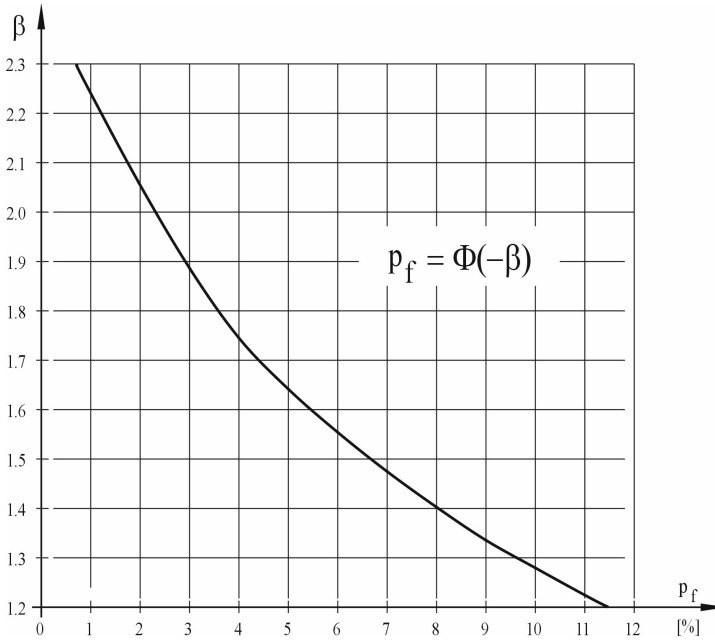


Fig. 7. Relationship between the probability of cracking p_f and the reliability index β

In the paper, the values of random parameters of concrete are based on standards [1]. If such an assumption is accepted the mean value of the tension strength of concrete ($-m_r = R_{btk\,0.50}$) depends linearly [3] on the class of concrete

$$-m_r = \frac{18 + R_b^G}{20} \text{ [MPa]}. \quad (35)$$

The standard deviation calculated from $R_{btk\,0.05}$ [1] is expressed by equation

$$\sigma_r = \frac{4R_b^G}{329} \text{ [MPa]}. \quad (36)$$

The components of the normal stresses X_i for a bottom edge of precast beam are independent random variables

$$X = X_s(S, G_0) + X_0(M_0, G_0) + X_w(M_w, G_\varphi) + X_\varepsilon(\varepsilon_{sk}, G_\varphi) + X_p(M_p, G) \quad (37)$$

which have arisen from the prestressing (S), dead load (g_0) during noncomposite action stage and from equipment load (g_w), concrete shrinkage (ε_{sk}) and live load (p) during composite action stage. The components X_i depend on random geometry of the cross-section G_i and random factors influencing normal stresses given in Figure 3 in the form of bending moments M_i or the shrinkage of concrete ε_{sk} . Within the components X_0 and X_ε both random variables M_0, G_0 and $\varepsilon_{sk}, G_\varphi$ are mutually embroiled. In

the case of X_s , X_w and X_p , we can assume that the prestressing force and bending moment are independent of the geometry of cross-section of the main girder.

In the problem analyzed, in order to obtain the distribution of probabilistic characteristic of geometry, it is convenient to use the technique of computer simulation, i.e. the Monte Carlo method [3], [4], [12]. The aforementioned method of calculation makes it also possible to analyse complex random variables, for example, in the case of shrinkage and creep of concrete [12].

Assuming that random variables X_i can be approximated by the normal distribution [3], [4], [8], [9], the mean values of stresses given in Figure 6 can be obtained from

$$m_{SM} = m_S - (m_0 + m_w + m_\varepsilon + m_p) \quad (38)$$

and the standard deviation for equation

$$\sigma_{SM}^2 = \sigma_S^2 + \sigma_0^2 + \sigma_w^2 + \sigma_\varepsilon^2 + \sigma_p^2. \quad (39)$$

The random characteristic of those variables are included in the coefficient of variations

$$v_i = \frac{m_i}{\sigma_i}. \quad (40)$$

4. The parametric analysis

To narrow down the number of variables, it is assumed that the road bridges to be analyzed have identical geometrical characteristic of spans (length, width, the arrangement of girders, the cross-sectional dimensions of precast girders and the width of roadway) and equipment. These bridges are different in the class of concrete used to precast girder and in the intensity of live load. It was assumed in that case that intensity of live load is adjusted to the level of prestressing of beam, as given in (30). It was also supposed that the effect of prestressing would be reduced by external forces and the concrete shrinkage, i.e. $m_{SM} \rightarrow 0$ (compare Figure 6). The exemplary cross-section of a girder is shown in Figure 4.

The calculations of geometric characteristics G_i are carried out on the basis of the dimensions of the cross-section as an evenly distributed variable. For the precast bridges, the changes range from -5 mm to $+10$ mm starting with a nominal value (as in Figure 4), and for the slab deck, from -10 mm to $+15$ mm. The physical properties of concretes were taken as for normal distribution:

- modules of elasticity E_b ($v = 10\%$), E_p ($v = 12.5\%$),
- volume weights $C_b = 27.0$ kN/m³ ($v = 4\%$), $C_p = 26.0$ kN/m³ ($v = 5.5\%$),
- rheologic parameters φ_b ($v = 12.5\%$) and φ_p ($v = 18\%$) and ε_{sk} ($v = 18\%$).

The effects of external loads in the form of bending moments and prestressing are treated as independent of the geometry of cross-section of girder. For that reason the coefficients of variation for geometry were determined separately with using the Monte Carlo technique; however in the case of external forces, the data found in references and literature were used. For the dead load of structure and the effects of creep and shrinkage of concretes, the calculations of stresses were carried out with the help of the computer-based simulation technique [12]. The outcomes are presented in Table 1.

Table 1. Characteristics of random variables

Components of load and effects	Load		Geometry		Stresses	
	<i>m</i>	<i>v</i> [%]	<i>m</i>	<i>v</i> [%]	<i>m</i>	<i>v</i> [%]
Prestressing	3.254	3.5 [4]	8.107	1.994	26.38	4.029
Dead load					10.00	4.257
Load of equipment	0.539	10 [9]	9.276	3.218	5.00	10.51
Shrinkage and creep					1.38	20.29
Live load	1.191	18 [9]	8.396	3.366	10.00	18.32

In Figure 8, there is shown the relationship between the probability of cracking p_f and the level of prestressing and the class of concrete obtained from (33) and (34). These results prove that the higher the level of prestressing (actually the intensity of live loads) of the same structures, the higher the probability of their cracking. As regards the class of concrete used to precast, it is clear that the beams made from high-strength concrete have much lower p_f . The results shown in Figure 8 are consistent with the calculated coefficients of reliability of cracking shown in Figure 5.

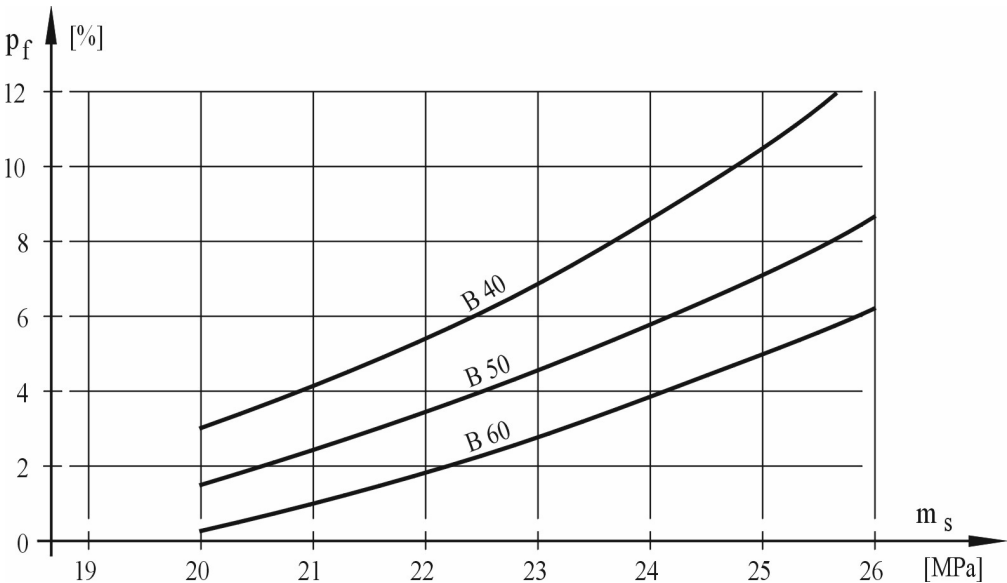


Fig. 8. Relationship between the probability of cracking p_f , class of concrete and level of prestressing

The overload of the road prestressed concrete beam bridge first of all manifests itself as the cracking. The cracking of concrete testifies to the near-structural damage, but this does not pose a threat of bridge failure. For that reason, the reliability indexes considering this effect are lower compared to the values given in Table 2. From the research of American bridges [10] it follows that the composite prestressed bridges are proved to have the highest values of β in terms of the structural damage. For other types of short- and medium-span bridges (compare Figure 9) the value of β is lower.

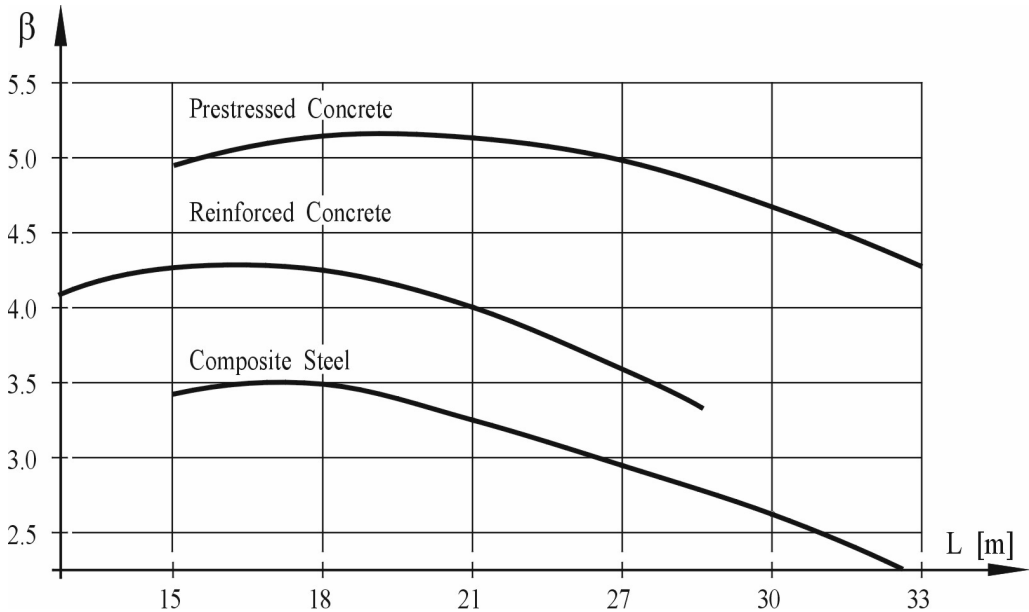


Fig. 9. Relationship between the reliability index β and the length L of typical spans of roadway beam bridges [10]

Table 2. The values of the reliability index β for building structures [13]

Safety-assurance costs	Results of damage			
	Low	Noticeable	Moderate	High
High	—	1.5	2.3	3.1
Moderate	1.3	2.3	3.1	3.8
Low	2.3	3.1	3.8	4.3

5. Conclusions

Due to the standard-based condition [1] considering a full prestressing (10), the safety factor on cracking s_1 (1) is of a limited effectiveness [2], even for the composite concrete beam-slab bridges. It is true in spite of the fact that the precast beams are usually made of high-class concrete (favorable), but with a high level of prestressing (unfavorable). A significant reduction of the value s_1 for composite concrete bridges is

obtained in the case of taking into consideration the rheological processes due to dead load (the creep of concrete) and the shrinkage of concrete, as is shown in Figure 5.

The method of design of flexural bridge members on the basis of standard assumption of the full prestressing form (10) in general case [2], [3] leads to diverse values of the probability of cracking p_f of those members. Based on the results of parametric analysis (Figure 8), the omission of condition (10) seems to be obvious for composite concrete bridges erected in continuous building cycle (if there are no contact zones over the length of span as in the technology of incremental launching).

Assumption of a uniform value of p_f (the reliability index β) as a basis for composite bridge design makes it possible to apply the standard-based [1] range of the stresses $\sigma(S, M)$, i.e. the full prestressing (FP) and the partial prestressing (PP). In the value of p_f , we take into consideration the level of prestressing of concrete $\sigma(S)$ and the class of concrete that are characteristic of the technology of bridge erection [2], [3], [4].

However, a further modification of formula for the safety factor on cracking s_1 , for example (26), in order to obtain complex p_f is ineffective. It seems to be possible only in the case of homogeneous cross-section (not for composite section) [2].

References

- [1] PN-91/S-10042. *Obiekty mostowe. Konstrukcje betonowe, żelbetowe i sprężone. Projektowanie.*
- [2] Machelski Cz.: *Ocena prawdopodobieństwa zarysowania mostów belkowych z betonu sprężonego*, Inżynieria i Budownictwo, 2003, nr 3.
- [3] Machelski Cz., Sadowski K.: *Bezpieczeństwo budowania mostów metodą betonowania wspornikowego z uwagi na możliwość zarysowania*, Drogi i Mosty, 2002, nr 3.
- [4] Machelski Cz., Onysyk J.: *Symulacja losowa wyężeń przęseł z belek prefabrykowanych*, Inżynieria i Budownictwo, 1996, nr 3.
- [5] Furtak K.: *Mosty zespolone*, Warszawa – Kraków, PWN, 1999.
- [6] Machelski Cz.: *Zmiany temperatury jako oddziaływania zastępcze skurczu i pęczania betonu w mostach zespolonych*, Inżynieria i Budownictwo, 2000, nr 12.
- [7] Murzewski J.: *Bezpieczeństwo konstrukcji budowlanych*, Arkady, Warszawa, 1970.
- [8] Śniady P., Biernat S., Sieniawska R., Żukowski S.: *Problemy i metody probabilistycznej analizy i oceny niezawodności mostów*, XLV Konferencja KILiW PAN i KN PZITB, Krynica, 1999.
- [9] Nowak A.S.: *Calibration of LRFD Bridge Code*, J. Struc. Engng. ASCE, 1995, 121, 8.
- [10] Nowak A. S.: *Probabilistic Basis for Bridge Evaluation Criteria*, US-European Workshop on Bridge Evaluation, Repair and Rehabilitation, St. Remy-les-Chevreuse, June 1987.
- [11] Machelski Cz.: *Reliability assessment of structural elements of old bridges*, Archives of Civil Engineering, 2000, XLVI, 3.
- [12] Kmita J.: *Mosty betonowe. Cz. 1. Podstawy wymiarowania*, Warszawa, WKiŁ, 1984.
- [13] ISO 2394. *General principles on reliability for structures.*

Prawdopodobieństwo zarysowania zespolonych mostów z betonu sprężonego

Przedstawiono analizę bezpieczeństwa, z uwagi na zarysowanie, zespolonych przęseł mostów wykonanych z betonu sprężonego. Dokonano analizy wymagań normowych w tym zakresie. Ocenę bezpieczeństwa oparto na wartości indeksu niezawodności Cornella, biorąc pod uwagę dwa czynniki losowe: wytrzymałość betonu na rozciąganie i wartości naprężeń normalnych na krawędzi dolnej dźwigara głównego. Jako zmienne losowe wpływające na naprężenia normalne przyjęto: efekty sprężenia i obciążeń stałych oraz zmiennych. Założono, że zmienne losowe opisuje rozkład normalny. Rozpatruje się mosty drogowe, wielobelkowe w fazie użytkowej, a więc poddane obciążeniom stałym i zmiennym oraz sprężeniu w stanie zaawansowanych procesów reologicznych. Praca nie obejmuje zagadnienia defektów technologicznych, w tym rys powstałych przed sprężeniem belek. Analiza parametryczna wykazała, że normowy współczynnik bezpieczeństwa na zarysowanie w zastosowaniu do przęseł mostów nie jest efektywny.

Information for Authors

Send to: *Archives of Civil and Mechanical Engineering*
Polish Academy of Sciences, Wrocław Branch
Podwale 75, 50-414 Wrocław, Poland

Archives of Civil and Mechanical Engineering (ACME) publishes both theoretical and experimental papers which explore or exploit new ideas and techniques in the following areas: structural engineering (structures, machines and mechanical systems), mechanics of materials (elasticity, plasticity, rheology, fatigue, fracture mechanics), materials science (metals, composites, ceramics, plastics, wood, concrete, etc., their structures and properties, methods of evaluation), manufacturing engineering (process design, simulation, diagnostics, maintenance, durability, reliability). In addition to research papers, the Editorial Board welcome: state-of-the-art reviews of specialized topics, letters to the Editor for quick publication, brief work-in-progress reports, brief accounts of completed doctoral thesis (one page is maximum), and bibliographical note on habilitation theses (maximum 250 words). All papers are subject to a referee procedure, except for letters, work-in-progress reports and doctoral and habilitation theses, which are briefly reviewed by the Editorial Board.

The papers submitted have to be unpublished works and should not be considered for publication elsewhere.

The Editorial Board would be grateful for all comments on the idea of the journal.

Submit three copies, each complete with abstract, tables, and figures.

Detailed information about the Journal on web:

<http://www.pan.wroc.pl>

www.ib.pwr.wroc.pl/wydzial/czasopismoACME.html

<http://www.wmech.pwr.wroc.pl>

Price 12 zł
(0% VAT)